Passive Cavitation Mapping for Monitoring Ultrasound Therapy

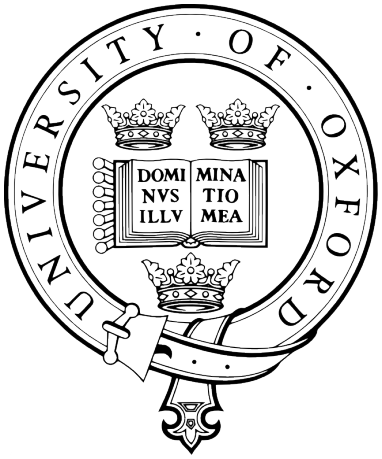

Miklós Gyöngy

Department of Engineering Science

University of Oxford

A thesis submitted for the degree of

Doctor of Philosophy

2010

Acknowledgements

In my last year as an undergraduate, a tutor had taunted me: "have you ever built a submarine"? I was more apt at example sheets than practical exercises, and he scored a sore point. The water tanks in our laboratory are too small for a submarine, but there is cavitation noise and now passive sonar to locate it, so his question no longer taunts me. When I joined the Life Sciences Interface Doctoral Training Centre in 2005, I had little idea of what research I wanted to do. Now, at the end of my doctoral studies, I have found an area of research I am passionate about. Both examples illustrate the guidance and example of my primary supervisor Constantin-C. Coussios, to whom I am deeply grateful for the skills he has taught me as a researcher and for the confidence that this has given me. I am also grateful to my other supervisor Alison J. Noble who, though not as directly involved with my research, has helped and encouraged me throughout.

Nearly everyone in Constantin's group has helped me in some way or another, but I would like to mention particularly Manish Arora and Jamie Collin. Their theoretical and experimental expertise have helped me out more times than I can count, and I am thankful for the engaging discussions I have had with them. Similarly, though only visiting Oxford for a year, it has been a pleasure to discuss with Ron Roy the subtleties of cavitation, and his experimental tips and ideas have encouraged me try out new things, giving them a chance to succeed.

The latter part of my experimental work was carried out in collaboration with Rob Ritchie, a highly able doctor and scientist, who showed a patience beyond what could be expected during our difficult and sometimes frustrating work with animal tissue. I am grateful to him, Eleonora Mylonopoulou, and the rest of the lab for their tolerance of my increasingly demanding personality towards the last months of my research.

Some of the equipment and software I used was made specifically for this research. Many thanks to Jim Fisk and Roger Lewis, the departmental technicians, who made the sample and transducer holders, as well as Bassel Rifai, who designed the two-channel phantom holder. Larry Mo (formerly of Zonare) was also invaluable in helping to explain the quirks of the ultrasound system, and in ensuring our instrumentation needs were incorporated into the ultrasound operating system. I was honoured to meet him in person at a conference.

My family, my wife's family, and friends have been a source of great moral and practical support during my studies and research. Without wishing to embarass anyone by mentioning names, many have been a model of kindness to me throughout my life and have led me to believe, perhaps foolishly but still implacably, in the truth of this University's motto.

I would like to dedicate this thesis to my wife Kinga. Many words can be used to describe her, but none more so than *fun*.

Abstract

Cavitation is a phenomenon present during many ultrasound therapies, including the thermal ablation of malignant tissue using high intensity focused ultrasound (HIFU). Inertial cavitation, in particular, has been previously shown to result in increased heat deposition and to be associated with broadband noise emissions that can be readily monitored using a passive receiver without interference from the main ultrasound signal. The present work demonstrates how an array of passive receivers can be used to generate maps of cavitation distribution during HIFU exposure, uncovering a new potential method of monitoring HIFU treatment.

Using a commercially available ultrasound system (z.one, Zonare, USA), pulse transmission can be switched off and data from 64 elements of an array can be simultaneously acquired to generate passive maps of acoustic source power. For the present work, a 38 mm aperture 5-10 MHz linear array was used, with the 64 elements chosen to span the entire aperture. Theory and simulations were used to show the spatial resolution of the system, the latter showing that the broadband nature of inertial cavitation makes passive maps robust to interference between cavitating bubbles.

Passive source mapping was first applied to wire scatterers, demonstrating the ability of the system to resolve broadband sources. With the array transversely placed to the HIFU axis, high-resolution passive maps are generated, and emissions

from several cavitating bubbles are resolved. The sensitivity of passive mapping during HIFU exposure is compared with that of an active cavitation detector following exposure.

The array was then placed within a rectangular opening in the centre of the HIFU transducer, providing a geometric setup that could be used clinically to monitor HIFU treatment. Cavitation was instigated in continuous and disjoint regions in agar tissue mimicking gel, with the expected regions of cavitation validating the passive maps obtained. Finally, passive maps were generated for samples of ox liver exposed to HIFU. The onset of inertial cavitation as detected by the passive mapping approach was found to provide a much more robust indicator of lesioning than post-exposure B-mode hyperecho, which is in current clinical use. Passive maps based on the broadband component of the received signal were able to localize the lesions both transversely and axially, however cavitation is generally indicated 5 mm prefocal to the lesions. Further work is needed to establish the source of this discrepancy.

It is believed that with use of an appropriately designed cavitation detection array, passive mapping will represent a major advance in ultrasound-guided HIFU therapy. Not only can it be utilized in real-time during HIFU exposure, without the need to turn the therapeutic ultrasound field off, but it has also been shown in the context of the present work to provide a strong indicator of successful lesioning and high signal-to-noise compared to conventional B-mode ultrasound techniques.

Contents

List of Figures

List of Tables

List of Symbols

Chapter 1

Introduction

Ultrasound is a physical phenomenon that has found a variety of clinical uses. Besides its widely recognised role in diagnostic imaging, long-standing interest in the bioeffects of ultrasound [1; 2] has spawned a number of well-established uses such as physiotherapeutic ultrasound and lithotripsy, as well as other emerging therapeutic applications. Recently, the use of high intensity focused ultrasound (HIFU) has revealed many potential applications, among them the thermal ablation of cancerous tissue [3]. However, for every ultrasond-based therapy, the need for cheap and robust monitoring strategies has also arisen, a need that still awaits fulfillment.

In this work, a new method of monitoring therapeutic ultrasound is proposed, whereby the ultrasonic emissions of cavitating bubbles excited by a therapeutic ultrasound transducer are detected passively by an array of ultrasonic receivers, and used to construct spatiotemporal maps of cavitation activity (see Figure 1.1). Such microbubble activity or *cavitation* is involved in a number of ultrasound therapies [3; 4], so the proposed method of *passive cavitation mapping* is expected to

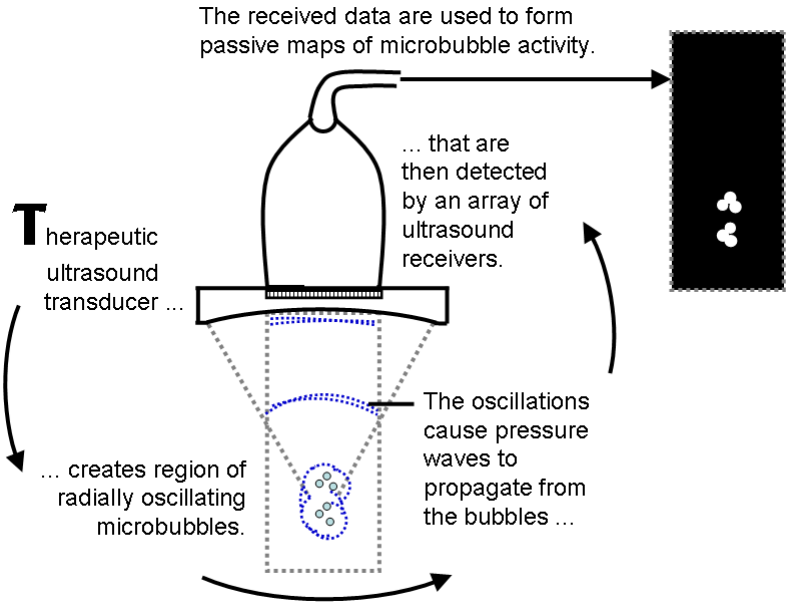

Figure 1.1: Proposed method of monitoring therapeutic ultrasound by passive cavitation mapping.

be accordingly relevant. The current work focuses on the applicability of passive cavitation mapping to monitoring thermal ablation by HIFU.

In order to appreciate the validity and usefulness of passive cavitation mapping, the first section of this chapter investigates the thermal and mechanical bioeffects of ultrasound, and shows that cavitation is often involved in both types of bioeffects. In Section 1.2, the procedure of thermally ablating tissue using HIFU is presented. Current monitoring strategies for ablative HIFU treatment are then discussed in Section 1.3, demonstrating the gap in knowledge that the passive cavitation mapping technique presented in this thesis aspires to fill. Finally, the last section presents the layout of the rest of this thesis.

1.1 Interaction of ultrasound with tissue

1.1.1 Linear propagation of pressure waves

Ultrasound propagates through a medium by oscillations of its constituent molecules, or particles. Depending on whether the oscillations are parallel or perpendicular to the direction of wave propagation, the propagating disturbances take the form of pressure and shear, respectively [5]. Tissue, by virtue of its viscoelasticity, can support both types of waves. Compared with pressure waves, shear waves are heavily absorbed in tissue at ultrasonic frequencies [6] and are therefore not widely employed in medical ultrasound. This work is concerned with the generation and detection of pressure waves.

Normally, pressure waves are modelled as propagating linearly, that is, the shape of the waveform is unchanged as it travels. This remains the case even if the waveform amplitude is decreased by absorption, scattering, or (in the case of non-planar waves) geometric spreading. For pressure disturbances that are small relative to the ambient pressure, linear propagation is a valid assumption. However, diagnostic and therapeutic ultrasound often employs pressure amplitudes well in excess of 1 MPa, where nonlinear effects become significant [7; 8; 9].

1.1.2 Non-linear propagation

Contrary to the linear assumption, a particle travelling in the same direction as the pressure disturbance will transmit the disturbance faster than if it was travelling in the opposite direction. As a consequence, the compressional phase of a waveform

will travel faster than the rarefactional phase, resulting in distortion of the waveform [7]. The degree to which a linear wave becomes distorted as it propagates through a medium depends on the coefficient of non-linearity of the medium (a material property), and increases with increasing amplitude, frequency and distance of propagation [10]. In the frequency domain, the distortion is seen as a gradual transfer of energy from the fundamental frequency of the wave to its harmonics. Since attenuation in tissue typically varies with $f^{1.1}$, where f is frequency [11], non-linear propagation enhances the attenuation of the distorted wave.

Although non-linear propagation is an important phenomenon in biomedical ultrasonics, it should be noted for later reference that attenuation of the transmitted waveform (including its conversion to harmonics) will diminish the non-linearity of propagation, and hence its effects, with distance. In addition, since dispersion (the variation of propagation speed with frequency) is negligible in tissue [12], the generated harmonics will remain in phase with the original waveform.

1.1.3 Thermal effects

As a planar ultrasound wave propagates through tissue, it attenuates due to the combined effects of scattering arising from tissue inhomogeneities and absorption. Absorption, caused by a variety of effects including viscous damping, thermal damping, and molecular relaxation [13; 14; 15], converts acoustic energy to thermal energy.

As with total attenuation, the frequency-dependence of absorption in tissue is also approximately linear [11; 16]. Therefore, non-linear propagation will cause a wave to dissipate its energy over a shorter propagation distance and increase the

local rate of heat deposition [17; 18]. As will be discussed later, inertial cavitation, which is a special form of non-linearity, also greatly enhances the local rate of heat deposition by converting part of the incident acoustic energy into broadband emissions [19; 20; 21].

The elevation of tissue temperature above its normal physiological value (37°C) causes a wide range of bioeffects. Temperatures of up to 45°C may promote tissue repair [22; 23], however, exposures above 40°C can also lead to cell death, depending on exposure duration [24]. Raising whole body temperature (up to 42°C) or malignant tissue temperature (up to 50°C) induces an immune response that complements radiotherapy, chemotherapy and immunotherapy in the treatment of cancer [24; 25]. Above 50°C, cells in tissue are rapidly destroyed, or *ablated*. Given its relevance to this work, a description of thermal ablation follows.

Thermal ablation

Living organisms rely on a plethora of long-chain molecules whose function is largely determined by their structure. In the case of proteins, structure is maintained by relatively weak hydrogen and hydrophobic bonds. Thus, external stresses on a molecular scale often cause disruption of the protein structure, known as *denaturation* [26]. Under normal circumstances, denaturation is a reversible process. However, sustained disruption, such as that caused by heat, can lead to hydrophobic regions of the protein being exposed to the surrounding aqueous solution. This can cause protein aggregation and an irreversible loss of function [27].

Although other processes are responsible for thermal ablation [27; 28], protein aggregation is generally considered to be the main mechanism, which manifests

itself as white opaque tissue in gross pathology [29; 30] and coagulative necrosis in histology [31; 32]. Protein aggregation is not well understood, however the work of Wu *et al.* [33] has shed some light on its mechanism. By assessing changes in the mechanical properties of bovine muscle during thermal ablation, they identified three regions on a hysteretic shear modulus-temperature curve, believed to correspond to three types of protein behaviour. Up to temperatures of 55°C, the tissue softened, and was observed to return to its original stiffness on cooling. This first region was thus thought to correspond to reversible protein denaturation. At 60°C, a marked and irreversible increase in tissue stiffness occured, and this increase continued up to the maximum temperature in the experiment, 75 °C. Protein aggregation, and hence cell death, is thought occur in this second region. Finally, after tissue was allowed to cool to room temperature, tissue softened again, but remained stiffer than in its original state. Subsequent heating showed the third region to have reversibility.

The above results suggest a relatively simple relationship between temperature, stiffness, and cell death, even if this relationship may become more complex above 75°C [34; 35]. In fact, the amount of time for which tissue is held at an elevated temperature greatly determines the probability of thermal ablation [36].

Thermal dose

While it is helpful to quote which temperature ranges are generally associated with different thermal effects, these values ignore the cumulative effect of exposure to elevated temperatures. Therefore, it would be useful to reduce any temperature history $\mathrm{T}(t)$ to a scalar quantity called a *thermal dose* that would allow prediction of different physiological outcomes. A simple and intuitive definition of thermal dose

is the amount of time for which the tissue should have been held at 43°C to achieve the same outcome. To formulate this definition, called the *cumulative equivalent minutes* at 43°C (CEM_{43}), it is assumed that thermal effects can be described by a single chemical reaction whose rate constant varies exponentially with temperature [37]:

$$\mathrm{CEM}_{43} = \int_{t=t_0}^{t=t_{end}} R^{43-\mathrm{T}(t)} \mathrm{d}t, \tag{1.1}$$

where tissue temperature was elevated in the time period $t \in [t_o, t_{end}]$. A common estimate of R is [37]

$$R = \begin{cases} 0.25 & \text{for } \mathrm{T}(t) < 43°\mathrm{C} \\ 0.5 & \text{for } \mathrm{T}(t) \geq 43°\mathrm{C} \end{cases} \tag{1.2}$$

The above expressions for the thermal dose are useful for temperatures below 50°C [38]. Furthermore, they provide a simple metric: above 43°C, every degree Celsius halves the required treatment time. Above 50°C, however, the applicability of CEM_{43} becomes uncertain. This is reflected by the great variation of estimates for the thermal dose required to achieve thermal ablation – as a conservative measure, an upper value of 240 minutes at 43°C is generally adopted [39; 40; 41]. One source of variation could be the amplification of thermometry errors due to the exponential term in Equation 1.1 [42]. It is also likely that a different estimate of R is required for higher temperatures [43], with an exponential temperature dependence that reflects the more general Arrhenius equation [44; 45]. Even the Arrhenius equation, however, wrongly assumes a single dominant reaction over all ablative temperatures. In contrast, the denaturation of a single protein has been shown to

consist of several steps. Furthermore, the denaturation of different proteins will become significant at different temperatures [46; 47].

1.1.4 Acoustic cavitation

Although definitions of cavitation vary depending on context, in this work cavitation will be taken to refer to the oscillations of bubbles caused by sound, also termed *acoustic cavitation* [48]. Therefore, phenomena such as *nucleation* (bubble formation) or boiling will be treated as separate from cavitation, even if they are closely related [49; 3]. With this definition in mind, the response of a bubble to an acoustic field is described, followed by the resulting thermal and mechanical effects.

Linear bubble behaviour

Despite their beguilingly simple appearance, bubbles give rise to a variety of complicated cavitation phenomena. Perhaps the simplest example of cavitation is a spherical bubble made to weakly oscillate using a spatially uniform and temporally sinusoid pressure field. This scenario can be physically approximated with a plane wave whose wavelength is much larger than the bubble radius. Assuming small excursions from its mean radius, the bubble can be modelled as a simple harmonic oscillator [50; 51]. The components of the oscillator are the inertia of the surrounding liquid, the stiffness arising from gas compressibility and surface tension at the liquid-gas interface, and various damping effects, including thermal damping, viscous damping and the re-radiation (or scattering) of the incident pressure wave [20].

Because of the linear response of the bubble to the incident pressure wave, the frequency of the scattered wave will be that of the incident wave. However, the scattering amplitude will be highest at the resonant frequency of the bubble. For an air bubble surrounded by water, with an equilibrium radius $r_0 > 5$ µm, surface tension can be neglected and the resonance frequency is approximately $3.26/r_0$ MHz (with r_0 in micrometres) [20]. In the present work, the frequency of insonation is typically 1.1 MHz, so for the bubble sizes implicated, surface tension must be taken into account. Furthermore, the contrast in acoustic properties between a bubble and the surrounding medium is so great that at megahertz insonations, even modest pressure amplitudes of 0.01 MPa invalidate the linear approximation [20]. In this work, pressure amplitudes of 1 MPa are frequently exceeded. Nevertheless, this simple formula indicates that it is micron-sized bubbles (or *microbubbles*) that have the highest response to megahertz insonations. Therefore, in future discussions, the word bubble will imply microbubble, unless stated otherwise.

Stable and inertial cavitation

As the incident pressure amplitude is increased, the behaviour of a bubble deviates from that of a simple harmonic oscillator and the scattered wave becomes increasingly non-linear. The scattered wave, and the increased levels of harmonic components it contains, can be detected using an acoustic receiver [48].

Above a certain rarefactional pressure threshold, the bubble expands to a radius several times larger than its equilibrium radius. In the subsequent contraction that follows, the acceleration of the bubble wall is dominated by the inertia of the surrounding liquid, with the rising pressure inside the bubble, the surface tension of the

Figure 1.2: Simulations of an inertially cavitating contrast agent microbubble. Left: radius-time curvature of the bubble and radiated pressure 1 cm from the bubble. The sudden rebounds of the bubble following each collapse causes sharp broadband pulses to be emitted. Right: the radius-time profile of the bubble has been scaled and is indicated by the envelope. The pressure recorded by a hydrophone is filtered by its 22.2–27.8 MHz response, showing ringing at the centre frequency (25 MHz). Figures taken from Church and Carstensen [53].

bubble wall, or even the acoustic field having a negligible effect [52]. The ensuing violent collapse, appropriately termed *inertial cavitation*, occurs much faster than the compression part of the acoustic cycle [49].

Figure 1.2 shows a typical radius-time curvature of an inertially cavitating bubble (although the figure illustrates the collapse of a contrast agent microbubble, the behaviour agrees qualitatively with that of a systemic gas bubble). Since the radiated pressure is proportional to the second temporal derivative of bubble volume [49] (which, to a first approximation, is proportional to the acceleration of the bubble wall), the abrupt changes from collapse to rebound cause the emission of shocked pulses [54; 55; 49].

Since tissue absorption increases with frequency, the re-radiation of the incident pressure wave at mostly higher frequencies than the insonating frequency leads to

enhanced heating along the path of emission [19; 20; 21]. Due to the high attenuation of higher frequency components, as well as spherical spreading of the wavefront, most heating is expected to occur within 0.1 mm of the microbubble centre [56]. Outside this region, the emission is expected to propagate in a linear manner due to the significantly reduced pressure amplitude [57]. Even without these attenuating effects, the finite bandwidth of a receiver will cause "ringing" of the received signal at the receiver centre frequency, as depicted in Figure 1.2 for the case of a 22.2–27.8 MHz hydrophone. Later experimental results obtained with the 5-10 MHz array used in this work (see Section 2.3.2) will also depict similar ringing (see, for example, Figure 5.2).

If cavitation activity repeats itself over several hundred cycles, it is termed *stable cavitation*. Although the phenomena of stable and inertial cavitation are not mutually exclusive, increased driving pressures cause the cavitating bubble to be more chaotic. A bubble that cavitates equally for every cycle of the insonating pressure wave will, according to Fourier theory, have an emission power spectrum consisting of peaks at the harmonics of the driving frequency. This remains the case even if each individual cavitation event is inertial and emits a broadband pulse. However, with increasing pressure amplitudes, the number of periods over which an emission pattern repeats itself increases, generating submultiples of the driving frequency and its harmonics [48]. These frequencies are referred to as the *subharmonics* and *ultraharmonics* of the driving frequency, respectively. Eventually, the emission trace will be fully chaotic, with a broadband spectrum that is generally associated with inertial cavitation. This chaoticity will be enhanced if the ultrasound field contains

several cavitating bubbles, as the scattering and collapse of one bubble can influence that of another [58].

The lifecycle of a bubble

Even under the same ultrasound insonation, several phenomena act to change the nature of a single bubble and therefore its response under the effect of an ultrasound field. To help appreciate the evolution of cavitation dynamics with time, the typical life cycle of a bubble in tissue is considered when a high intensity ultrasound field is switched on.

First, the bubble needs to originate from somewhere. The tensile strengh of homogeneous tissue, on the order of 10 MPa [20], is much larger than the pressures generated by diagnostic ultrasound devices, or even most therapeutic devices. Even so, cavitation has been observed at modest pressure amplitudes [59; 60]. Similarly, it is well known that bubbles may appear following the rapid ascent of a scuba diver, the decompression being significant but well below 10 MPa. These observations suggest the pre-existence of bubble nuclei in tissue, for which a variety of explanations have been offered: the crevice model [61; 62; 63; 64], the skin surface model [65], spontaneous nuclear fission [66], cosmic radiation [67], tribonucleation [68], and spontaneous homogeneous nucleation [69; 70].

Once a bubble is formed, an ultrasonic pulse of sufficient intensity can make it collapse inertially. However, for every insonation frequency, there is an optimal range of bubble sizes that can cavitate inertially [71], and the bubble may first need to grow to reach an optimal size for collapse. Any mechanism that causes growth will need to counteract surface tension and gas dissolution. One such mechanism

for bubble growth is *rectified diffusion*, where more gas and vapour enter the bubble during the rarefaction phase of the ultrasonic cycle than during the compression phase [72]. However, the pressure threshold for rectified diffusion is often very close to the inertial cavitation threshold [73], so that other effects such as absorptive heating of the surrounding medium may also be needed to help the bubble to grow [74].

Eventually, an adequate size may be reached for the bubble to collapse inertially. Following collapse, several things may happen [75]. The bubble may fragment into smaller pieces. Depending on their size, each fragment may dissolve away, start growing again, or even coalesce with other fragments. Alternatively, the bubble may not fragment at all, and simply keep cavitating inertially. With time, however, the heating of tissue caused by sonication will also play a significant part in the growth of the bubble, as decreased gas solubility causes degassing of the tissue, and a sufficient temperature rise will even cause boiling. It must be noted, however, that while acoustic cavitation may help the formation of boiling bubbles, boiling is a thermal effect that can be generated in the absence of an acoustic field [76].

Whether boiling is reached or not, the increasing size and vapour pressure inside the bubble will cause it to stabilize against inertial collapse. At this stage, the large geometric cross-section of the bubble will cause strong backscattering of the incident pressure wave, with significant harmonic components [77; 78].

Cavitation bioeffects

Typically, human tissue is densely filled with scatterers, that is, local inhomogeneities that take some of the energy from an incident plane wave by re-radiating

it in many directions. A bubble is, in effect, a very efficient non-linear scatterer of sound that re-radiates much of the incident wave at different frequencies to the driving frequency, and does so with significant motions of the bubble wall. In addition, bubbles do not scatter all the power they remove from the incident wave, with some power being absorbed at the bubble shell. All these qualities of a bubble enable cavitation to have significant thermal and mechanical effects, as described below.

Heating from a cavitating bubble can arise in many ways, but two of these are deemed to be particularly efficient [3]. Firstly, viscous heating will occur at the boundary layer between the bubble and the medium. This form of heating will be significant for larger, stably cavitating bubbles in a highly viscous medium.

In the case of inertially cavitating bubbles, another form of heating dominates: the absorption of higher frequency components generated by broadband scattering. The effect of this heating mechanism has been aptly demonstrated *in vivo*: above the inertial cavitation threshold, when an onset of broadband emissions is detected, an order of magnitude increase occurs in the local temperature rise, which allows faster thermal ablation of tissue [20; 21]. Furthermore, because inertial cavitation can only exist beyond this threshold, confining bubble activity to regions of maximum pressure within the ultrasound field can also provide a means of improved localization of ultrasound-induced bioeffects.

In addition to thermal effects, both stable and inertial cavitation will also impact their surroundings mechanically. Stable oscillations create streaming patterns around the bubble [3], a phenomenon termed *microstreaming*. Microstreaming can alter cell membrane permeability, helping to stimulate tissue repair by initiating cer-

tain biochemical cascades [22]. Microstreaming can also create stirring and micropumping, two possible mechanisms by which stable cavitation is believed to enhance the effect of the thrombolytic drug rt-PA [79]. Ultrasound-mediated blood-brain barried disruption (BBBD), a technique to deliver drugs to the brain, is also thought to occur due to stable cavitation, though the exact mechanism is as yet uncertain [41]. In all of the above cases, the injection of microbubble contrast agents provided a supply of bubbles ready to oscillate stably without the need to grow them from systemic bubble nuclei.

In contrast to the relatively mild mechanical effects of non-inertial stable cavitation, inertial cavitation is a violent phenomenon with extreme mechanical effects. In fact, rigorous study of inertial cavitation began when it was found to be chiefly responsible for the damage observed in ship propellers [80]. The damage, in the form of "pitting" on the surface of the blades, was later found to be due to high-speed liquid *microjets* [81]. These microjets arise from the asymmetric collapse of a bubble due to the nearby presence of a rigid boundary [82], contributing to destruction of calculi (organ stones) during lithotripsy [83]. In a related technique called histotripsy, soft tissue is destroyed, which creates many exciting therapeutic opportunities, including the mechanical destruction of tumours, noninvasive heart surgery, and even drug-free thrombolysis [84; 85; 86].

While close proximity to a microjet can destroy a cell, if the cell is further away, temporary poration of the cell membrane can occur [3]. Such *sonoporation* can be used for cellular drug delivery [87]. Inertial cavitation also allows transdermal drug delivery using a similar effect called *sonophoresis* [88; 89].

1.1.5 Other mechanical effects

Since ultrasound is propagated by particle oscillations, it may be conjectured that this has some mechanical bioeffect on tissue. In fact, the amplitude of oscillations is too low even at therapeutic intensities to have a direct effect [90]. However, ultrasound does not only exert an oscillatory force along the axis of propagation, but also provides a net force, over each cycle, in the direction of propagation. This phenomenon, termed *acoustic radiation force*, can take several forms [91]: a change in acoustic impedance causes a force on the boundary [92], and even a medium with uniform impedance will experience a force due to the energy density lost through attenuation [93]. Both manifestations of the acoustic radiation force can give rise to streaming in a liquid such as blood [94], with the "boundary force" relying on small particles to create flow. Such streaming is said to induce fluid shear stress along cell membranes, altering their permeability and causing upregulation of genes [95]. Alteration of metabolism in such a way can be very useful: for instance, it has been shown to be a contributor to bone repair during ultrasound physiotherapy [95].

A fitting way to conclude this discussion on ultrasound bioeffects is to highlight the potential for synergy using the example of acoustic hemostasis. In this ultrasound therapy, heating, macrostreaming, microstreaming, and the mechanical effects of inertial cavitation have all been implicated: while heating causes thermal coagulation, mechanical effects shear and rip apart platelets in the bloodstream, whose contents in blood serum activate other platelets [96; 97].

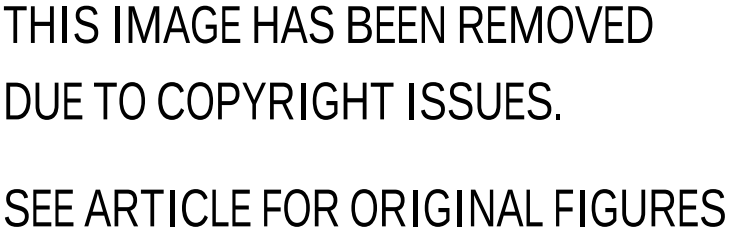

Figure 1.3: Schematic of non-invasive tumour ablation by HIFU (from [98]).

1.2 Tissue ablation by High Intensity Focussed Ultrasound (HIFU)

The previous sub-section has described the many bioeffects that can be induced by ultrasound, illustrating its tremendous potential for therapy. A particularly promising therapeutic application of ultrasound lies in the exploitation of thermal effects induced by High Intensity Focussed Ultrasound (HIFU), generally generated by an extracorporeal (outside the body) transducer to destroy malignant tissue deep within the body.

Principle of operation

Figure 1.3 depicts a typical arrangement for an extracorporeal HIFU treatment system. A spherically focussed single-element or multi-element transducer is placed over the skin (with a coupling medium in between) and used to transmit acoustic

energy into the body, creating high ultrasound intensities at the focal region.

A typical focal region at 1 MHz has a length of 15 mm along the HIFU axis and a width of 2 mm, with a shape and size comparable to a grain of rice. Ultrasound absorption raises the local temperature at the focal region by more than 30°C in a matter of seconds [98], resulting in rapid cell death (see Section 1.1.3). By moving the HIFU focus after each exposure, the whole tumour can be gradually "painted out" and thus destroyed [32].

Treatment efficacy

Focusing ultrasound is crucial for achieving selective thermal ablation of tissue: firstly, the local thermal deposition is made several orders of magnitude higher than elsewhere; secondly, provided a high (if not unity) duty cycle is used, the high acoustic intensities obtained with focusing allow for rapid destruction of tissue before heat conduction and blood perfusion [99; 100] can either limit thermal damage, or spread it elsewhere. Therefore, any effect that enhances focusing is worth considering, while any effects that limit it should be avoided. Two of each are given below.

Higher pressures increase the effect of non-linear propagation, which in turn increases local absorption due to the increased harmonic content of the pressure wave [17]. Therefore, non-linear propagation of sound enhances absorption at the focal region [18]. Inertial cavitation further enhances focusing, since only the region above the cavitation threshold will support inertial cavitation, with the heating effect of inertial cavitation being very local (within 1 mm of the bubble) [19; 20; 56; 21].

Unfortunately for HIFU treatment, the overlying tissue between the HIFU transducer and the intended focus will limit focal thermal deposition in two ways: firstly,

the pressure waves travelling towards the focus will be attenuated by scattering and absorption. More dangerously, gross tissue inhomogeneities will cause distortion of the HIFU beam, either by skin layers of differing speeds of sound [101], or bubbles [102].

Because of the marked increase in acoustic impedance compared to the surrounding tissue, the presence of bubbles is important to consider in HIFU. Bubbles can "shield" the HIFU wave from deeper regions of tissue that may need to be treated, and they can also cause reflection of the incident HIFU wave to "hot spots" of high acoustic intensity in front of the focus. The latter phenomenon gives rise to "tadpole-shaped" lesions, where the lesion has a large pre-focal bulge [103]. Due to their small radii, microbubbles such as those involved in cavitation are not thought to create tadpole-shaped lesions themselves [76]. However, high heating rates may create boiling bubbles whose presence *is* strongly correlated with tadpole-shaped lesions [76]. Therefore, whether focusing is enhanced by non-linear propagation or inertial cavitation (or both), real-time monitoring of HIFU treatment is essential to prevent distorted lesion formation as well as treatment occlusion.

Treatment duration

As mentioned earlier, the HIFU focus must be moved after each exposure in order to cover an entire tumour. In addition to every exposure having a typical duration of 2-10 s, a cooling time is also necessary to limit thermal build-up in surrounding healthy tissue. This means that currently, more than 5 hours are needed to ablate a 10-cm tumour [98]. However, there is ongoing research in how to best optimise treatment parameters (including scan path, exposure duration and cooling duration). Recent

work suggests that when local thermal deposition is increased, "the reduction in heating time is larger than the subsequent time lost due to the need for additional normal tissue cooling time" [104]. This result validates the approach of harvesting inertial cavitation for increasing the local rate of heating at the focus.

The need for real-time time treatment monitoring

Currently, HIFU is the only truly non-invasive method of destroying deep-seated tumours, and is therefore a treatment with great promise. In contrast with other cancer therapies such as chemotherapy, HIFU is also relatively cost-effective. However, the above discussion has highlighted some challenges in HIFU treatment. While a high rate of thermal deposition is useful in reducing treatment time, it is also crucial that tissue does not reach boiling temperatures. These considerations make real-time monitoring of HIFU is essential. It is important to note that the adopted monitoring strategy should not only be accurate, but it should not impact negatively on the cost-effectiveness or duration of HIFU treatment. With these considerations in mind, existing and prospective methods of monitoring ablative HIFU are next discussed – including the merits of the passive cavitation mapping method presented in the current work.

1.3 HIFU treatment monitoring

There are several imaging modalities that can be used to monitor HIFU treatment. MRI and ultrasound are the most well-developed modalities for this purpose, offering high spatial resolution and large penetration depth without the danger of ionizing radiation. This review is focussed on these two modalities, but other possible approaches are also noted for reference [105; 106; 107; 108; 109; 110].

Even within MRI and ultrasound, many methods or sub-modalities exist for monitoring treatment. It is important to distinguish between methods that estimate temperature (*thermometry*), from which a thermal dose is derived using Equations (1.1,1.2); and those that show changes in tissue properties associated with lesioning (*lesion identification*). Temperature is a familiar measure with which clinicians are comfortable, and current FDA approval requires that temperature be measured during thermal therapy [42]. However, as Section 1.1.3 has shown, the widely used CEM_{43} formulation of thermal dose suffers from errors in the ablation regime. On this basis, lesion identification may be a more sensible approach, however such an image may lack a quantitative measure that is independent of imaging equipment or parameters. Moreover, lesion identification methods require HIFU to be switched off, either to allow the tissue to cool down in the case of MRI, or to avoid interference from the therapeutic ultrasound beam in the case of diagnostic ultrasound.

In the review that follows, the HIFU treatment monitoring methods have been grouped into three categories: MRI, active ultrasound (including B-mode hyperecho) and passive cavitation detection. Of all the methods, only MRI monitoring and B-mode hyperecho (a cavitation-based method) are in current clinical use [42]. Most

methods are based on *differential imaging*, the comparison of a current image with one taken before HIFU exposure. These images are very sensitive to errors arising from motion compensation. Uniquely, the last described method, passive cavitation monitoring, does not require differential imaging, as it is based on the detection of acoustic emissions from cavitating bubbles during HIFU exposure. The real-time nature, high signal sensitivity and low cost of passive cavitation monitoring are contrasted with other available methods. This provides the motivation for the current work, to provide spatial maps of cavitation during HIFU exposure.

1.3.1 Monitoring by Magnetic Resonance Imaging (MRI)

Magnetic resonance (MR) is a widely used medical imaging modality that detects the net magnetic field of atomic nuclei. It is also the current "gold standard" for noninvasive HIFU treatment monitoring [42], and thus widely adopted clinically [111; 112; 113; 114]. Though the physics of MRI is a highly complex topic, a few basic concepts are first presented, to allow a subsequent discussion of the applicability of MRI techniques to HIFU treatment monitoring. For further details, the reader is directed to the works by Hornak [115] and Hashemi *et al.* [116].

MRI Physics

Any spinning charged particle has a magnetic field along the direction of its angular momentum, and a nucleus with unpaired protons will give the nucleus a non-zero net magnetic field. In MRI, the hydrogen nucleus ^{1}H is most often studied because of its high abundance in the human body and from hereon, discussion will be restricted

to these protons. Moreover, "net magnetic field" will refer to the net magnetic field of hydrogen nuclei averaged over an image voxel.

Without an external magnetic field, the magnetic fields of nuclei are randomly and evenly distributed, causing a zero net magnetic field. Application of a high magnetic field B_0 along the (conventionally-named) z-axis will cause nuclei to precess about the +z or -z directions (low and high energy states respectively) at the so-called proton resonant frequency (PRF) associated with B_0. As dictated by the Boltzmann distribution, the ratio of low to high energy state nuclei will be slightly above 1 at body temperature (tending to 1 with increasing temperature). In the absence of another external electromagnetic source, the precession of nuclei will be out of phase with each other, causing a net magnetic field in the +z direction.

It turns out that applying a secondary magnetic field at the PRF transverse to the z-axis allows the nuclei in the low energy state to absorb energy and precess in phase at a certain angle ("flip angle"), decreasing net magnetization in the +z direction and introducing net transverse magnetization. Magnetic resonance imaging relies on applying such a magnetic field and measuring the time-constants associated with the realignment (or relaxation) of net magnetic fields, namely T1, for relaxation along the z-axis, and T2, for relaxation to zero net magnetic field in the x-y plane. The former is also called spin-lattice relaxation time because it depends on the efficiency of energy transfer between the nucleus and the surrounding lattice, while the latter is often termed spin-spin relaxation time because it relies on spin-spin interactions to dephase the precessions. Different tissues have different T1 and T2 characteristics, allowing noninvasive imaging of the body.

MRI monitoring methods

MRI is able to monitor HIFU treatment in several ways. As will be mentioned later, MR elastography suffers from long acquisition times (>20s) and MR cavitation monitoring needs to be verified [117]. T2 images can accurately identify HIFU lesions after tissue has cooled down [118; 119; 117]. Alternatively, temperature maps can be generated during HIFU exposure [120; 121]. Several thermometry methods exist. T1 has been shown to vary linearly with temperature [122] for temperatures below 50°C [42]. The molecular diffusion of water molecules can be imaged using MRI. This provides highly accurate estimates of temperature [123], however, diffusion imaging is very sensitive to motion artefacts. The most widely used method measures slight shifts in the PRF [124; 121]. The proton resonant frequency method compares phase information with prior images, so motion compensation is important to prevent estimate errors [125].

Although MRI can identify lesions accurately after tissue has been left to cool [126; 113; 114], temperature-based monitoring during HIFU treatment (one of the requisites of fast treatment) presents several challenges [121; 127]. One such challenge is the trade-off between temporal and spatial resolution. A low spatial resolution will cause spatial averaging (and therefore underestimation) of peak temperatures. However, with high spatial resolution, monitoring is not real-time and motion artefacts appear. The ExAblateR 2000 (InSightec Inc., Haifa, Israel), a widely used system that was originally deployed for the treatment of uterine fibroids, demonstrates a typical compromise, with 1 mm and sub-Hz spatial and temporal resolutions [40; 128].

Because of limited temporal resolution, MRI-guided HIFU typically uses relatively low acoustic intensities and tries to avoid the high heating rates and unpredictability associated with inertial cavitation [126]. This inevitably lengthens treatment duration. Other drawbacks of MRI are even more difficult to circumvent. MRI is very expensive, not portable, and nothing brought into the operating theatre can be ferromagnetic (including some medical implants such as pacemakers).

1.3.2 Monitoring by active ultrasound

A technically simple and cost-effective method of monitoring HIFU treatment is to use conventional B-mode (or brightness-mode) ultrasound imaging to look for hyperechoes (or "bright-ups") in the images. The rationale and limitations of this technique are first discussed.

Since the acoustic properties of tissue change with temperature and thermal ablation, these changes form the basis of more complex ultrasound-based methods that are next described. In particular, shifts in echo and a change in the level of backscatter occur when temperature is raised (raising the prospect of thermometry), while tissue attenuation and stiffness increase as a result of protein denaturation (which could enable lesion demarcation) [129]. Monitoring the above changes is relatively simple as long as the clinical ultrasound imager provides access to echo data at radio-frequencies (RF), prior to conversion to B-mode. However, the presence of any stabilised bubbles that remain after HIFU is turned off, either due to cavitation or boiling, will greatly confound images [130; 131; 132].

All active ultrasound methods of monitoring HIFU treatment share an important

drawback. Due to the fact that the therapeutic ultrasound intensity is several orders of magnitude higher than typical diagnostic intensities, the therapeutic beam needs to be off while diagnostic pulses are transmitted to avoid interference. Any synchronisation scheme between the two pulses needs to ensure that the HIFU duty cycle is sufficiently high to generate high heating rates while the diagnostic ultrasound method has enough time to generate a whole image.

B-mode hyperecho monitoring

The acoustic impedance of air differs greatly from surrounding tissue, making bubbles very echogenic. This is the reason for which (stabilised) microbubbles are used as ulrasound contrast agents [133]. Similarly, bubbles that have cavitated and grown during HIFU exposure can sometimes be seen on B-mode images as hyperechoic regions after HIFU exposure, providing a means of monitoring treatment [134]. However, unless they are stabilised by boiling, bubbles may have dissolved away by the time pulses are sent to detect it. Moreover, real-time monitoring necessitates that images be taken during HIFU exposure. These two considerations have led to the synchronization of HIFU with diagnostic ultrasound, where HIFU insonation is switched off while diagnostic ultrasound takes an image to avoid interference [135].

Typically a B-mode image is constructed of A-lines taken one after the other, where each A-line is a one-dimensional sequence of pixels extending radially or perpendicularly from the face of the transducer. On most ultrasound imagers, at least one pulse needs to be transmitted for every A-line that is generated [133]. For a 128-element 38 mm aperture array imaging 10 cm into tissue, 1 cm of image width will take over 4 ms to acquire. Therefore, when synchronising HIFU with diagnostic

ultrasound, a compromise is made between the width of interference-free images and the size of bubbles that can be captured (since smaller bubbles will dissolve away earlier).

Although hyperecho correlates with inertial cavitation, the latter is detected using a passive cavitation detector (PCD) before hyperecho is detected [136; 20; 137; 138]. Moreover, hyperecho also correlates with tadpole-shaped lesioning [102], thought to be due to reflection of the HIFU wave by larger, boiling bubbles. Thermocouple data suggests that "inertial cavitation precedes rapid heating up to 110°C at the HIFU focus" [139], after which hyperecho is seen. This suggests that inertial cavitation is a precursor to boiling bubbles that are detected as hyperecho, highlighing the importance of passive cavitation detection as a monitoring tool.

Somewhat surprisingly, hyperecho monitoring does not only suffer from low sensitivity, it can also have a low specificity [140]. This is perhaps due to sub-ablative increases in backscatter, which will be discussed shortly.

Echo-shift thermometry

When tissue is heated, features on the diagnostic ultrasound image such as tissue interfaces and scattering regions change position. This is the joint effect of thermal expansion, a relatively insignificant effect that is usually neglected [141], and changes in speed of sound [142], which is a function of the compressibility and density of the medium.

By calculating the echo strain in the axial direction using cross-correlation techniques borrowed from elastography [143], local changes in speed of sound can be evaluated. Many researchers have sought to demonstrate the feasibility of using

changes in speed of sound to infer temperature [141; 144; 145].

Echo-shift thermometry has some inherent difficulties. The speed of sound in non-fatty tissue has a peak at 50°C [146], making changes in speed of sound hard to evaluate around this temperature, as well as creating a non-unique mapping from speed of sound to temperature. Furthermore, the temperature-dependence of speed of sound is highly variable between different tissues, with lipid content being an especially significant cause of variation [147]. Lastly, irreversible changes in tissue stiffness above 55°C, as described in Section 1.1.3, will make speed of sound a function of thermal dose as well as temperature. Nevertheless, echo-shift thermometry is fast emerging as a cheap alternative to MRI thermometry, and a real-time implementation has been recently achieved [148].

Backscatter thermometry

Assuming density to be a constant with respect to temperature, changes in speed of sound can be directly related to changes in the compressibility of the medium. Using this assumption, it has been predicted that as with the speed of sound, the compressibility contrast between scatterers and bulk medium also increases for temperatures up to 50°C, causing an increase in the backscattered signal [149]. This effect has been demonstrated experimentally [150] and is useful for moderate hyperthermic treatment. However, the decrease in the speed of sound above 50 °C also affects the accuracy of backscatter thermometry. Moreover, in ablative HIFU treatment, where the goal is to denature tissue, it becomes difficult to distinguish between decreasing backscatter and increasing attenuation, resulting in an ill-defined problem.

Attenuation-based lesion identification

Both ultrasonic attenuation and its derivative with respect to frequency – "attenuation slope" – significantly increase for temperatures above 50°C [151; 132; 152; 153; 146]. This effect is due to protein coagulation [152], a process that causes irreversible changes in tissue and can therefore still be detected when tissue returns to body temperature [146].

Attenuation can be estimated by observing the signal energy returning from different depths, while the attenuation slope is derived from the downshift in the centre frequency of the diagnostic ultrasound pulse. Imaging changes in attenuation has shown some promise [154], though further work needs to establish that the method is reliably sensitive [155; 156].

Elastographic lesion identification

Palpation has long been used by doctors as a way of assessing tissue stiffness. Ultrasound elastography is its mechanised extension, where the stiffness of tissue can be imaged by tracking speckle displacements in the RF echo signal of an ultrasound imager during the application of some force [157; 158]. Traditionally, elastography has used quasi-static external compressions, however, the force can also be vibrational or transient, and it can be focused inside the body.

Section 1.1.3 has already described how tissue stiffens as a result of irreversible protein denaturation during thermal ablation. This stiffening can be exploited by elastography to monitor hyperthermic treatment. Elastography has been used to assess thermal damage after RF ablation [159; 160; 161]. It has also been imple-

mented following HIFU treatment of prostate cancer [162], although image contrast was often deemed unsatisfactory.

The results cited above were obtained using quasi-static external compressions. One disadvantage of this is that the stress field created is unknown due to tissue inhomogeneities, introducing artefacts in the stiffness calculations. A solution to this problem is to generate and quantify localised displacements using an acoustic radiation force (ARF) [163]. The ARF (see Section 1.1.5) can be generated by relatively long (up to 10 ms) focused ultrasound pulses from a diagnostic [164] or therapeutic (HIFU) transducer [165; 36], and can successfully detect tissue stiffness changes due to thermal or chemical lesioning. An ARF also arises if two overlapping ultrasound beams are made to oscillate at slightly different frequencies, whereby an audible beat frequency emanating from the intersection of the two beams can be detected using a remote hydrophone [166; 167].

As an alternative to scanning the region of interest with an ARF beam, a procedure that seriously hinders the frame rate of elastographic images, the propagation of the shear wave generated by one or more ARF beams can be imaged using ultrafast ultrasound imaging. By measuring the speed of shear wave propagation as it passes through the region of interest, a map of tissue stiffness is obtained [168; 169].

On the whole, the application of ultrasound elastography during HIFU is a promising approach to treatment monitoring, although, as with other active ultrasound methods, the therapeutic and diagnostic pulses need to be synchronised in a way that the operation of neither is compromised. This limitation can be circumvented if the displacements induced by an acoustic transducer are imaged using

another modality, such as MRI [170; 171]. However, more research is needed to make MR elastography a real-time technique [172].

1.3.3 Cavitation monitoring

The mechanisms via which cavitation, and inertial cavitation in particular, can enhance heat deposition by ultrasound were described in Section 1.1.4. By using focal pressures above the cavitation threshold, cavitation can be used both as a promoter and as a marker of heating, and could therefore also provide a direct indicator of thermal damage. If the cavitation threshold is prohibitively high in the tissue in question, microbubbles can be delivered via the bloodstream to lower the threshold [173; 140].

Although non-acoustic methods of detecting cavitation exist, they are either invasive and thus unsuitable for use *in vivo* or they lack validation [174; 175; 117; 176]. The present discussion is thus concerned with acoustic detection of cavitation, which can either be active or passive, depending on whether a diagnostic pulse is used. Active cavitation detection (ACD) can be a sensitive method under carefully designed experimental conditions that are not designed to mimick cavitation in tissue [177]. However, as already discussed in Section 1.3.2, ACD in the form of B-mode images lacks the required sensitivity to reliably prevent overtreatment.

So far in this chapter, there has been repeated reference to the need to switch off HIFU when generating ultrasound images, in order to avoid interference. Such interference has three components:: backscattering of the HIFU driving signal, backscattering of HIFU harmonics due to non-linear propagation, and cavitation

emissions. Therefore, by using an acoustic receiver recording passively, signals previously avoided as interference can be used to extract useful information about the HIFU exposure. By considering cavitation emissions in particular (discussed in Section 1.1.4), and filtering out other signal components, the receiver becomes a passive cavitation detector (PCD).

Passive cavitation detection

Passive cavitation detection is able to recognise a wide range of bubble behaviours. In fact, much of the knowledge regarding cavitation bioeffects (as presented in Section 1.1.4) was uncovered with the help of passive cavitation detectors.

In the case of inertial cavitation, much of the resulting broadband emission, especially its higher frequency components, is absorbed in the vicinity of the bubble, leading to increased heating. However, the fraction of the emission that is not absorbed is still easily detectable outside the source region, and remains broadband in nature. For instance, insonating a tissue mimicking agar-graphite gel at 1 MHz and 1 MPa peak rarefactional focal pressure (PRFP) causes inertial cavitation emissions whose pressure waves 75 mm away from the bubble have frequency content going beyond 10 MHz [20; 56].

Interestingly, the detected emissions and absorbed emissions are proportional to each other [56]. This means that, if inertial cavitation is the dominant source of heating, the local rate of heating in the focal region of a PCD is proportional to the signal power received by the PCD [21]. Thus, using the bioheat transfer equation [99] to predict temperature rise, a map of thermal dose could be estimated to predict lesioning (see Section 1.1.3). Alternatively, inertial cavitation is observed to "shut

down" as the vapour pressure inside the bubble increases and boiling is approached [21], and increasing tissue stiffness is expected to have a similar effect. Hence, the decrease in signal power with time could also be used to predict lesioning.

Towards spatiotemporal mapping of cavitation

A PCD typically consists of a spherically focussed single element transducer, set to receive only. Therefore, generating a spatial map of cavitation distribution requires mechanically scanning the focus of the receiver over a region of interest, which introduces a severe time-space constraint [178]. Recently, a diagnostic ultrasound array was used as an array of PCDs by turning off transmission [179]. By placing the linear array transversely to the HIFU transducer and using the dynamic receive beamforming algorithm of the imager, cavitation distribution along the HIFU axis could be imaged [78].

Unfortunately, the above method provides limited resolution along the array axis, even when the source is placed closer (at 40 mm distance) to the array [180]. Part of the problem is that conventional imagers typically use a receive subaperture that is half the size of the entire available aperture. Moreover, since the received RF data is dynamically beamformed with depth, integration of the post-beamformed RF data to yield source power creates a trade-off between axial resolution and signal-to-noise ratio.

In contrast to the above approach, the novel cavitation mapping approach at the heart of the present work was developed using a commercially available ultrasound system capable of providing access to simultaneously recorded array data [181; 182; 183]. This allowed the use of a specifically passive beamforming algorithm [184]

on a full aperture. The present work describes the implementation and results arising from this passive cavitation mapping approach, with suggestions for future developments.

1.4 Summary of contributions of the current work

This chapter has presented the bioeffects of ultrasound and shown how high intensity focussed ultrasound (HIFU) can destroy tissue via thermal ablation. Current and prospective methods of monitoring HIFU ablation have been reviewed, with particular attention to their reliability and real-time capability. Since the HIFU focus needs to be moved in small steps to ablate an entire volume of malignant tissue, it is important that at each step, the effect of HIFU ablation is quickly assessed. Therefore, the real-time capability of the monitoring method directly affects treatment time, which is currently of the order of hours.

In reviewing the monitoring methods available to HIFU ablation, a gap in knowledge was identified. Although inertial cavitation greatly increases the rate of heating during HIFU ablation, there is currently no reliable method to monitor the spatial distribution of cavitation during HIFU exposure. Of the two monitoring methods used in clinical practice, MRI tries to avoid cavitation, while B-mode hyperecho is not a sensitive marker of it. Moreover, no active ultrasound method can function while cavitation emissions and other sources of HIFU interference are present. In contrast, broadband emissions recorded on single-element acoustic receivers or passive cavitation detectors (PCDs) can be related to the temperature rise in the focal region of the receiver. This work extends single-element PCDs to an array of

effective PCDs in such a way that reliable maps of cavitation can be generated.

In the following chapters, the theory, implementation, and results of passive cavitation mapping are described. The brief overview that follows also references relevant work (some yet to be published) that this author has co-written.

In Chapter 2, different passive source reconstruction methods are reviewed, and the resolution performance of the chosen passive beamforming method is derived theoretically and simulated. A simple parametric method for estimating the location of a single source based on data acquired with a linear array is also presented [182]. In Chapter 3, the experimental method for passive source mapping is described. Chapter 4 presents passive source maps obtained by exciting a scatterer of known size and location [182]. This provides an absolute and spatial calibration of the linear array, allowing quantitative passive cavitation maps to be generated in subsequent chapters. Chapter 5 shows the results of placing the linear array transversely to the HIFU transducer. High resolution passive maps and resolution of individual cavitation emission traces from several bubbles cavitating simultaneously is achieved [185]. In the last results chapter, Chapter 6, the linear array is placed through a central opening in the HIFU transducer, creating a clinically applicable arrangement. Passive cavitation maps are shown for continuous and disjoint cavitation regions in agar tissue mimicking gel [182; 181; 183], as well as *ex vivo* ox liver [186; 187]. Finally, in Chapter 7, the main achievements of the work are summarised and suggestions are made for future improvements and applications [188; 189].

Chapter 2

Theory and Simulations of Passive Cavitation Mapping

In the previous chapter, the potential usefulness of monitoring the spatial distribution of inertial cavitation activity was outlined, in particular as a means of real-time treatment monitoring during HIFU exposure. When bubbles cavitate inertially inside tissue, they act as broadband sources, whose emissions can be detected by receivers outside the patient. This chapter is concerned with the mathematical problem of using signals received by an array of receivers outside the body to infer the spatial distribution of broadband sources inside the body. It should be noted that, unlike pulse-echo diagnostic ultrasound techniques, which make use of time-of-flight information to infer source location, cavitation sources are excited continuously or quasi-continuously during therapeutic ultrasound exposure. Hence, time-of-flight information can seldom be used to localize these broadband sources, and alternative techniques must be sought to enable cavitation mapping during HIFU exposure.

Section 2.1 presents the formulation of the forward model, namely the remote recording of pressure signals arising from a source field such as a cavitating region. It is argued that beyond the immediate region of the cavitating bubble, the amplitude of the emitted wave is weak enough to be well described by linear propagation. The effect of attenuation is also discussed. Drawing from other research fields, Section 2.2 then reviews existing approaches for solving the inverse problem of reconstructing the source field from such pressure signals.

Finally, Section 2.3 presents the chosen approach based on a variant of passive beamforming to map cavitation using a linear array of receivers focussed in a plane. The resolution of the novel passive cavitation mapping system is then estimated using simple theoretical expressions and its performance is simulated under different conditions.

2.1 The forward model

To be able to reconstruct the distribution of cavitation activity, it is first necessary to describe how acoustic emissions such as those arising from cavitation propagate through tissue before being recorded by acoustic receivers. Since the amplitude of the emitted wave quickly diminishes due to spherical spreading, only small deviations from the ambient pressure and density are expected, so that the propagation process can be described by the linear wave equation (Section 2.1.1).

The linear wave equation is then used in Section 2.1.4 to derive the pressure recorded by a receiver due to the aforementioned acoustic emissions. It is shown that a simple modification of the expression can be used to account for tissue attenuation.

2.1.1 Propagation of radiated pressure waves

Consider a medium that has a velocity field $\mathbf{v}$, as well as pressure and density scalar fields p_a, ρ_a that deviate slightly from their mean values p_0, ρ_0:

$$p_a = p_0 + p, \qquad (p \ll p_0) \tag{2.1}$$

$$\rho_a = \rho_0 + \rho. \qquad (\rho \ll \rho_0) \tag{2.2}$$

Using the above small-signal assumption, the three governing equations of acoustics are obtained in linearised form:

$$p = \kappa\rho, \tag{2.3}$$

$$\frac{\partial \rho}{\partial t} = -\rho_0 \nabla \cdot \mathbf{v}. \tag{2.4}$$

$$\nabla p = -\rho_0 \frac{\partial \mathbf{v}}{\partial t}. \tag{2.5}$$

Equation (2.3) states that the differential pressure (with respect to the mean pressure) is proportional to the differential density by some constant κ. Equation (2.4) uses the principle of mass continuity to state that the change of mass per time in a control volume equals the net flow of mass into the volume. Equation (2.5) uses Newton's second law of motion to state that the net force on a control volume is equal to the acceleration times mass of the particles in the control volume. Combining the above three equations leads to:

$$\nabla^2 p = \frac{1}{\kappa} \frac{\partial^2 p}{\partial t^2} \tag{2.6}$$

which is the well-known linear-wave equation, though it requires two modifications before it can be used in our context. Firstly, by substitution of the travelling wave equation into Equation (2.6), it is realised that $\kappa = c^2$, where c is the speed of sound propagation. Secondly, Equation (2.6) is in the *homogeneous* form of the linear wave equation, that is, it lacks a source term. If energy is converted to acoustic energy (such as in thermoacoustics [190]), a source field term s is added that varies with position $\mathbf{r}$ and time t [191]:

$$\nabla^2 p - \frac{1}{c}\frac{\partial^2 p}{\partial t^2} = -s(\mathbf{r}, t), \tag{2.7}$$

In the current context, $s(\mathbf{r}, t)$ represents the acoustic emissions created by cavitation, where acoustic energy from the primary HIFU signal (typically around 1 MHz) is converted to broadband emissions by the inertially cavitating bubble. More specifically, $s(\mathbf{r}, t)$ gives the rate of change of mass outflow per unit volume [192], and is also called the source field. Integrating the source field over a volume $\mathcal{V}$ will yield the rate of change of mass flow out of that volume (in kg s^{-2}), also called the source strength, or $q_{\mathcal{V}}(t)$ [192].

2.1.2 Modelling bubbles as acoustic sources

In the case of cavitating bubbles, the question arises as to what kind of sources they should be modelled as. For purely radial motion, bubbles could be treated as simple spherical sources whose radiation, as far as remote detectors are concerned, is equivalent to that generated by point sources. That is, a bubble of strength $q(t)$ at $\mathbf{r}_s$ would give rise to a source field $s(\mathbf{r}, t) = q(t)\delta(\mathbf{r}_s)$, where $\delta(\mathbf{r})$ is the

multidimensional Dirac delta, or impulse function. Accordingly, several bubbles can be modelled as creating a source field that consists of several spatial impulse functions. However, any source mapping algorithm will create spatial blurring or integration over these spatial impulse functions. Therefore, it is more practical if the inverse problem generates estimates of a source strength field $q(\mathbf{r}, t)$ which is zero everywhere except for peaks corresponding to actual values of source strength $q_k(t)$ for bubbles $k = 1, \ldots, K$. Even if the number of bubbles is so large as to be intractable, the generality of this formulation is preferred over the estimation of the source field, which becomes meaningless in the case of discrete point sources.

2.1.3 Power radiated by cavitating bubbles

Due to its role in heating, this thesis is primarily concerned with the acoustic power radiated by bubbles. For the source strength field $q(\mathbf{r}, t)$ defined in Section 2.1.2 and considered over a time period $[t_0, t_0 + T]$, the radiated power is given by [192]

$$\psi(\mathbf{r}) = \frac{\langle q^2(\mathbf{r}, t) \rangle}{4\pi\rho_0 c} = \frac{1}{4\pi\rho_0 c T} \int_{t_0}^{t_0+T} q^2(\mathbf{r}, t)\ dt \tag{2.8}$$

Thus, in addition to estimating the source strength field, a prime concern of passive mapping is to estimate the source power field $\psi(\mathbf{r})$, whose peaks correspond to the power emitted by individual bubbles or bubble clusters. This approach has similarities to the concept of the *source intensity field* in *Time Exposure Acoustics* [184; 193]. However, in the current work, the concept of source power is presented as a physical quantity rather than the arbitrary units most often encountered in literature.

2.1.4 Detection of radiated pressure waves

As the previous subsection has shown, the source field influences the pressure field outside the source region. Since the wave equation is a linear differential equation, any linear combination of solutions will also be a solution. This means that the pressure field response to an impulse source disturbance at $(\mathbf{r}', t')$, the so-called Green's function, can be convolved with the actual source field $s(\mathbf{r}, t)$ to yield the pressure field at $(\mathbf{r}, t)$. Specifically, the Green's function of Equation (2.7) is [191; 194]

$$g(\mathbf{r}, t|\mathbf{r}', t') = \frac{1}{4\pi|\mathbf{r} - \mathbf{r}'|}\delta\left(|\mathbf{r} - \mathbf{r}'|/c - (t - t')\right) \tag{2.9}$$

so that the pressure field $p(\mathbf{r}, t)$ in response to a source field $s(\mathbf{r}, t)$ is

$$p(\mathbf{r}, t) = \int_{\mathcal{V}} \frac{1}{4\pi|\mathbf{r} - \mathbf{r}'|} s\left(\mathbf{r}', t - |\mathbf{r} - \mathbf{r}'|/c\right)\ d\mathbf{r}' \tag{2.10}$$

with $\mathcal{V}$ a volume enclosing the source region. The implication of Equation (2.10) is that the pressure at a particular location and time will be the spatial integral of all sources in the source region, each source being time delayed by the relevant propagation time and weakened by spherical spreading.

Piezoelectric elements, such as those found in the transducer heads of medical ultrasonic imagers, convert the pressure signal that they experience to a voltage trace [195], which can then be amplified and digitized for storage. Since the processes of acoustoelectric conversion and amplification are frequency-dependent, it is useful at this point to convert Equation (2.10) into the temporal frequency domain using the Fourier transform:

$$P(\mathbf{r}, f) = \int_{\mathcal{V}} \frac{1}{4\pi|\mathbf{r} - \mathbf{r}'|} \exp\left(-j2\pi f|\mathbf{r} - \mathbf{r}'|/c\right) S\left(\mathbf{r}', f\right) \, d\mathbf{r}' \tag{2.11}$$

Then, for a point receiver at $\mathbf{r}$, the voltage signal can be modelled as the pressure $P(\mathbf{r}, f)$ experienced by the receiver multiplied by a frequency response. If the receiver centred at $\mathbf{r}$ has instead a finite size, its signal can be modelled as arising from an integral of pressures over its surface, the so-called Rayleigh integral [196; 197]. This will give rise to a spatially dependent frequency response $H(\mathbf{r}, f)$. In general, then, for a source region $\mathcal{V}$ the voltage $V(\mathbf{r}, f)$ generated can be expressed as:

$$V(\mathbf{r}, f) = \int_{\mathcal{V}} B(\mathbf{r} - \mathbf{r}', f) \exp\left(-j2\pi f|\mathbf{r} - \mathbf{r}'|/c\right) S\left(\mathbf{r}', f\right) d\mathbf{r}' + N(f) \tag{2.12}$$

$$B(\mathbf{r}, f) = \frac{1}{4\pi|\mathbf{r}|} H(\mathbf{r}, f) \tag{2.13}$$

where $B(\mathbf{r}, f)$ combines the processes of spherical spreading, acoustoelectric conversion and signal amplification, while the complex exponential term causes a phase shift arising from the propagation delay, and $N(f)$ represents electrical noise.

2.1.5 The role of attenuation

So far, a simplified model of linear propagation has been given that has not taken into account the effect of attenuation. However, a significant portion of the broadband emissions from inertially cavitating bubbles is attenuated before reaching the receivers, much of it converted into heat. To incorporate attenuation in the above forward model, a frequency-dependent attenuation coefficient $\alpha(f)$ can be included, which causes an exponential weakening of the signal with distance [198]:

$$V(\mathbf{r}, f) = \int_{\mathcal{V}} B(\mathbf{r} - \mathbf{r}', f) \exp\left(-j2\pi f|\mathbf{r} - \mathbf{r}'|/c\right) S\left(\mathbf{r}', f\right) d\mathbf{r}' + N(f) \quad (2.14)$$

$$B(\mathbf{r}, f) = \frac{\exp(-2\alpha(f)|\mathbf{r}|)}{4\pi|\mathbf{r}|} H(\mathbf{r}, f) \quad (2.15)$$

When considering the total acoustic power transmitted by a cavitating bubble, let the receivers be estimated as being at an equal distance from the bubble, thereby sampling the pressure on a spherical surface. The total power radiated by the bubble is then split into the power that reaches the spherical surface (*received source power*) and the power that is attenuated along the way, some of it by absorption.

Ultimately, the aim of passive mapping should be to estimate the local rate of heating from the source power absorbed in the immediate vicinity of the cavitating bubble. Therefore, even if attenuation was correctly compensated for, a scaling factor would be needed to convert the total source power estimate into the absorbed source power [56].

Unfortunately, the array used in the current work had a 5-10 MHz response that did not allow detection of emissions at higher frequencies, and this made attenuation correction difficult. Therefore, it was thought that relating the received source power to absorbed source power should be left to future work.

For this work, the attenuation coefficient was set to zero so that estimates of source power represent the received source power. Nevertheless, the attenuation term has been kept in the formulation to show how calculations are modified if full bandwidth data was available and attenuation compensation is attempted.

2.2 The inverse problem

The problem of reconstructing the source field $S(\mathbf{r}, f)$ by using pressure recordings outside the source region and a forward model such as Equation (2.14) is known as the inverse source problem [199]. Unfortunately, even with an infinite number of uniform frequency response noiseless point receivers, the mapping from a 4-dimensional source field to a 3-dimensional measurement space creates an ill-defined problem [191; 200]. This means that the solution needs some additional information or constraints, which can include *regularization*, that is, the constraint of smoothness, typically over space. A formulation for estimating the strength of a single source is first presented, which forms a natural introduction to existing methods of source field reconstruction.

2.2.1 Passive beamforming for single source reconstruction

Assume the source field $S(\mathbf{r}, f)$ consists of a single point source of known location $\mathbf{r}_s$. As argued in Section 2.1.2, this is a valid model for a radially oscillating bubble. Then, the source field reduces to the product of a shifted Dirac delta function and a source strength $Q(f)$, whose estimate is sought:

$$S(\mathbf{r}, f) = \delta(\mathbf{r} - \mathbf{r}_s)Q(f). \tag{2.16}$$

For receiver elements $i \in \{0 \dots I-1\}$ at positions $\mathbf{r}_i$, where each element has equal characteristics, the recorded voltage $V_i(f)$ according to Equation (2.14) is:

$$V_i(f) = B(\mathbf{r}_s - \mathbf{r}_i, f) \exp\left(-j2\pi f|\mathbf{r}_s - \mathbf{r}_i|/c\right) Q(f) + N_i(f) \quad (2.17)$$

$$B(\mathbf{r}, f) = \frac{\exp(-2\alpha|\mathbf{r}|)}{4\pi|\mathbf{r}|} H(\mathbf{r}, f) \quad (2.18)$$

where $N_i(f)$ is the noise term associated with receiver i. Assuming a known noise power spectrum $|N(f)|$ that is the same for each receiver signal, the minimum variance estimate $\tilde{Q}(f)$ of the source strength $Q(f)$ is:

$$\tilde{Q}(f) = \mathbf{w}^T(f)\mathbf{V}(f) \quad (2.19)$$

$$w_i = \frac{1}{I} C(\mathbf{r}_s - \mathbf{r}_i, f) \exp\left(j2\pi f|\mathbf{r}_s - \mathbf{r}_i|/c\right) \quad (2.20)$$

$$C(\mathbf{r}, f) = \frac{1}{B(\mathbf{r})} \frac{|V_i(f)|^2}{|V_i(f)|^2 + |N(f)|^2} \quad (2.21)$$

with $C(\mathbf{r})$ being a compensation term incorporating a Wiener filter.

Equation (2.19) above presents the so-called *passive beamformer*: in order to recover the source strength, the signal from each receiver is

(i) back-propagated to the source location using the complex exponential (which corresponds to a delay in the time domain);

(ii) multiplied by a compensation term $C(\mathbf{r}_s - \mathbf{r}_i, f)$ to account for attenuation and receiver response effects;

(iii) coherently added to reduce noise.

Although the passive beamformer was presented here in the frequency domain, it is also readily implementable in the time domain. With $\mathrm{c}(\mathbf{r}_s - \mathbf{r}_i, t)$ as the time

domain equivalent of the compensation term and $*_t$ denoting temporal convolution, the time domain beamformer is

$$\tilde{q}(t) = \frac{1}{I}\sum_{i=0}^{I-1} \mathrm{c}(\mathbf{r}_s - \mathbf{r}_i, t) *_t v_i(t - |\mathbf{r}_s - \mathbf{r}_i|/c) \tag{2.22}$$

2.2.2 Beamforming for source field reconstruction

The previous sub-section presented a way to estimate the source strength of a single point source of known location by an array of receivers. Such an approach is called *passive beamforming* since, by analogy of focussing wave transmission, appropriate delaying of receiver signals also produces a spatially focussed beam [201].

In the case of single source reconstruction, the beam focus can be placed at the source location. By moving the focus around a source field consisting of several point sources, a source strength field estimate $\tilde{Q}(\mathbf{r}, f)$ is obtained, with peaks in signal energy corresponding to estimates of source strengh for individual sources. If the source field is continuous, a scaling factor corresponding to the spatial blurring caused by passive beamforming is needed to convert $\tilde{Q}(\mathbf{r}, f)$ to an estimate of the source strength density field $\tilde{S}(\mathbf{r}, f)$.

A generalization of passive beamforming allows the use of different weights A_i for each receiver element. The use of such weights, termed *apodization*, modifies the source strength estimate at $\mathbf{r}$ as

$$\tilde{Q}(\mathbf{r}, f) = \mathbf{w}^T(f)\mathbf{V}(f) \tag{2.23}$$

$$w_i = A_i C(\mathbf{r} - \mathbf{r}_i, f) \exp\left(j2\pi f|\mathbf{r} - \mathbf{r}_i|/c\right) \tag{2.24}$$

$$\sum_{i=0}^{I-1} A_i = 1 \tag{2.25}$$

In many research fields, the source field is *narrowband*, with only slight deviations from a centre or carrier frequency f_0, and can be expressed as a complex signal

$$s(\mathbf{r}, t) \exp(j2\pi f_0 t) \tag{2.26}$$

In such a case, the frequency-domain beamformer can be used at the frequency f_0, since the propagation process can be approximated to depend only on the carrier frequency. There are two possible implementations for a broadband source field, such as that arising from cavitation. Firstly, the beamformer can be implemented for each frequency bin in the Fourier domain, with the resulting signal transformed back to the time domain [202; 203]. This is a computationally expensive procedure; however, as will be shown, most acoustic reconstruction methods have been developed for narrowband sources. Alternatively, the beamformer can be adapted to the time domain (2.22):

$$\tilde{q}(\mathbf{r}, t) = \sum_{i=0}^{I-1} c(\mathbf{r}_s - \mathbf{r}_i, t) *_t v_i(t - |\mathbf{r}_s - \mathbf{r}_i|/c) \tag{2.27}$$

With estimates of the source field, the source power field (2.8) can now be estimated for a single frequency or over all frequencies, by integration over the time or frequency domains (which give equivalent results due to Parseval's theorem):

$$\tilde{\Psi}(\mathbf{r}, f) = \frac{1}{4\pi\rho_0 c}|\tilde{Q}(\mathbf{r}, f)|^2 \tag{2.28}$$

$$\tilde{\psi}(\mathbf{r}) = \frac{1}{4\pi\rho_0 cT}\int_{t_0}^{t_0+T} \tilde{q}(\mathbf{r}, t)^2 \; dt = \frac{1}{4\pi\rho_0 c}\int_{-\infty}^{\infty} \tilde{\Psi}(\mathbf{r}, f) \;\; \mathrm{d}f \tag{2.29}$$

The above definitions make it possible to quantify the concept of a receive beam, namely, the ratio of signal power that is received from source locations $\mathbf{r}_s$ to the signal power received when the source is at the beam focus $\mathbf{r}$. In line with common usage, this ratio is defined as the *psf* (point spread function) of the beamformer. For a single frequency, the *psf* is given as

$$PSF(\mathbf{r}, \mathbf{r}_s, f) = \tilde{\Psi}(\mathbf{r}, f)/\Psi(\mathbf{r}_s, f) \tag{2.30}$$

while the *psf* of a broadband signal is obtained from the ratio of source powers integrated over time or frequency

$$psf(\mathbf{r}, \mathbf{r}_s) = \tilde{\psi}(\mathbf{r})/\psi(\mathbf{r}_s) \tag{2.31}$$

The quantification of beam shape using the point spread function allows us to discuss the usefulness of the apodization weights A_i. Although the conventional passive beamformer (2.19-2.22) calls for uniform receiver weights to minimise signal noise (so-called *matched processing*), changing A_i allows adjustment of the receive beam, with a trade-off between central beam size and magnitude of sidelobes. The receive beam can also be adjusted to avoid interference from sources near the location of interest $\mathbf{r}$. A class of beamformers called adaptive beamformers use the received signal to adapt the apodization weights in such a way. In particular, for narrowband

signals, the *Capon* or *MVDR* (Minimum Variance Distortionless Response) beamformer minimises the source power according to the constraint $\sum_{i=0}^{I-1} A_i^2 = 1$ (note that after optimization, A_i should be re-scaled according to (2.25)). Fortunately, the minimisation has a simple analytical solution involving the array signal $\mathbf{V}(f)$ covariance matrix [204].

Since the *psf* causes blurring of the source power map, the question arises whether some de-blurring could be applied. When the *psf* is *space-invariant* (constant for constant $\mathbf{r}-\mathbf{r}_s$), this is indeed possible with *deconvolution*, a well-researched topic with a wealth of techniques [205; 206]. This psf will be independent of the frequency content of the source field if it is also *frequency-invariant*, giving a *psf* that is known *a priori*. Since, as will be seen in Section 2.3, the *psf* depends on the array aperture, beamformer focus, and source frequency, the effective array aperture over which beamforming is carried out can be varied with focal distance and frequency to achieve a space- and frequency-invariant beam [207; 208]. However, synthesis of such a beam involves reducing the beamforming aperture for higher frequencies and shorter focal distances, where the *psf* is narrower. Thus, the operation effectively chooses the worst *psf* available over the focal distance and frequency space, and assigns it over the entire variable space, rejecting array information for source locations where the inverse source problem is better defined. Nevertheless, it is possible that the application of deconvolution to such degraded images will create images superior to those obtained using conventional passive beamforming.

2.2.3 Reconstruction of discrete point sources

As has been shown in Section 2.2.1, passive beamforming is based on the implicit assumption that the only source in the field is the one currently being reconstructed. Therefore, an extension of passive beamforming is to assume a finite set $k \in \{1 \dots K\}$ of point sources with locations

$$\mathbf{R} = [\mathbf{r}_1 \cdots \mathbf{r}_K]. \tag{2.32}$$

For a vector of narrowband sources $\mathbf{q}(t)$, the single-source model of Equation (2.17) can be extended to multiple sources whose propagation can be described by a system of linear equations:

$$\mathbf{v}(t) = M(\mathbf{R})\mathbf{q}(t) + \mathbf{n}(t) \tag{2.33}$$

$$M(\mathbf{R})_{i,k} = B(\mathbf{r}_k - \mathbf{r}_i, f_0) \exp\left(-2j\pi f_0 |\mathbf{r}_k - \mathbf{r}_i|/c\right) \tag{2.34}$$

where $M(\mathbf{R})$ is a function of the source positions $\mathbf{R}$. There are two ways in which the above model can be used. Firstly, a grid of postulated source positions $\mathbf{R}$ can be used. This grid corresponds to the pixels or voxels of a sampled source field that is sought. The matrix $M(\mathbf{R})$ can then be inverted using Tikhonov regularization [209; 210] to yield the sampled source field. Unfortunately, the number of receivers available is likely to be much lower than the number of grid points required for a well-resolved image, making the problem extremely ill-posed.

Alternatively, for a discrete number K of actual point sources (assumed smaller than the number of receivers I) the source locations $\mathbf{R}$ can be estimated. Once

$\mathbf{R}$ is obtained, the signals $\mathbf{q}(t)$ can be easily estimated as before with Tikhonov regularization, from which the discrete source power field is obtained. Therefore, the review now focusses on the two widely used approaches to estimate the number K of sources and their locations $\mathbf{R}$. For further details, the reader is referred to the excellent review of [204].

One set of methods for source localization are known as the *subspace-based methods*. Here, the basic idea is that for statistically independent source and noise, the array signal covariance can be decomposed into two groups of eigenvector-eigenvalue pairs, one containing signal eigenpairs (the signal subspace), and the other noise eigenpairs (the noise subspace). Assuming zero-mean σ^2-variance white noise $N_i(f)$ that is uncorrelated with noise from other elements, the decomposition will produce K eigenpairs arising from the K sources, as well as $I - K$ noise eigenpairs, with each noise component having an eigenvalue of σ. This property allows counting of the number of sources, with information theoretic criteria such as MDL (minimum description length) [211] requiring no prior knowledge of σ.

Upon estimation of the number of sources K and subsequent identification of the source subspace (eigenpairs with the K largest eigenvalues), the source locations need to be estimated. In the MUSIC (MUltiple SIgnal Classification) algorithm, the observation is made that for the correct set of source locations $\mathbf{R}$, the columns of the matrix $M(\mathbf{R}, f)$ (2.33) are orthogonal to the noise eigenvectors [204], so that their dot product is zero. This property is used to define a function in location space whose roots should correspond to the locations of the sources. In practice, the array signal covariance can only be estimated, and one finds the K smallest minima [212].

Due to its simplicity and small search space, the MUSIC algorithm has found wide acceptance. However, subspace-based methods such as MUSIC suffer from two challenges: accurate estimation and subsequent decomposition of the array signal covariance matrix can be computationally expensive; moreover, if the source signals are correlated, the sources cannot be well separated using covariance [204]. The latter problem can be solved by computing higher-order statistics of the signal [213; 214; 215; 216; 217], assuming these are non-zero, with the added advantage that any Gaussian additive noise can be filtered out (since a Gaussian process lacks higher-order statistics). However, accurate estimation of higher-order statistics requires longer sample sizes and computation times.

The incorporation of higher-order statistics into source localization effectively incorporates more information about the signal than the covariance conveys. This raises the interesting question whether the source signal has a structure known *a priori* that can be used to aid localization. For instance, there exists a class of random processes which display stationarity only at a certain cycle, termed *cyclostationary processes*. More specifically, a process is N-order cyclostationary if all its statistics to the Nth order repeat cyclically [218]. In other words, for a signal $q(t)$ of cycle T and expectation operator $E\langle . \rangle$,

$$E\langle q(t)^n \rangle = E\langle q(t - iT)^n \rangle \text{ for } n \leq N, i \in \mathbb{Z} \tag{2.35}$$

Cavitation due to a cyclic ultrasound field could exhibit this property, in which case the cyclic statistics of the signal can be fed to MUSIC [219], or even adaptive multi-stage beamformers that sequentially extract one source after the other [220].

In addition to subspace methods, another important class of localization methods exists, namely ML (maximum likelihood). Here, a likelihood function is constructed that expresses the probability of receiving the array data given the source parameters [221; 212; 204]. If the number of sources has already been estimated using the subspace method described earlier, the source parameter over which the likelihood function is minimsed consists of the source locations $\mathbf{R}$ and noise variance σ^2. Depending on the assumptions used, the ML estimator can be a noise-regularized minimization of the linear system's error norm integrated over the recording time $[t_0, t_0 + T]$:

$$\arg\min_{\mathbf{R},\sigma^2} \left\{ I \log \sigma^2 + \frac{1}{\sigma^2 T} \int_{t_0}^{t_0+T} \|\mathbf{v}(t) - M(\mathbf{R})\mathbf{q}(t)\| \, \mathrm{d}t \right\} \tag{2.36}$$

While such optimization can provide accurate estimates of source locations, the author is not aware of an efficient optimization strategy for 2D localization.

Although there is a wealth of literature on discrete sources localization, the linear system formulation (2.33) on which discrete source localization methods are based presents several significant challenges. Firstly, the model of propagation presented in Equation (2.33) is only valid for narrowband sources, so that for a broadband source such as a cavitating bubble, estimates need to be combined for many frequency bins [222]. The system of linear equations could be written using the z-transform, with the matrix inverse converted to a set of time-domain filters, however the difficulty of converting arbitrary z-domain filters into the time domain may make this impractical for a large number of sources.

Most important of all, the validity of assuming spatially discrete sources needs

to be questioned. Since spherically collapsing bubbles can be treated as spherical monopole sources, the assumption would at first appear to hold, however, the concentration of bubbles could be so large as to appear to act as a spatially continuous source field, in which case the problem may become intractable using the discrete sources assumption. In such a case, a spatially parameterized source field distribution model may present a solution. There exists work that assumes a single Gaussian-distributed source field whose parameters are then estimated [223; 224], however this assumption is deemed too restrictive in the case of HIFU-induced cavitation where inhomogeneities in tissue could create several regions of cavitation.

2.3 Passive source mapping with a linear array

2.3.1 Choosing the right algorithm

The previous section has considered several existing methods to reconstruct a source field using an array of detectors. These methods are extensively used in passive sonar and radar, noise mapping, and geophysics, to localise or map animals, vehicles, earthquakes, and other sources of sound [225; 204; 226; 227; 228].

Recently, advances in medical ultrasonic devices have raised the exciting possibility of applying these passive techniques to localise and characterise cavitating bubbles. Using a medical ultrasonic linear array placed at right angles to a HIFU transducer and with pulse transmission off, Farny was able to generate bubble distributions along the HIFU axis [179; 78]. Unfortunately, access was only available to post-beamformed RF data using the so-called "dynamic receive beamforming"

algorithm optimised for active imaging, with a beamforming aperture half the size of the entire available aperture. This limited the system to resolving sources transversely to the linear array. Moreover, since dynamic receive beamforming varies the receive focus dynamically, this causes two significant problems: firstly, the source signal is distorted, making cavitation characterization based on frequency content ambigious; secondly, the effective integration time in (2.8) is limited, giving noisy source power maps.

In order to provide 2-D maps of cavitation, access to simultaneous recordings of receiver array data – so-called *channel data* – is necessary. Previously, this capability was restricted to a few custom-built, expensive research platforms, such as the RASMUS system at the Technical University of Denmark [229], or the DiPhAS system at the Fraunhofer Institute in Germany [230]. Thankfully, the recent introduction of a commercially available ultrasound system (z.one, Zonare, Mountain View, CA) z.one ultrasound system from Zonare has broadened the availability of channel data. Thus, for the first time, a diagnostic ultrasound array could be placed co-axially with the HIFU transducer with the possibility of resolving cavitation distributions in 2D using a setup that can be directly transferred to the clinic.

With the above capability in place, the question must be asked as to which of the passive source reconstruction methods discussed in Section 2.2 should be adopted. The adopted method should be simple and mathematically robust, acting as a proof of concept, and yet return physically meaningful spatial maps of broadband source distributions. Since the method is chosen with a view to an eventual real-time and online implementation, a frequency-based method that requires decomposition of

the broadband source into narrowband components is not an option. Computation time should also be fixed, precluding the use of iterative methods.

The above needs of the current work are best met by passive beamforming, and in particular, *Time Exposure Acoustics* [184], where passive beamforming is explicitly used as a means to reconstruct a so-called source intensity field from broadband near-field data. This work therefore adopted the Time Exposure Acoustics formulation, with two slight modifications. Firstly, the original formulation contains a subtraction term involving the variances of the array signals, with the aim of removing a "DC bias" from the images. This term lowers the source intensity estimates at the source locations, and was therefore omitted. Secondly, the current formulation incorporates a scaling factor to generate estimates in units of power (see Equation (2.8)) rather than the unspecified units of source intensity. In order to distinguish the current method from other variations of passive beamforming, the term *passive source mapping* is adopted, which becomes *passive cavitation mapping* in the case of cavitation sources. It should be noted that the method does not only generate maps of source power, but also temporal variation of source strength, as explained in the following sub-section.

Although, due to the aforementioned clinical needs (as well as consistency), passive source mapping was used throughout this thesis, the access to simultaneously recorded array data also makes it possible to research spatiotemporal cavitation dynamics in a laboratory environment, where some of the above needs can be relaxed. For this reason, the application of the more advanced source reconstruction methods detailed in Section 2.2 will be the focus of future research.

2.3.2 Implementation on a linear array

What follows is a presentation of the passive source mapping algorithm as applied to the linear array used in the work. However, the algorithm can be simply modified to any array geometry.

Linear array geometry

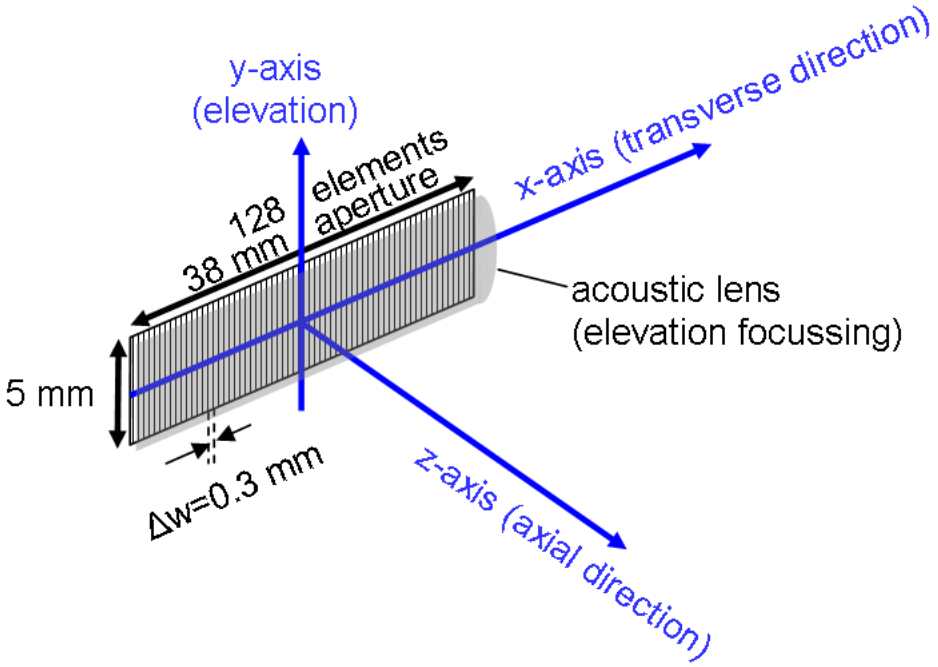

Figure 2.1: The linear array used to generate passive maps. The array has an aperture of 38 mm consisting of 128 elements, each with a 5–10 MHz frequency response. At any time, 64 out of the 128 elements can be connected to recording channels. For the purpose of generating passive maps, the recording channels were chosen to span the entire array. An acoustic lens provides cylindrical focussing in the elevation direction, with a focal length of $z = 17.5$ mm. The sources are assumed to be in the far-field of the receivers.

Figure 2.1 shows a schematic of the linear array used during the experiments (L10-5, Zonare, Mountain View, CA), with the co-ordinates chosen to simplify the

mathematical formulations. A uniformly spaced linear array of 128 receivers spanning an aperture of $D = 38$ mm lies along the x-axis, with the centre of the array at the origin. The width of the elements is less than 0.3 mm in the transverse (x) direction and 5 mm in the elevational (y) direction. Elevational focusing is provided by an acoustic lens, with a focal length of 17.5 mm [231]. Each element has a nominal 5-10 MHz response. The spatial and frequency sensitivities of the array elements will be experimentally investigated in Section 4.1.1.

Given the above system parameters and the assumption of appropriately loud sources further than 30 mm from the array, the receivers were modelled as noiseless point receivers with uniform (unity) response in the 5-10 MHz range. The point receiver model is later validated in Section 4.1.2, where it is shown that despite a 10 mm thick imaging plane, the received pressure scales with the inverse of distance.

With only 64 recording channels (see Appendix A), the elements connected to the channels are chosen to span the entire 38 mm aperture in order to optimise resolution. These elements are arranged near-uniformly from $x = -18.75$ mm to $x = 18.75$ mm:

$$x_i = \begin{cases} (-62.5 + 2i)\Delta w & \text{for } i \in \{0 \dots 31\} \\ (-63.5 + 2i)\Delta w & \text{for } i \in \{32 \dots 63\} \end{cases} \tag{2.37}$$

$$\Delta w = 0.3 \text{ mm} \tag{2.38}$$

For clarity in later expressions, a distance function is defined that expresses the distance from receiver element i to a point (x, z) in the imaging plane:

$$d_i(x, z) = \sqrt{(x_i - x)^2 + z^2} \tag{2.39}$$

Passive source mapping algorithm

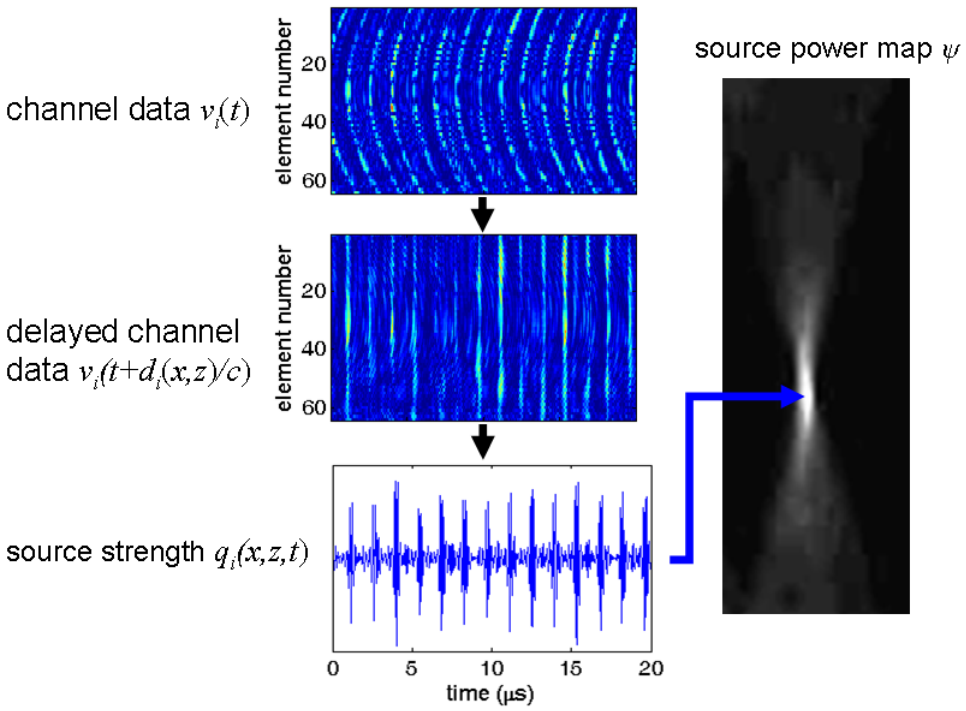

Figure 2.2: The passive mapping algorithm. The channel data shows emissions from a single bubble cavitating periodically. For each pixel location in the source power map, the appropriate time delays are used to create a reconstructed source strength, whose mean square value is then taken. See text for further details.

The passive source mapping algorithm, as depicted in Figure 2.2, can now be presented. For a point (x, z) in the imaging plane, the signals $v_i(t)$ from the 64 channels are first delayed according to the relevant propagation times and then summed. Assuming a constant pressure sensitivity b over the 5-10 MHz response of the array leads to the following estimate of the source strength at (x, z, t) (2.22):

$$\tilde{q}(x, z, t) = \frac{4\pi}{64b} \sum_{i=0}^{63} d_i(x, z)\ v_i(t + d_i(x, z)/c) \tag{2.40}$$

where b is a calibration factor that converts the voltage RF signal to the pressure

experienced by the element. The factor is analogous to the frequency and spatially dependent term B in (2.18), with the difference that b is a constant that assumes no absorptive or scattering attenuation. Furthermore, the mapping only considers the portion of the source field that is in the 4.6-9.6 MHz recording band of the IQ data, with a uniform frequency response of the array over this band (see Section). The value of the calibration factor b, as well as the validity of the above assumptions, will be ascertained in Chapter 4.

The corresponding value of source power is estimated by taking a scaled mean square of the source strength over some integration time period $[t_0, t_0 + T]$, as in (2.8):

$$\tilde{\psi}(x,z) = \frac{1}{4\pi\rho_0 cT}\int_{t_0}^{t_0+T} \tilde{q}(x,z,t)^2 \mathrm{d}t \tag{2.41}$$

In the actual application, the channel data is available at a 50 MHz sampling rate (see Appendix A). To avoid errors due to delay quantization, the signals are upsampled using cubic interpolation to 200 MHz before delaying the signals to the nearest available indices. The source strength itself can be generated at a lower sampling frequency of 50 MHz. Thus, an integration duration of T=20 µs is approximated using the summation of 1000 data points.

Parametric single source localization

Figure 2.2 has shown the channel data received when a single bubble was periodically cavitating from a fixed location. It can be seen that the pressure wave from each cavitation event reaches the array elements with a delay curvature. Clearly, if

the bubble was sufficiently far away, the pressure wavefront reaching the array elements would be planar (the far-field or Fraunhofer assumption), with the wavefronts registering as lines in the channel data. Closer to the array, if the propagation time from a source at (x_s, z_s) to an array element at $(x, 0)$ is referenced to some array position $(x_0, 0)$:

$$\frac{1}{c}\left(\sqrt{z_s^2 + (x - x_s)^2} - \sqrt{z_s^2 + (x_0 - x_s)^2}\right) \tag{2.42}$$

then using the Fresnel approximation

$$\sqrt{z_s^2 + (x - x_s)^2} \approx z_s + \frac{(x - x_s)^2}{2z_s} \tag{2.43}$$

the difference in propagation delays is given by

$$\frac{1}{2z_s c}\left((x - x_s)^2 - (x_0 - x_s)^2\right) = \frac{1}{2z_s c}x^2 - \frac{x_s}{z_s c}x + \frac{2x_0 x_s - x_0^2}{z_s c} \tag{2.44}$$

in other words, a quadratic function with co-efficients

$$\left[\frac{1}{2z_s c}, -\frac{x_s}{z_s c}, \frac{2x_0 x_s - x_0^2}{z_s c}\right] \tag{2.45}$$

whose curvature is determined by the axial distance z_s to the source and whose minimum is given by the transverse position x_s of the source.

The above result suggests a way to quickly estimate the position of a single source: take the cross-correlation of one of the data channels at $(x_0, 0)$ with the rest of the channels and find the maximum value of each cross-correlation to yield relative times of arrival; retrieve the coefficients of the parabola by performing a

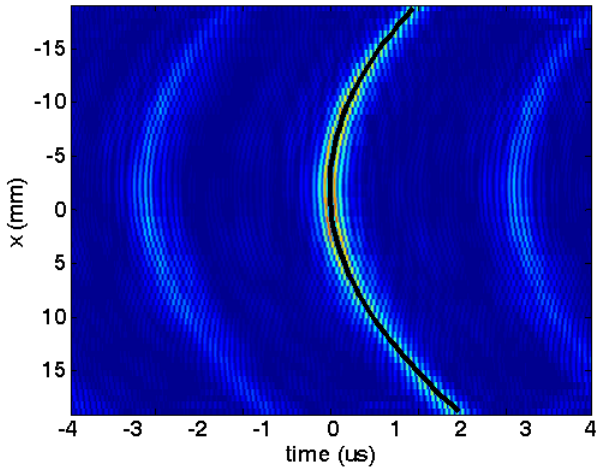

Figure 2.3: Parametric single source localisation based on parabolic curvature of arrivals. The cross-correlation of one data channel with the other channels (in this case channel 32) is used to fit a parabola to the curvature of arrivals. From the parabola co-efficients, the source location can be recovered. See text for further details.

least-squares fit; retrieve (x_s, z_s) from the coefficients of the parabola. An example for a cavitating bubble with an estimated location of (-2,72) mm is shown in Figure 2.3.

This technique will be extensively used in Chapter 4 for the localisation of single scatterers. In addition, since passive beamforming is equivalent to summing all the possible cross-correlation pairs evaluated at the appropriate time delays [184], taking the cross-correlation of one channel with the rest of the channels also provides a rapid way of checking the quality of the recorded data (as illustrated later in Figures 6.2, 6.7).

2.3.3 Spatial resolution

In this section, the task is to derive the point spread function $PSF(\mathbf{r}, \mathbf{r}_s, f)$, as defined by Equation (2.30), of the passive mapping algorihtm for a single frequency, from which the $psf(\mathbf{r}, \mathbf{r}_s)$ of an arbitrary signal can be derived, as defined in Equation (2.31). To begin with, an exact expression for $PSF(\mathbf{r}, \mathbf{r}_s, f)$ is given, assuming adequate compensation for receiver response effects. Using some simplifying assumptions, a simple expression for the transverse and axial resolutions is obtained for a source near the imaging z-axis. Since the linear array will be placed co-axially with the HIFU transducer, this is a relevant expression that will be verified experimentally in Chapter 4. Many of the derivation steps are taken from closely related work [232; 233].

First, the passive beamformer from Equation (2.23) and the received signal due to a point source from Equation (2.17)

$$\tilde{Q}(\mathbf{r}, f) = \sum_{i=0}^{I-1} A_i \; C(\mathbf{r} - \mathbf{r}_i, f) \; V_i(f) \exp\left(j2\pi f |\mathbf{r} - \mathbf{r}_i|/c\right) \tag{2.46}$$

$$V_i(f) = B(\mathbf{r}_s - \mathbf{r}_i, f) \exp\left(-j2\pi f |\mathbf{r}_s - \mathbf{r}_i|/c\right) Q(f) + N_i(f) \tag{2.47}$$

are combined to express the beamformed signal from a point source, neglecting noise, as

$$\tilde{Q}(\mathbf{r}, f) = \sum_{i=0}^{I-1} A_i B(\mathbf{r}_s - \mathbf{r}_i, f) C(\mathbf{r} - \mathbf{r}_i, f) \; \exp\left\{ \frac{j2\pi f}{c} \left(|\mathbf{r} - \mathbf{r}_i| - |\mathbf{r}_s - \mathbf{r}_i| \right) \right\} Q(f) \tag{2.48}$$

To simplify the above expression, the definition of the wavenumber, $k = 2\pi f/c$,

is used. Furthermore, it is assumed that the compensation term C can adequately cancel the attenuation term B, which is a fair assumption for small $|\mathbf{r}_s - \mathbf{r}|$. The assumption is also made that the linear array is focussed in the $(x, 0, z > 0)$ plane, in which the source also lies. Later experimental results (Section 4.1.2) will address the effect of elevational focussing on out-of-plane sources. Lastly, since the array lies on the x-plane, $\mathbf{r}_i = (x_i, 0, 0)$. These considerations lead to

$$\tilde{Q}(\mathbf{r}, f) = Q(f) \sum_{i=0}^{I-1} A_i \ \exp\{j\phi(\mathbf{r}, i)\} \tag{2.49}$$

$$PSF(\mathbf{r}, \mathbf{r}_s, f) = \left| \sum_{i=0}^{I-1} A_i \ \exp\{j\phi(\mathbf{r}, i)\} \right|^2 \tag{2.50}$$

$$\phi(\mathbf{r}, i) = k\left(\sqrt{(x - x_i)^2 + z^2} - \sqrt{(x_s - x_i)^2 + z_s^2}\right) \tag{2.51}$$

The above is a general expression for $PSF(\mathbf{r}, \mathbf{r}_s, f)$. A simplified expression is now sought for small changes $\delta x = x - x_s$, $\delta z = z - z_s$ in the transverse and axial directions, respectively. Firstly, in order to make the expression integrable, an apodization function $A(l)$ is introduced that is spatially continuous over the array [233], yielding

$$PSF(\mathbf{r}, \mathbf{r}_s, f) = \left| \int_{-\infty}^{\infty} A(l) \exp\{j\phi(\mathbf{r}, i)\} \, \mathrm{d}l \right|^2 \tag{2.52}$$

For an array using uniformly weighted point receivers, the apodization function $A(l)$ is

$$A(l) = \frac{1}{I}\,\Pi(l/D)\,\mathrm{III}\left(\frac{I-1}{D}l + \frac{I-1}{2}\right) \tag{2.53}$$

$$\Pi(l) = \begin{cases} 1 & \text{if } l \leq 1 \\ 0 & \text{otherwise.} \end{cases} \tag{2.54}$$

$$\mathrm{III}(l) = \begin{cases} \delta(l) & \text{if } l \in \mathbb{Z} \\ 0 & \text{otherwise.} \end{cases} \tag{2.55}$$

In the limit of infinite point receivers ($I \to \infty$) forming a continuous receiver surface, the apodization function (2.53) becomes

$$A(l) = \frac{1}{D}\Pi(l/D) \tag{2.56}$$

Next, the second-order binomial expansion of the square root terms in (2.52) is taken – the so-called Fresnel approximation [197; 232; 233]:

$$PSF(\mathbf{r}, \mathbf{r}_s, f) = \left| \int_{-\infty}^{\infty} A(l) \exp\left\{ jk \left(\frac{(x-l)^2}{2z} - \frac{(x_s-l)^2}{2z_s} \right) \right\} \mathrm{d}l \right|^2 \tag{2.57}$$

Transverse resolution

Considering changes $\delta x = x - x_s$ transversely to the array imaging axis, with the correct axial focus $z = z_s$, the point spread function (2.57) becomes

$$PSF(\delta x, f) = \left| \int_{-\infty}^{\infty} A(l) \exp\left\{ -jk \frac{\delta x}{z_s} l \right\} \mathrm{d}l \right|^2 \tag{2.58}$$

Noting that the Fourier transform is defined as

$$\mathcal{F}_\varepsilon\{h(l)\} = \int_{-\infty}^{\infty} h(l) \exp(-j\varepsilon l) dl \tag{2.59}$$

allows Equation (2.58) to be written as

$$PSF(\delta x, f) = |\mathcal{F}_{\varepsilon}\{A(l)\}|^2 \tag{2.60}$$

$$\varepsilon = k\delta x/z_s \tag{2.61}$$

The above result confirms the observation by other researchers that the transverse field of a focused transducer in the focus plane is a scaled version of its far-field directivity pattern, that is, the Fourier transform of its apodization function [234; 233]. Using known properties of the rectangle function $\Pi(l)$ and Shah function $\mathrm{III}(l)$ in the apodization function in Equation (2.53), an analytical expression for the transverse point spread function is obtained:

$$PSF(\delta x, f) = \left| \frac{D^2}{I(I-1)} \mathrm{sinc}\left(\frac{Dk\delta x}{2\pi z_s}\right) *_x \mathrm{III}\left(\frac{DI}{I-1}\frac{k\delta x}{z_s}\right) \right|^2 \tag{2.62}$$

$$\mathrm{sinc}(x) = \sin(\pi x)/(\pi x) \tag{2.63}$$

where the Shah function causes grating lobes due to the finite element spacing $D/(I-1)$. In the current setup, the spacing between two consecutive elements – 0.6 mm (Equation 2.38) – is significant compared to the wavelengths of interest (at $f = 7.5$ MHz and $c = 1480ms^{-1}$, $\lambda = 0.2$ mm). Therefore, the effect of grating lobes will need to be considered (see, for example, Figure 2.5). For the moment, however, the approximation of zero element spacing is taken to enable an estimate of the main lobe.

In the limit of zero element spacing (2.56), grating lobes disappear. Taking this limit, and noting the definitions of the f-number $f_{\#} = z_s/D$ and wave-number

$k = 2\pi/\lambda$ leads to the elegant expression

$$PSF(\delta x, f) = \left|\text{sinc}\left(\frac{\delta x}{f_{\#}\lambda}\right)\right|^2 \tag{2.64}$$

giving a -3dB transverse resolution of

$$\mathcal{P}^x_{-3dB} \approx 0.89 f_{\#}\lambda \tag{2.65}$$

Axial resolution

If the focus is placed correctly in the transverse direction ($x = x_s$), the point spread function parallel to the array imaging axis (2.57) becomes

$$PSF(z, z_s, f) = \left|\int_{-\infty}^{\infty} A(l) \exp\left\{jk\frac{1}{2}\left(\frac{1}{z} - \frac{1}{z_s}\right)(x_s - l)^2\right\} \mathrm{d}l\right|^2 \tag{2.66}$$

In analogy to the Fourier transform that appears in the transverse resolution, the above expression is related to the generalized Fresnel transform [235] and the chirp transform [236]. Assuming small axial deviations $\delta z = z - z_s$, a source close to the imaging axis (a reasonable assumption considering the coaxial placement of the array with the HIFU axis), and a large number of receiver elements with uniform apodization, allows the following approximations

$$1/z - 1/z_s \approx -\delta z/z_s \tag{2.67}$$

$$(x_s - l)^2 \approx l^2 \tag{2.68}$$

$$A(l) \approx 1/D\ \Pi(l/D) \tag{2.69}$$

Substitution of the above approximations into Equation (2.66) gives

$$PSF(\delta z, f) = \left| \frac{2}{D} \int_0^{D/2} \exp\left\{ jk \frac{\delta z}{2 z_s^2} l^2 \right\} \mathrm{d}l \right|^2 \tag{2.70}$$

Using the definition of the Fresnel integral [233], a function that can be accurately computed using series expansions [237]

$$F(z) = \int_0^z exp(j\pi l^2/2) dl \tag{2.71}$$

the following expression is obtained

$$PSF(\delta z, f) = |F(\xi)/\xi|^2 \tag{2.72}$$

$$\xi = \frac{D}{2 z_s} \frac{k \delta z}{\pi} \tag{2.73}$$

which has similarities to the sinc expression obtained for the transverse resolution in Equation (2.64). The definitions of the f-number $f_\# = z_s/D$ and wave-number $k = 2\pi/\lambda$ are again used, as well as a new function that will be called fresnc (in analogy with the definition of the sinc function), to give the axial point spread function as

$$PSF(\delta z, f) = \left| \mathrm{fresnc}\left(\frac{\delta z}{f_\#^2 \lambda} \right) \right|^2 \tag{2.74}$$

$$\mathrm{fresnc}(z) = F\left(\sqrt{z/2}\right) / \sqrt{z/2} \tag{2.75}$$

giving a -3dB axial resolution of

$$\mathcal{P}^z_{-3dB} \approx 6.95 f_\#^2 \lambda \tag{2.76}$$

Predicted experimental resolutions

In the experimental setup, the array has an aperture of 38 mm, with a bandwidth of 5–10 MHz (see Figure 2.1). The array can be placed in two configurations relative to the HIFU transducer. For investigations of cavitation dynamics in the laboratory, the array can be placed transversely to the HIFU transducer, at a distance of 36 mm from the HIFU focus. For clinically relevant passive cavitation mapping, the array is placed coaxially with the HIFU transducer, with a distance of 73 mm from the HIFU focus (doubling $f_{\#}$). These setups are explained in greater detail in Chapter 3. For the latter setup, taking a centre frequency of 7.5 MHz and the speed of sound in water at 20° of 1480 m/s [238] gives resolutions of

$$\mathcal{P}^{x}_{-3dB} \approx 0.4 \text{ mm} \tag{2.77}$$

$$\mathcal{P}^{z}_{-3dB} \approx 4.9 \text{ mm} \tag{2.78}$$

Although using an array with a larger aperture would achieve an even better resolution, the above resolutions are already smaller than the the dimensions of a typical HIFU beam (2 mm transverse width and 15 mm axial length). They also compare favourably with the "gold standard" of ablative HIFU monitoring, MRI thermometry, which has a typical real-time resolution of 3 mm by 3 mm in a plane. The purpose of this section is to use simulations to verify these theoretical resolutions, as well as evaluate the effect of interference between sources.

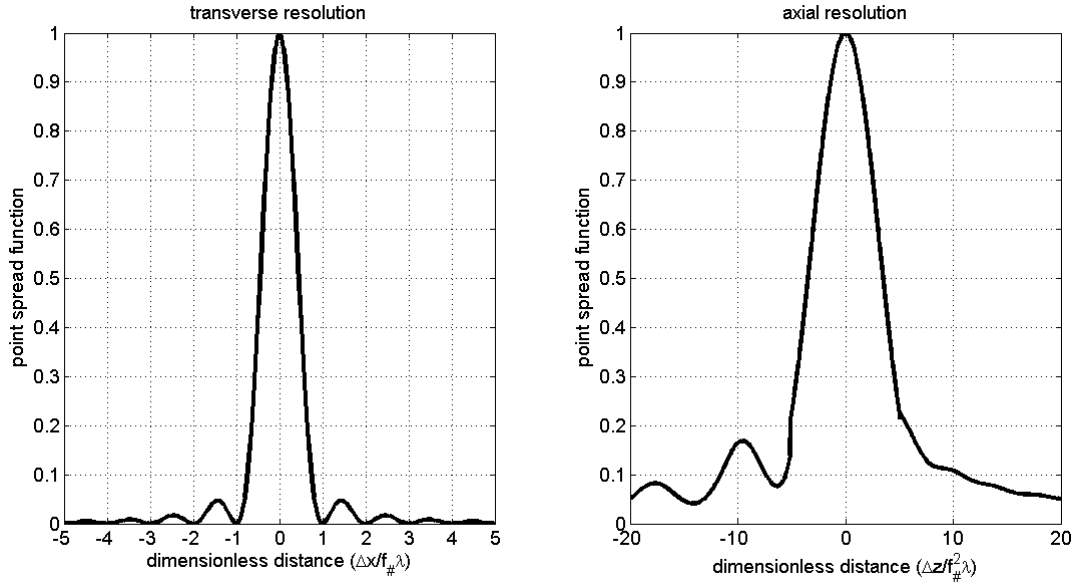

Figure 2.4: Estimated point spread function of passive beamforming with a linear array, using dimensionless distance.

2.3.4 Simulations

Simulation model

To investigate the accuracy of the above resolution estimates, as well as evaluate the performance of the passive beamformer in the imaging plane, some simulations were performed that reflected the experimental setup used in later chapters. The array used has already been described in Section 2.3.2.

Based on Equations (2.14,2.33), the signal received by the array due to point sources of strength $q_k(t)$ is

$$v_i(t) \quad = \quad \frac{b}{4\pi} \sum_{k=1}^{K} d_i(x_k, z_k)^{-1} q_k(t - d_i(x_k, z_k)/c) \tag{2.79}$$

and the corresponding passive source power map $\tilde{\psi}(x, z)$ is calculated using Equations (2.40,2.41) with an integration period T=20 µs.

In the case of single frequency f sources, the above propagation and reconstruction formulae do not suffer from any sampling or integrating errors as the signals are represented in phasor form:

$$V_i = \frac{b}{4\pi} \sum_{k=1}^{K} d_i(x_k, z_k)^{-1} \exp\{-j2\pi f d_i(x_k, z_k)/c\} \; q_k \tag{2.80}$$

$$\tilde{q}(x, z) = \frac{4\pi}{64b} \sum_{i=0}^{63} d_i(x, z) \; \exp\{j2\pi f d_i(x, z)/c\} \; V_i \tag{2.81}$$

$$\tilde{\psi}(x, z) = \frac{1}{4\pi\rho_0 c} |\tilde{q}(x, z)|^2 \tag{2.82}$$

Simulation results

The simulation model derived above is now used to test the performance of the passive mapping system. Of particular interest is the clinically implementable arrangement of the linear array placed coaxially with the HIFU transducer, which will be discussed in greater depth in Section 3.6. For the moment, it is noted that in this monostatic arrangement of the HIFU transducer and linear array, the HIFU focus is at a distance of $z = 73$ mm from the centre of the array. Thus, all simulations to follow will use as their reference point the HIFU focus at $(x_s, z_s) = (0, 73)$ mm.

In the first simulation, a 7.5 MHz source with source power $\psi = 1$ is placed at the HIFU focus. Cross-sections of the obtained image are also taken to be able to compare these with the expressions for the transverse and axial point spread functions (Equations (2.64,2.74)) derived in Section 2.3.3. The results are shown in Figure 2.5. The imager performs as expected, with the estimated point spread functions corresponding well to the actual blurring.

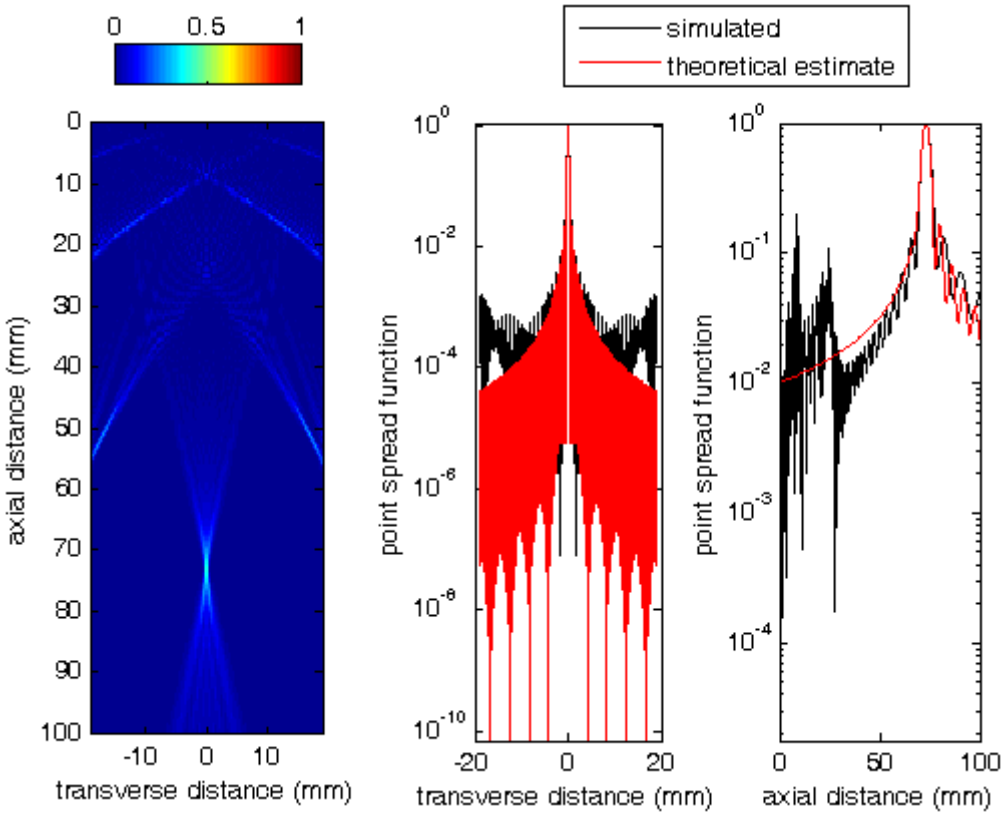

Figure 2.5: Comparison of simulated and theoretical imaging resolution in the clinically-relevant imaging setup. A 7.5 MHz source (corresponding to the centre of the array's 5-10 MHz bandwidth) is placed at the HIFU focus, which is z=73 mm from the centre of the array and on the array's central axis (x=0). The image on the left shows a simulated passive map, while the plots in the centre and right compare the simulated (black) and theoretical (red) point spread functions. Near the focus, the two point spread functions show good correspondence, with transverse and axial resolutions of 0.5 mm and 5 mm respectively. Since the theoretical point spread function was derived with the assumption of small distances from the focus, the function becomes less accurate with increasing distances from the focus. Moreover, the assumption of point receivers in the simulations also becomes invalid for short distances from the array. These two effects lead to a discrepancy between the two point spread functions at distances of less than 30 mm from the array. Finally, note the grating lobes at the edges of the image (outside the region of interest).

A common measure of image resolution is the smallest separation between two sources that enables them to be resolved from each other. Since the axial and transverse resolutions for a 7.5 MHz signal at 73 mm are roughly 5 mm, 0.5 mm respectively, two $\psi = 1$ sources were placed 5 mm, 10 mm and 20 mm apart along the central axis of the array ($x = 0$,$y = 0$), followed by two sources 0.5 mm, 1 mm, 2 mm apart, at a distance of 73 mm from the array. In all cases, the mean location of both sources was at the HIFU focus of $(x_s, z_s) = (0, 73)$ mm. For each of these conditions, the simulated passive maps sought to determine the effect of changing the phase of one of the sources with respect to the other one. In the case of two axially placed sources, a phase lag of 0 was taken to mean that the wavefront of the distal source arrived at the frontal source in phase. The phase lag was varied in the range $[0, \pi]$. In the case of two transversely placed sources, a phase lag of 0 was taken to mean that the two sources were emitting in phase.

The results of the two 7.5 MHz sources placed axially and transversely are shown in Figures 2.6–2.7. The left images show axial and transverse cross-sections as they vary with relative phase, while the right images show the variations of the estimated source powers at the frontal (blue) and distal (green) source locations. As predicted, interference of the two sources occurs due to the coherence between the sources [184]. However, complete destructive or constructive interference does not occur as there is variation in the relative phase difference with which the waves reach the array.

In contrast with the 7.5 MHz sources considered so far, the cavitating sources of interest will be far from sinusoid. In the case of fully chaotic inertial cavitation, cavitation emissions can be modelled as uncorrelated Gaussian white noise.

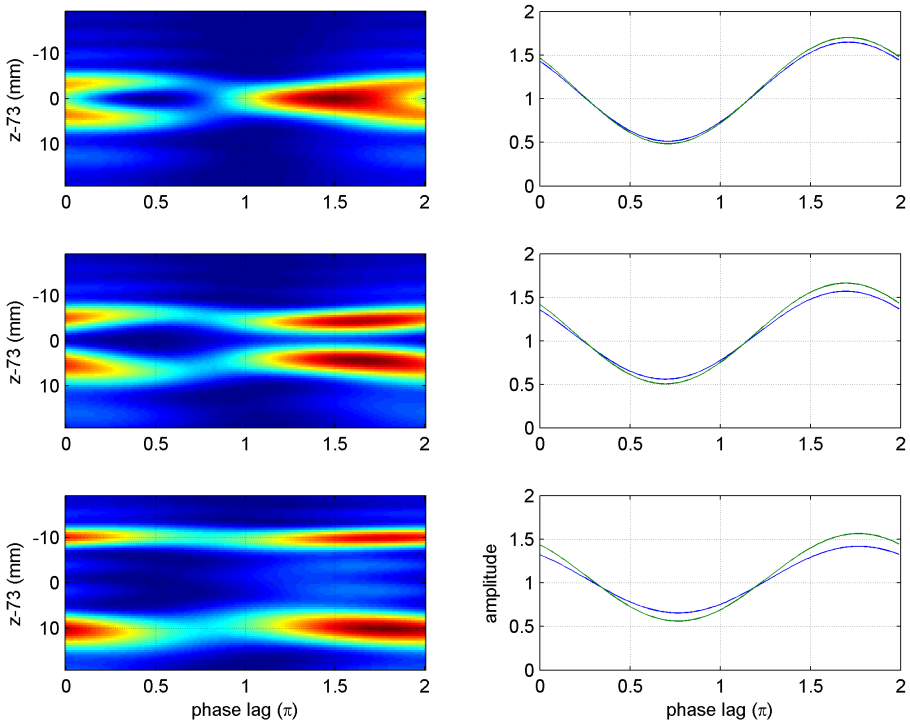

Figure 2.6: Simulation of imaging resolution with two 7.5 MHz sources on the array central axis. The phase lag of the distal source with respect to the frontal source is varied, with a phase lag of 0 corresponding to the distal source wavefront arriving at the frontal source location in phase with the frontal source.

The images on the left show axial cross-sections of passive maps with sources placed 5 mm, 10 mm, and 20 mm apart, with the 5 mm distance corresponding to the resolution limit of the image in the axial direction. The plots on the right show the corresponding variation of source power estimates at the frontal (blue) and distal (green) source locations. The mean location of the two sources was kept constant at the location of the HIFU focus, 73 mm from the array.

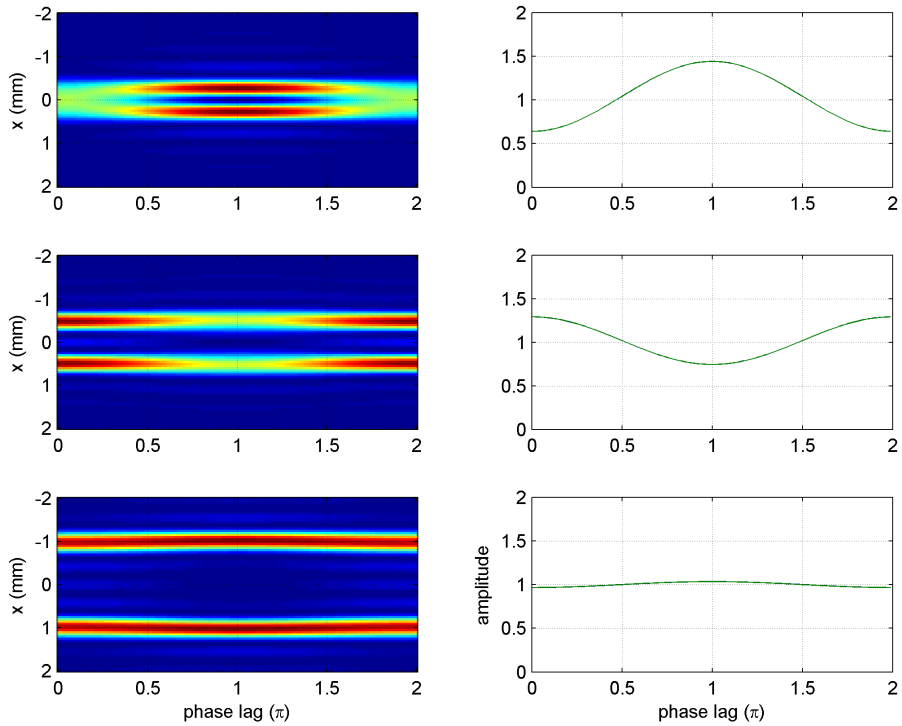

Figure 2.7: Simulation of imaging resolution with two 7.5 MHz sources on either side of the array central axis. The phase lag of the right source with respect to the left source is varied, with a phase lag of 0 corresponding to the two sources emitting in phase.

The images on the left images show axial cross-sections of passive maps with sources placed 0.5 mm, 1 mm, and 2 mm apart, with the 0.5 mm distance corresponding to the resolution limit of the image in the transverse direction. The plots on the right show the corresponding variation of source power estimates at the correct source locations. Blue corresponds to the source at $x < 0$, while green corresponds to the source at $x > 0$. Because of the symmetry of the problem, the two plots are virtually indistinguishable. The mean location of the two sources was kept constant at the location of the HIFU focus, 73 mm from the array.

However, because of the 5-10 MHz bandwidth of the receivers, the array signal will be band-limited. The simulations are therefore repeated for two such band-limited noise sources. Because axial resolution is much worse than transverse resolution, subsequent simulations and discussion will be about the former. Figure 2.8 shows the results for two noise sources placed along the central array (z) axis, with a mean location corresponding to the HIFU focus at z=73 mm. Because of the lack of coherence between the two sources, it can be seen that the source powers estimated are consistently near the correct values of 1.

The above assumption of mutually incoherent sources may be a close approximation at high ultrasound intensities, where both the direct effect of the high intensity and the indirect effect of a large concentration bubbles causes unstable and unpredictable bubble collapse. However, for lower intensities, it has been observed that bubbles can collapse stably. In the next simulation, the recorded emissions from a single bubble has been taken, scaled it to give it unity variance (or source power), and used as the source signal for both sources. The results are shown in Figure 2.9. Because of the self-coherence of the cavitation signal due to periodic collapse, there are perturbations in the power estimates from the true value of 1.

It is seen from the above examples that with increasing coherence between source signals, the source power estimates degrade. Coherence, and thus degradation, is highest for sinusoid signals, and lowest for mutually uncorrelated wideband noise. In the case of correlated single bubble emissions, there are also perturbations in the source power estimates. However, as will be seen in Chapter 4, emissions from different bubbles are rarely well correlated.

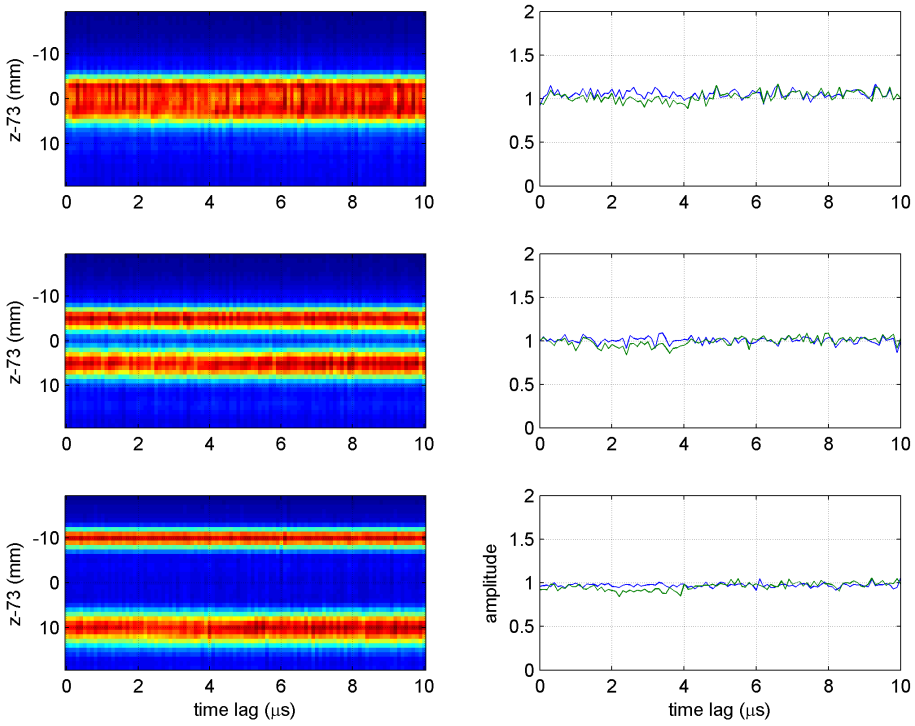

Figure 2.8: Simulation of imaging resolution with two 5-10 MHz noise sources on the array central axis. The time lag of the distal source is varied in the $[0, 10]$ μs range, showing consistent images that vary little.

The images on the left images show axial cross-sections of passive maps with sources placed 5 mm, 10 mm, and 20 mm apart, with the 5 mm distance corresponding to the resolution limit of the image in the axial direction. The plots on the right show the corresponding variation of source power estimates at the frontal (blue) and distal (green) source locations. The mean location of the two sources was kept constant at the location of the HIFU focus, 73 mm from the array.

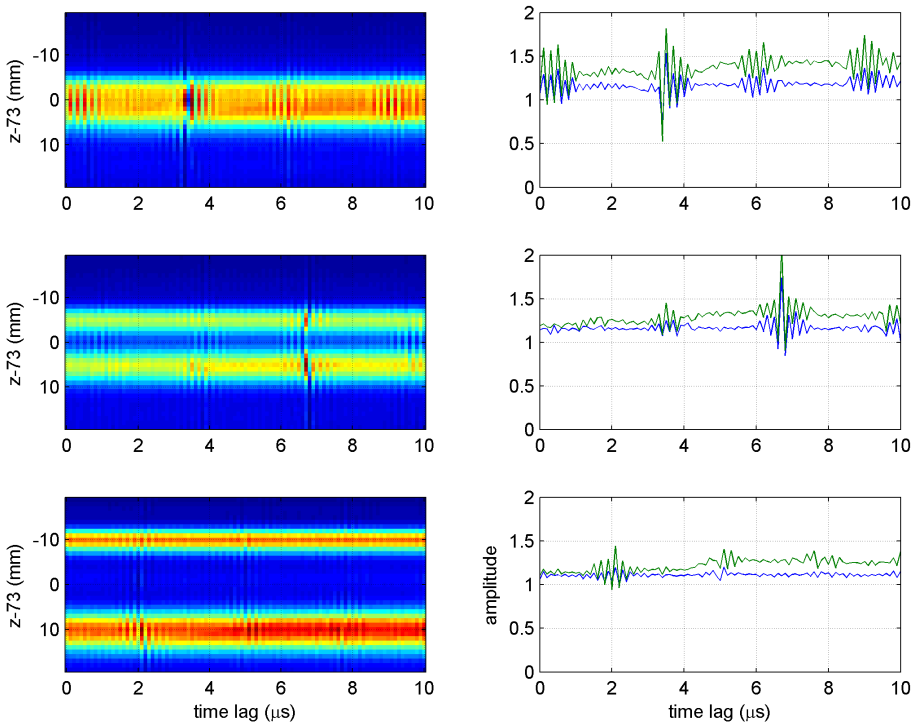

Figure 2.9: Simulation of imaging resolution with stable cavitation emissions used to create two source signals moved apart from the HIFU focus at z=73 mm on the array's central z-axis. The time lag of the distal source with respect to the frontal source is varied, with a time lag of 0 corresponding to the distal source wavefront carrying the same signal when it arrives at the frontal source location as the signal that the frontal source is emitting. Due to periodic bubble osillations

The images on the left images show axial cross-sections of passive maps with sources placed 5 mm, 10 mm, and 20 mm apart, with the 5 mm distance corresponding to the resolution limit of the image in the axial direction. The plots on the right show the corresponding variation of source power estimates at the frontal (blue) and distal (green) source locations.

Of perhaps more concern is the poor axial resolution seen on the images, as predicted in theory. To attempt to improve the resolution, two 5-10 MHz broadband sources were again moved at different distances from each other, with distances of 2.5 mm, 5 mm, 10 mm, and 12.5 mm. A constant $f_{\#}$ of 2.6 (corresponding to maximum imaging depth of 92 mm divided by maximum available aperture of 38 mm) was maintained during source reconstruction by varying the aperture used. Axial cross-sections of the resulting images, along with their deconvolved pairs, are shown in Figure 2.10. The deconvolved images, obtained using regularised deconvolution that assumed a signal to noise ratio (SNR) of 15 dB, clearly show some improvement in resolution, however the source powers are not well estimated. Moreover, the accuracy of these estimates, as well as the quality of deconvolution, greatly depends on the regularizing term of noise power. This is also the case with more complicated and computationally intensive deconvolution algorithms such as Lucy-Richardson. Therefore, while deconvolution is clearly a useful tool in improving the source power field estimates, further work is necessary before it is included in the passive cavitation mapping algorithm, and for now it is omitted.

2.4 Summary

The localization and reconstruction of broadband continuous sources based on pressure recordings outside the source region is not a trivial problem. This chapter has considered the forward problem of the signal received by acoustic receivers due to a source field, and reviewed methods in literature of solving its inverse problem.

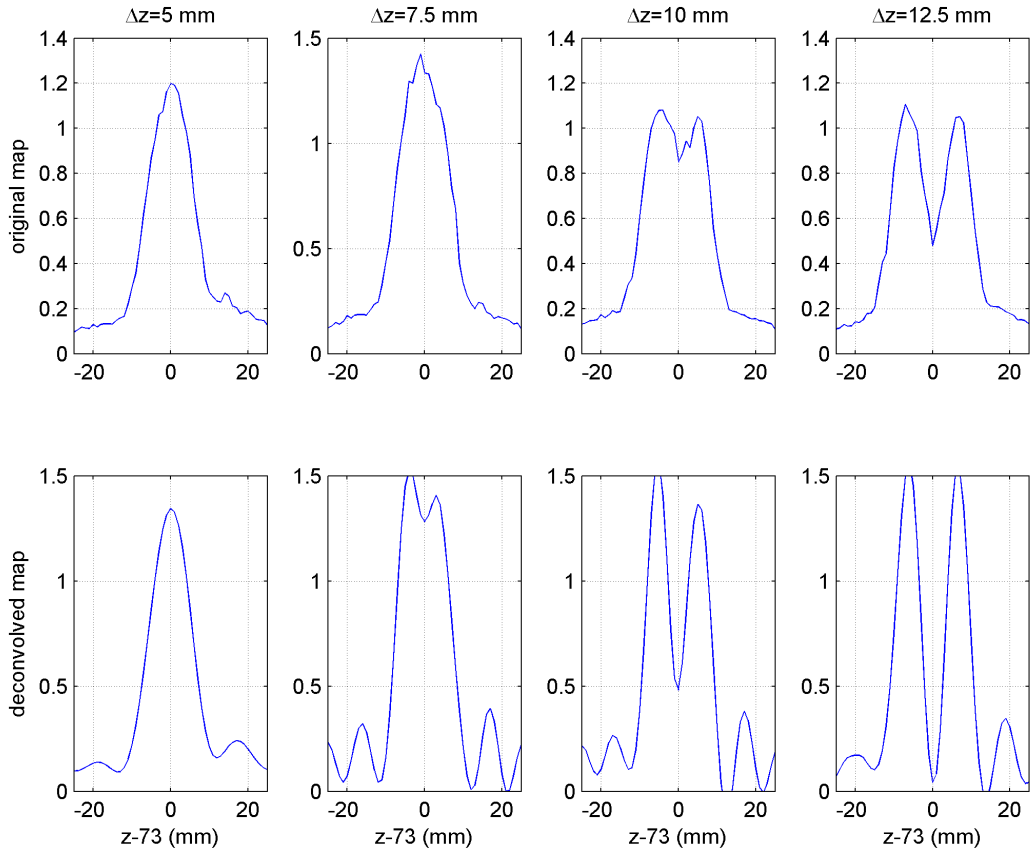

Figure 2.10: Evaluation of deconvolution to improve axial resolution. Two broadband (5-10 MHz) sources with a mean location corresponding to the HIFU focus at z=73 mm were placed at increasing distances from each other along the central array axis. The received array signal was modelled for separation distances of 5 mm, 7.5 mm, 10 mm, and 12.5 mm. In order to ensure a constant point spread function so as to be able to implement deconvolution on the images, a constant $f_{\#}$ of 2.6 was maintained for all depths by varying the imaging aperture with imaged depth (as described in Section 2.2.2). The plots on the first row show the axial cross-section of the original images, while the corresponding plots on the bottom show the deconvolved plots with regularized deconvolution. Other deconvolution methods such as Wiener and Lucy-Richardson yielded similar results.

In the context of mapping the distribution of cavitation emissions using an ultrasound linear array, a modified passive beamforming algorithm was developed that estimated the power of the unattenuated acoustic emissions.

Using some simplified assumptions, the resolution of passive mapping was estimated theoretically. Simulations of passive mapping were then carried out, based on a clinically implementable monostatic arrangement of HIFU transducer and linear array. The performance of passive cavitation mapping was thus numerically evaluated, with good agreement between theory and simulations.

In short, this chapter has provided the theoretical basis and justification for using passive cavitation mapping to monitor cavitation during HIFU exposure.

Chapter 3

Experimental Methods for Passive Cavitation Mapping

3.1 Overview of experimental rationale

In evaluating the applicability of passive cavitation mapping as a method for monitoring HIFU treatment, it is helpful to start with a simplified setup and gradually move towards more complex but clinically applicable configurations. In so doing, difficulties encountered at each stage can be identified and rectified more easily than with all the layers of complexity present. Hence, after considering the generation of passive maps from linear array channel data (Section 3.2) and the rest of the general experimental apparatus (Section 3.3), three sets of experiments, in increasing order of clinical relevance, are described. This sets the scene for Chapters 4–6, where the results of the experiments are presented.

In the first set of experiments, described in Section 3.4, the aim was to create

scattering sources which, unlike cavitation, had precisely controllable locations and temporal signatures. This was achieved by creating ultrasonic waves in water using a broadband transducer and scattering them off a steel wire placed in the transducer focus. Such a setup allowed calibration of the linear array on receive mode, enabling passive maps to be displayed in terms of source power. Furthermore, it was possible to assess imaging resolution for narrowband and broadband sources (the latter acting as a model of cavitation source), and compare this with theoretical and simulated results obtained in Chapter 2. Lastly, the effect of source distributions could be evaluated by capturing array data from several scattering locations and adding the recordings together. The results of these experiments will be left to Chapter 4.

In the second set of experiments, described in Section 3.5, cavitation sources were generated using a HIFU transducer and passively mapped. A bistatic configuration was used whereby the receiver array was placed normal to the HIFU transducer axis, at a short distance from the focal region. The resulting high resolution passive maps enabled an assessment of spatiotemporal cavitation dynamics. The cavitation medium was a homogeneous agar gel, which acted as a simplified model of tissue that caused little distortion of the cavitation emissions. The results of these experiments will be presented in Chapter 5.

During HIFU treatment, the array would need to be placed co-axially with the HIFU transducer, in a monostatic arrangement. The third set of experiments, described in Section 3.6, sought to validate the usefulness and accuracy of passive cavitation mapping in this clinically relevant configuration. Maps of cavitation activity were first generated in the same type of homogeneous, tissue-mimicking agar

gel that was used in the bistatic experiments. This gel was then modified using an innovative two-channel technique to provide prior knowledge of the regions where cavitation activity is likely to occur. Lastly, the correlation between passive cavitation maps obtained during HIFU exposure and ablation of *ex vivo* bovine liver tissue was investigated, providing evidence of the tremendous potential of this technique in a clinical setting. The results of these final experiments are given in Chapter 6.

3.2 Passive mapping from array channel data

The z.one ultrasound system (Zonare, Mountain View, CA) is a highly configurable system that could be used as a conventional B-mode imager or as a tool to passively map a source field. Figure 3.1 shows a photograph of the ultrasound system. A 5-10 MHz linear array (depicted in Figure 2.1) was used to either actively probe the medium in front of the array, or to passively listen to source emissions.

The received data was collected by the scan engine and converted to digital data, either in the form of reconstructed images, or, uniquely among commercial ultrasound systems, pre-beamformed channel data. The data could then be transferred from the engine to a USB stick for offline processing on a computer. A detailed discussion on the functioning of the ultrasound system, and on choosing the optimal acquisition parameters for the generation of passive maps, is found in Appendix A. This includes a discussion of IQ signals, whereby a signal in some frequency band of interest is demodulated to baseband so that it can be sampled at a lower frequency, thus reducing storage costs [239]. For now, the imaging paramaters used for passive

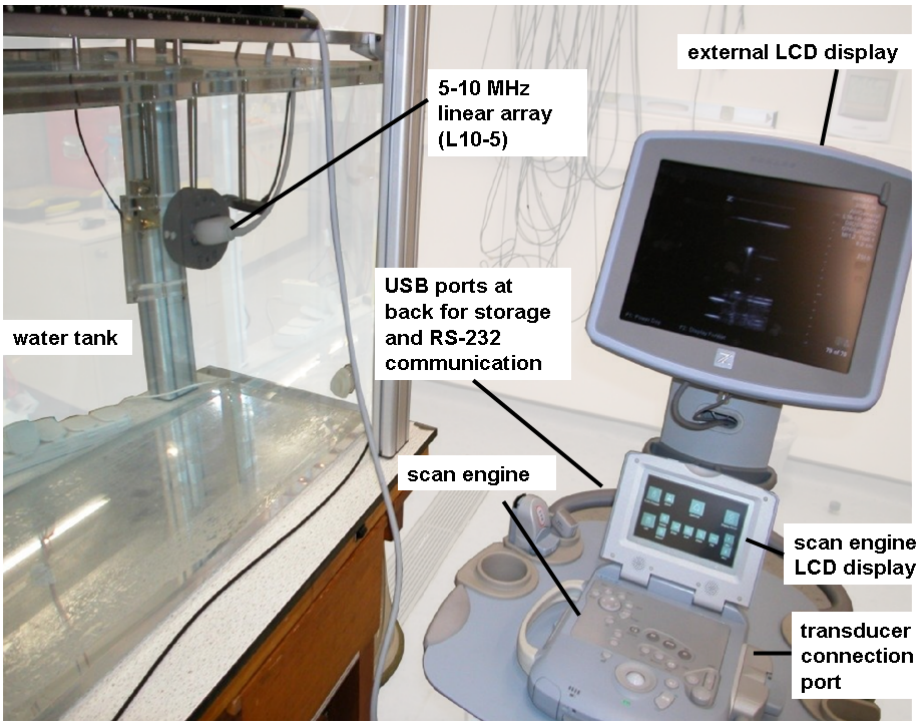

Figure 3.1: The z.one ultrasound engine from Zonare. The 5-10 MHz linear array is connected to the scan engine via the transducer connection port. Conventional B-mode images can be watched and reviewed using the external LCD display. Using two USB ports to the rear of the engine, communication with the scan engine with a serial interface is possible, as well as transfer of data to a USB storage device.

mapping are summarised in Table 3.1.

After reconstruction of 64 channels of RF data from IQ data (Appendix A, [239]), passive source mapping can be applied with an integration interval of $T = 20$ µs(see Equations 2.40,2.41). Given the software-based configurability of the scan engine, the passive maps could, with the assistance of the company's software engineers, be incorporated into the ultrasound system, providing the user with real-time passive maps. Such integration into the ultrasound system has already occured with other research groups, and is envisaged to occur in the context of the present work. In the current work, data is processed offline to generate passive maps.

imaging parameter	setting
pulse transmission	off
receiving aperture	38 mm
TGC	constant (40dB)
recording length	140 µs
frame rate	30-200 Hz
IQ signal band	4.6-9.6 MHz
IQ sampling rate	5 MHz

Table 3.1: Channel data acquisition parameters used for passive map generation. See Appendix A for further details.

3.3 Experimental apparatus

3.3.1 Test tank

All experiments were carried out in a transparent perspex open-top tank filled with water, and fitted with three axis positioning stages for alignment of objects. Water acts as a homogeneous (non-scattering) coupling medium between the acoustic source, the acoustic scatterer (be that a wire or a nonlinear "scatterer" such as a cavitating bubble), and the acoustic detector, and causes negligible attenuation over the frequency range of interest to the present work (1-10 MHz). While cavitation itself is instigated in media that more closely mimick in vivo tissue, water is used to propagate the HIFU wave to that medium, and to propagate any acoustic emissions from the medium to detectors.

To prevent scattering or cavitation in water, it needs to be free from small particles, and have a low gas concentration. Purified water is obtained from tap water passed through a deionising reverse osmosis system (Titan 200, R.O. UltraTec, Fallbrook, CA) that also contains 5 µm and 1 µm filters to remove particulate matter, as well as an activated charcoal filter to remove organic compounds. To maintain purity and lower gas concentration, water is run through a flow loop consisting of the following: centrifuge pump to establish water flow; deionising resin filter; 1µm and 0.2µm filters; and degassing membrane contactor.

The membrane contactor (Liquicel 2.5×8, Membrana, Wuppertal, Germany) has a central channel through which the water flows. The channel is in contact with a rolled membrane whose other side is connected to a vacuum pump set to -0.09 MPa

relative to atmospheric pressure. Therefore, water can flow through the membrane contactor unimpeded while gas forms out of solution at the membrane and escapes through the gas outlet.

If required, water temperature can be maintained at an elevated temperature by also connecting a water heater to the loop. Otherwise, the air-conditioned laboratory keeps the water temperature stable at room temperature (20°C). The temperature of the water is an important parameter to measure as the speed of sound of pure water is well characterized by its temperature [238], increasing from 1482 m/s at 20°C to 1524 m/s at 37°C. (At MHz frequency insonations with µs periods, it is helpful to convert these speeds to mm/µs, with corresponding speeds of 1.482 mm/µs, 1.524 mm/µs). Knowledge of the speed of sound is necessary for two reasons: alignment of objects in the water tank, and the generation of passive source maps.

Alignment of objects in test tank

By measuring the temperature of the water in the water tank, the speed of sound c in water can be obtained [238]. Hence, measurement of pulse-echo times can be used to infer the distance between the interrogating transducer and the reflecting or scattering object. The amplitude of the received echo is also used to ensure the object is at the focus of the transducer. Pulses were generated and the resulting echoes received and amplified using a pulser-receiver (DPR 300, JSR Ultrasonics, Pittsford, NY). An oscilloscope (Wavesurfer 434, LeCroy, Chestnut Ridge, NY) was used to display the amplified signal, and was triggered by the pulser-receiver on each pulse transmission.

As will be seen later when references are made to alignment, the above technique

is extensively used to align objects in the water tank. For instance, a 3.18 mm radius sphere can be used as the reflector to the HIFU transducer. The edge of the sphere facing the transducer will be in the HIFU focus when the return time corresponds to the focal distance of the transducer and the return amplitude is maximised. The ball can then be used to align other transceivers with respect to the HIFU focus.

3.3.2 Source transducers

As mentioned at the beginning of the chapter, the linear array was used to passively map two types of sources. In the first set of experiments, sources were created by scattering a narrowband or broadband pulse off a wire, while in the second and third set of experiments, cavitation was instigated using a HIFU transducer. For the scattering experiments, a signal generator was connected to a broadband transducer. The signal generator could either be a function generator (33250A, Agilent) generating a single-frequency or the pulser-receiver generating broadband pulses. Two types of broadband transducers were used, with their specifications shown in Table 3.2.

For the HIFU-induced cavitation experiments, the HIFU signal originated from the function generator, set to generate a single frequency continuously for a given time period. Typical values of the time period were 2 s, 5 s, and 10 s, set to mimick typical insonation times during HIFU treatment. The signal was then amplified using a power amplifier (A300, ENI, Rochester, NY) before being sent to the HIFU transducer. The amplifier had an output impedance of 50 Ω, and a matching net-

#	centre frequency (MHz)	-6dB fractional bandwidth (%)	aperture (mm)	focal length (mm)	-6dB axial focal width (mm)	-6dB transverse focal width (mm)
1	8	120	22.0	46.0	9.4	0.6
2	15	60	12.7	75.0	75.0	1.6

Table 3.2: Characteristics of broadband transducers used for source generation. Focal widths are calculated using [196] for a 7.5 MHz signal.

frequency (MHz)	aperture (mm)	focal length (mm)	-6dB axial focal width (mm)	-6dB transverse focal width (mm)	-6dB elevation focal width (mm)
1.06	64	63	16	1	2
0.5	64	63	35	4	4

Table 3.3: Characteristics of the HIFU transducers used in the experiments.

work supplied with each HIFU transducer ensured that the combined impedance of the HIFU transducer and matching network assembly was 50 Ω at the operating frequency.

HIFU transducers of two frequencies were used: 1.06 MHz (H-102B SN22, Sonic Concepts, Bothell, WA) and 0.5 MHz (H-107B SN10, Sonic Concepts, Bothell, WA). The former was used in all experiments, apart from the flow channel experiment in Section 3.3.4, when a larger focal volume was required. Both transducers were calibrated using a 75 µm needle hydrophone (SN 1331, Precision Acoustics, Dorset, UK).

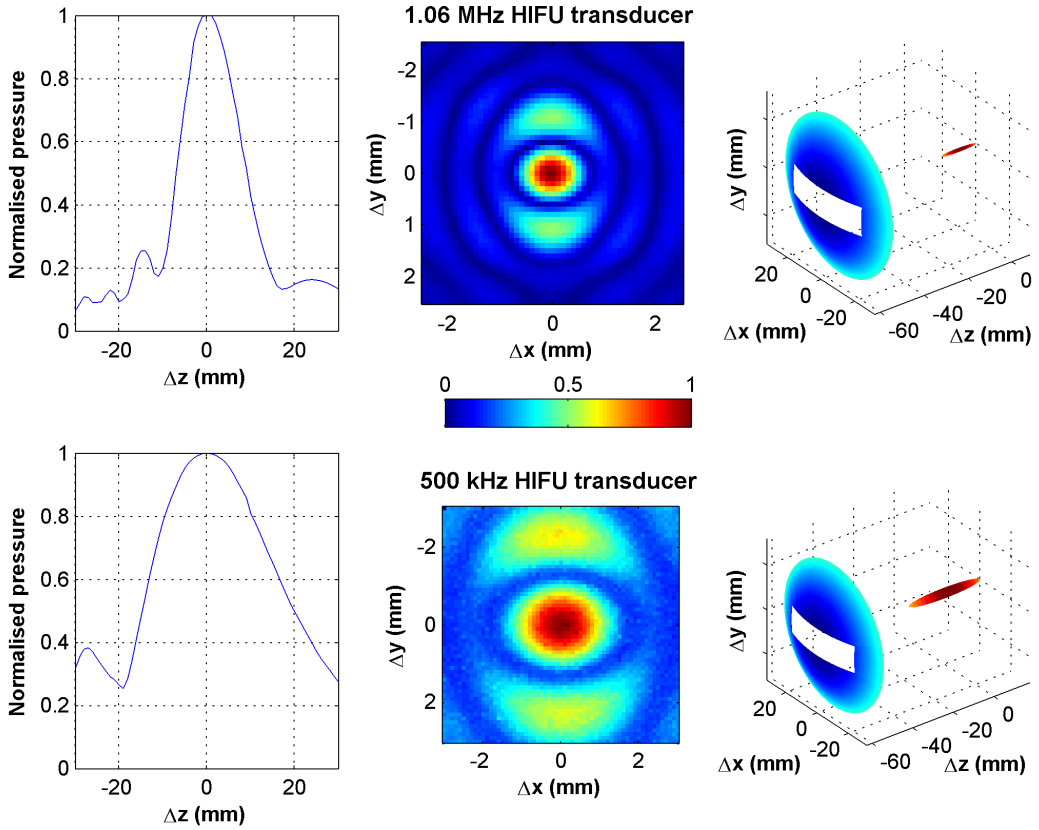

Figure 3.2: Spatial characterization of the field generated by the 1.06 MHz and 0.5 MHz HIFU transducers, obtained using a 75 µm needle hydrophone. The plots on the left show the variation of normalised pressure amplitude on the transducer axis, with deviations Δz away from the focus. The central plots show the normalised pressure amplitudes in the focal plane, while the plots on the right show the size and location of the -6dB beams with respect to the HIFU transducer surfaces. As illustrated in the plots on the right, there are rectangular cut-outs in the HIFU transducers that make it possible to accommodate the linear array. The x and y-axes are chosen so that the elements of the array lie on the x-axis, with Δx, Δy referred to as *transverse* and *elevational* deviations from the HIFU focus.

The hydrophone was used for both absolute calibration (pressure amplitude at focus against amplifier output voltage) and for spatial calibration (characterization of the pressure field generated by the HIFU transducer). The maximum pressure

amplitude recorded by the hydrophone was 1.1 MPa. Up to this pressure, the relationship between the driving voltage and focal pressure was found to be linear ($R^2 > 0.99$), and the peak positive and peak negative (or rarefactional) pressures were essentially identical. However, at higher pressures, the peak rarefactional pressure is expected to decrease (while the peak positive pressure is expected to increase) relative to half the pressure amplitude, due to non-linear propagation of the pressure wave [56]. Therefore, future work will incorporate this effect to provide more accurate estimates of the peak rarefactional pressure, which is the value quoted throughout this text due to its relevance to inertial cavitation (see Section 1.1.4).

Combining absolute calibrations with spatial characterizations of the HIFU field makes it possible to predict the extent of the region over which the pressure amplitude exceeds the cavitation threshold for a given input voltage to the transducer. This enables comparison of predicted regions of cavitation activity with those identifed by passive mapping, as described in greater detail in Section 3.6.

Figure 3.2 shows the results of the spatial calibration. The characteristics of the HIFU transducers provided by the manufacturer, together with the focal widths calculated using the spatial calibration, are shown in Table 3.3.

3.3.3 Active and passive source detection

Two ultrasonic transducers were used for acoustic detection: the 15 MHz focussed broadband transducer that was used for source generation in Section 3.3.2, and the 5-10 MHz 128-element linear array used to generate passive maps.

The broadband transducer could be used either as an active or passive detector.

Connected to the pulser-receiver, it could detect acoustic backscatter from bubbles immediately after HIFU was turned off, thus enabling observation of bubble dissolution. The data was stored in digital form by connecting the receiver output from the pulser receiver to a PCI digitiser card (PCI 5122, National Instruments, Austin, TX).

The transducer was also used as a passive cavitation detector (PCD) to detect cavitation during HIFU exposure. To avoid saturation from the HIFU insonation frequency, the received signal was first filtered using a 5 MHz high-pass filter (Allen Avionics, Mineola, NY) before being amplified using an RF amplifier (SRS 445A, Stanford Research Systems, Sunnyvale, CA). The resulting signal was also recorded using the digitiser.

Whether used for active or passive detection of cavitation, the signal from the broadband transducer was compared with the passive cavitation maps generated by the linear array. The array, shown in Figure 3.3 in a co-axial (monostatic) arrangement with the HIFU transducer, has 128 receivers spanning a 38 mm aperture (see also Figure 2.1). It was designed to be focussed in a plane, with a 5-10 MHz frequency response.

3.3.4 Agar tissue-mimicking gel

The ultimate aim of this work is to test passive cavitation mapping in tissue. However, in addition to the complicated preparation steps detailed in the next section, the structure of tissue shows significant variation from one sample to the next. What

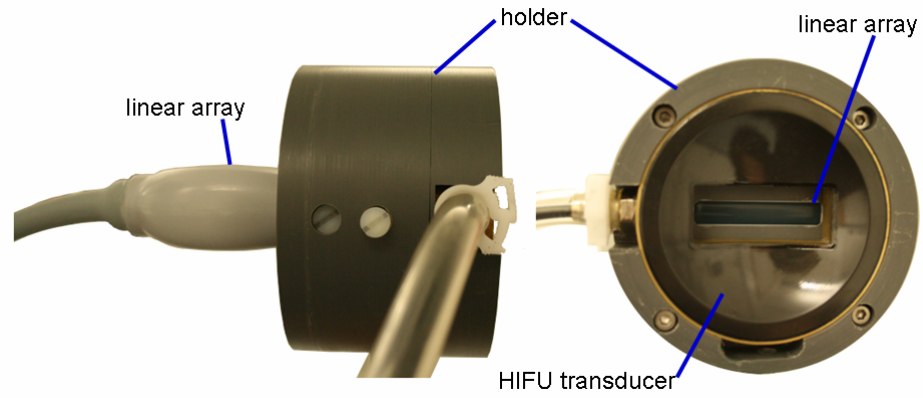

Figure 3.3: The 5-10 MHz linear array within the HIFU transducer in a monostatic arrangement. The spherical HIFU transducer was designed to have a rectangular cut-out in order to provide the linear array with an acoustic window (19 µm thick Mylar). A holder was designed to enable joint mounting and easy alignment of the two transducers. The array is 10 mm behind the surface of the HIFU transducer, reducing crosstalk and thermal damage from the latter.

is first sought is a simple medium that is similar to tissue in its acoustic and cavitating properties, but is simple to prepare and its properties can be made controllable.

At first thought, water presents itself as a simple tissue mimicking material, since a great proportion of tissue is made of up of water. However, unlike water, tissue is a visco-elastic medium, which significantly changes cavitation dynamics [240]. The viscoelasticity of tissue arises mainly from polymers such as elastin in the extracellular matrix that impede fluid flow as well as provide a restoring force to deformations. It would be useful if a similar polymer could be integrated into water to impart viscoelasticity. Moreover, the micro-scale inhomogeneities could provide cavitation nuclei sites that would lower the cavitation threshold from that of pure water. An appropriate candidate for such a polymer has been found to be agar [19].

Preparation of agar gel

Deionized water is heated to 85°C in a beaker with a magnetic stirrer, and 3% agar (3% of the water's mass) is slowly mixed into it. To ensure a repeatable cavitation threshold, the mixture is degassed for 30 minutes at -0.5 bar, and then poured into a perspex holder of inner dimensions 25 mm×25 mm×80 mm (Figure 3.4). The mixture is then left to cool to room temperature, whereupon it becomes a visco-elastic gel, and the sides of the perspex holder can be removed.

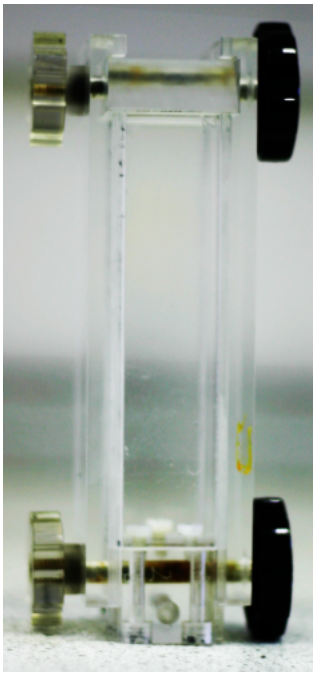

Figure 3.4: Perspex holder for preparing agar-based tissue mimicking gel. The holder ensures a fixed shape for the agar gel while it cools. Upon setting, the sides can be removed, minimising reflections of the HIFU beam during HIFU exposure (Figure 3.13).

By aligning the gel's main axis (the axis intersecting the centre of the 25 mm×25 mm base) with the HIFU focus, repeated HIFU exposures can be done along this axis, with a constant penetration depth of 10 mm along the HIFU axis. Since the elevational beamwidth of the 1.06 MHz HIFU transducer is 2 mm (Table 3.3), a

spacing of 5 mm between consecutive exposures ensures that they are independent of each other.

Properties of agar gel

Agar gel is a simple material to work with: while visco-elasticity makes its cavitation behaviour comparable to tissue, its acoustic properties are very similar to water. This means that there is little distortion of the HIFU beam due to reflection or refraction, and attenuation can also be neglected. Table 3.4 shows the acoustic properties of the agar gel, along with other materials encountered during the HIFU experiments. The speed of sound of agar and liver was measured by measuring propagation time through known lengths, while attenuation was measured by measuring insertion loss of two different sample thicknesses in turn, in order to cancel out reflection losses [56]. The cavitation threshold was measured by measuring the pressure at which broadband noise emissions rose two standard deviations from the noise floor. Much of the tissue characterization was done with other members of the laboratory (see Table 3.4 for acknowledgements).

Agar with two flow channels

One of the difficulties in predicting cavitation in tissue is the unknown cavitation threshold. This situation is further exacerbated if the cavitation threshold changes spatially due to tissue inhomogeneities such as blood vessels. The laboratory had existing experience of modelling blood vessels, which included a holder (designed by B Rifai) to create two interconnected channels 20 mm apart with fluid flow through

Material	Speed of sound (m/s)	Attenuation (Np/m)	Cavitation threshold (peak rarefaction MPa)
pure water (20°C)	1482	0.03, *0.006*	>8
pure water (37°C)	1524	0.02, *0.004*	>8
3% agar (20°C)	1489±19	0.10	1.2, *1.1*
0.5% talc suspension (20°C)	unknown	unknown	*0.2*
ox liver (37°C)	1615	7.38	2.7

Table 3.4: Acoustic properties and cavitation thresholds of different materials used in the HIFU experiments. Attenuation coefficients and cavitation thresholds in *italics* were evaluated at 0.5 MHz, while the rest were evaluated at 1.06 MHz (corresponding to the HIFU frequencies at which the materials were insonified). The speed of sound and attenuation of water were taken from [238; 241]. Agar attenuation was measured by JRT Collin [56] and ox liver properties were measured with R Ritchie and E Mylonopoulou. Water was degassed at -0.9 bar for 5 hours, with < 3 ml/l dissolved oxygen. 3% agar was degassed at -0.5 bar for 30 mins prior to cooling. Ox liver was degassed at -0.9 bar for 30 mins. The speed of sound of talc suspension is assumed to be close to water.

them. In addition, prior work (by JRT Collin and M Arora) had demonstrated that 0.5% talc suspended in water has a relatively low cavitation threshold (Table 3.4), since the hydrophobic talc particles entrap air particles as they are added to water.

Combining the above ideas of flow channels and cavitation enhancement, it was realised that by modifying the holder to create two independent channels, cavitation could be instigated in the channels while leaving the surrounding medium unaffected. Therefore, two disjoint regions of cavitation 20 mm apart could be created, and their cavitation passively mapped.

To prepare the modified agar gel, the molten 3% agar mixture was poured into the holder that had two 1.6 mm stainless steel rods placed in it (Figure 3.5). The rods were placed 20 mm apart, and were removed upon setting of the agar. Two 1.6 mm channels were thus formed, through which either pure water or talc suspension could be made to flow.

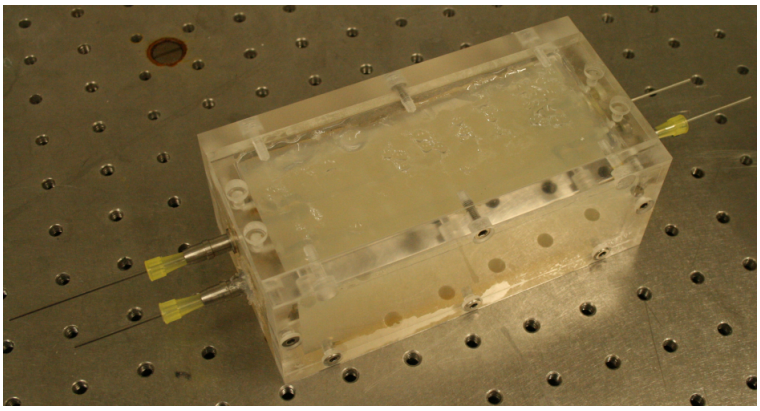

Figure 3.5: Agar gel with two flow channels. The two 1.6 mm rods seen in the picture are removed upon cooling to form two channels 20 mm apart through which cavitation-enhancing talc suspension is made to flow. During HIFU exposure, two disjoint regions of cavitation are thus created, while the surrounding agar gel is left unaffected.

3.3.5 Tissue preparation

In order to create an experiment that reflected, as much as was possible, an actual HIFU treatment, fresh ox liver, used within 4 hours of animal slaugher, was procured from a local abattoir. Its properties are shown in Table 3.4. Working with tissue is a complex task requiring patience and accuracy, and the author was fortunate to do these experiments with assistance from a skilled medical doctor and researcher, R Ritchie.

During the process of cutting and storage, air invariably enters the tissue, raising its gas concentration. Unfortunately, there were no reliable means of monitoring gas concentration during tissue preparation. Instead, to achieve some measure of repeatibility and closeness to living tissue, the tissue was degassed in phosphate-buffered saline solution at -0.9 bar for 30 mins (Figure 3.6). The saline solution was used to keep the tissue in an isotonic environment to minimise cell damage.

The setting of -0.9 bar, 30 mins, though seemingly arbitrary, provided a way to compare results with other work using *ex vivo* ox liver [179], where the conditions of the tissue preparation and HIFU insonation were very similar (although in that experiment, a temperature of 22°C was used, and a lower degassing pressure of -0.97 bar had been was achieved). Curiously, in that work, a cavitation threshold of 2.9 MPa was measured without degassing, and a threshold of 5.8 MPa was measured with 30 mins degassing; in this work, 2.7 MPa was measured with degassing. For comparison, a cavitation threshold of 2.7 MPa was measured for an *in vivo* study of dog muscle [242].

Upon degassing, the liver was transferred into a 90 mm×90 mm×40 mm holder (Figure 3.7). The 90 mm×90 mm sides were covered with 19-µm-thick Mylar to provide an acoustic window through which the HIFU beam could pass, so that the HIFU focus was placed 20 mm inside the tissue. Due to the hydrophobic nature of Mylar, the holder was also degassed along with the tissue and the liver was placed inside the holder while surrounded by the saline to ensure air would not enter the inside of the holder.

Figure 3.6: Degassing setup for ox liver. A desiccating chamber is used to set up an enclosed environment in which a partial vacuum of -0.9 bar can be created using a vacuum pump. Once the pressure is attained, the valve at the right can be switched off. Pressure can be monitored using the meter next to the valve. To ensure no air enters the inside of the tissue holder, both tissue and holder are degassed under phosphate buffered saline solution for 30 mins before being assembled in the solution.

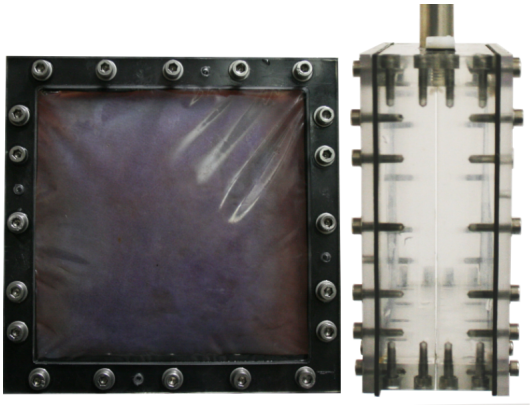

Figure 3.7: The liver holder. The holder has a 90 mm×90 mm acoustic window through which the HIFU beam is focussed, as shown on the left with a section of liver inside. Leaving a distance of 20 mm from the edges of the acoustic window and 10 mm between exposures, 6×6 exposures can be effected. As shown on the right with the liver removed, a 40 mm thickness of liver is used, with a central slit at the midplane that is covered with insulating tape during HIFU exposures and cut through with a microtome at the end of the exposures. The HIFU beam is focussed at this midplane, with a penetration depth of 20 mm.

3.3.6 Thermometry

As described in Chapter 1, cavitation has been found to greatly increase the rate of heating during HIFU exposure. It is therefore of interest to see if the estimated source power obtained using passive mapping can be related to temperature increases. This reflects previous findings that when heating is dominated by inertial cavitation, the broadband signal power received using a single-element passive cavitation detector is proportional to the heating rate in its focal region [56; 20; 21].

By using a thermocouple connected to a data acquisition unit (34970A, Hewlett Packard, Palo Alto, CA), temperatures at a single point can be recorded at a rate of 10 Hz. To minimise the effect of the thermocouple in the HIFU field as well as to avoid thermocouple artefacts, a T-type thermocouple embedded in a 200µm stainless steel needle (HYP0, Omega, Stamford, CT) was chosen. This thermocouple could be easily inserted into the cavitation medium.

To have meaningful temperature recordings, it is important to have control over the location of the thermocouple with respect to the HIFU focus. For this, the thermocouple must first be placed at the HIFU focus. This can be done on a rough spatial scale by connecting the HIFU transducer to the pulser-receiver and aligning the tip of the needle (which is close to the thermocouple element) with the focus. A more precise positioning is then achieved by finding the spot where the maximum temperature rise is observed following a low amplitude insonation. Since a peak rarefactional focal pressure of only 0.6 MPa is used, the temperature rise is very small ($< 1°C$) and no cavitation is generated, thereby ensuring that the effect of insonations is only temporary.

3.4 Passive mapping of time-invariant scatterers

As explained in Section 3.1, it was thought instructive to create a simple scattering source that could be used to calibrate the array on receive as well as generate passive maps of a source of known location and temporal signature. Using an acoustically small spherical scatterer would have required embedding this scatterer into a homogeneous gel, without contaminating the gel with further scattering particles [56]. Such a small scatterer would be difficult to locate and would have a weak scattering amplitude.

To counteract the above difficulties, it was decided that a broadband transducer should insonate a small section of a wire scatterer that cut the (x-z) plane of the linear array in the y (elevation) direction, as depicted in Figure 3.8.

Two pairs of insonator/scatterer were used, reflecting the changing needs of the experiments. First, a 15 MHz broadband transducer with a -6dB beam width of 1.6 mm (Table 3.2) was used with a 0.5 mm stainless steel wire to provide a strong scattering signal for absolute calibration. Both the array and the 0.5 mm needle hydrophone (SN1203, Precision Acoustics, Dorset, UK) were placed 40 mm from the section of the wire in the array plane (Figure 3.9), and insonated in the 4-11 MHz frequency range. Although the diameter of the scatterer is large compared to the wavelengths of insonation (0.13-0.36 mm), the effects of non-uniform scattering directivity were minimised by the axisymmetric placement of the centre of the array and the hydrophone. The 5 mm elevational aperture of the receivers is estimated to cause a 10% diffraction error, which is also the calibration uncertainty of the

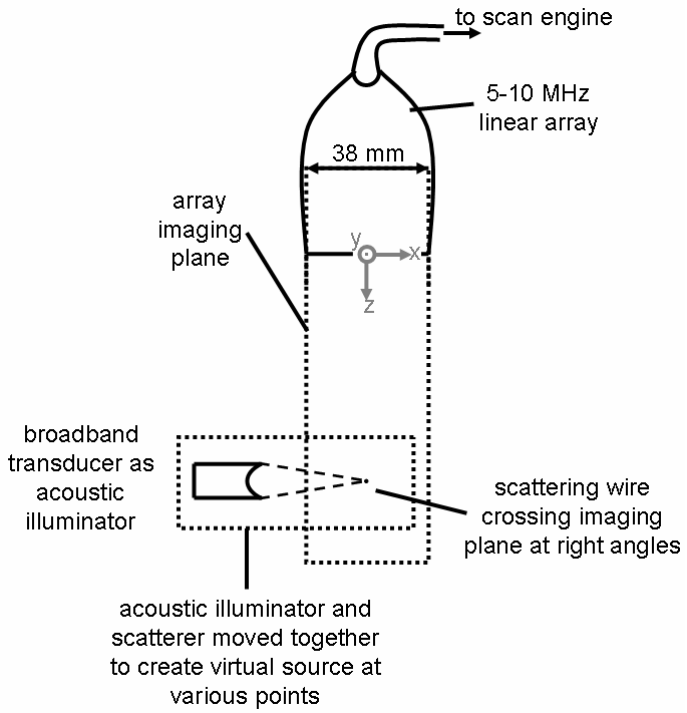

Figure 3.8: Passive mapping of an insonated scattering wire.

hydrophone.

The above insonator/scatterer arrangement was also moved in the shape of a 10 mm by 10 mm cross centred at the HIFU focus. Two source signatures were used: broadband pulses produced by the pulser-receiver, and a 7.5 MHz sinusoid generated by the function generator. The array recordings from several locations could then be added to look at the resolution of passive mapping, and compare it with simulated passive maps (see Section 2.3.4).

Seeking to provide accurate spatial calibration of the array, and no longer constrained by the low SNR of the hydrophone, a new insonator/scatterer arrangement was used: a 8 MHz broadband transducer, with a -6dB beamwidth of 0.6 mm (see Table 3.2) was set to insonate a 0.02 mm tungsten wire. To provide the calibration, the wire was moved continuously from $z = 20mm$ to $z = 120$ mm from the array

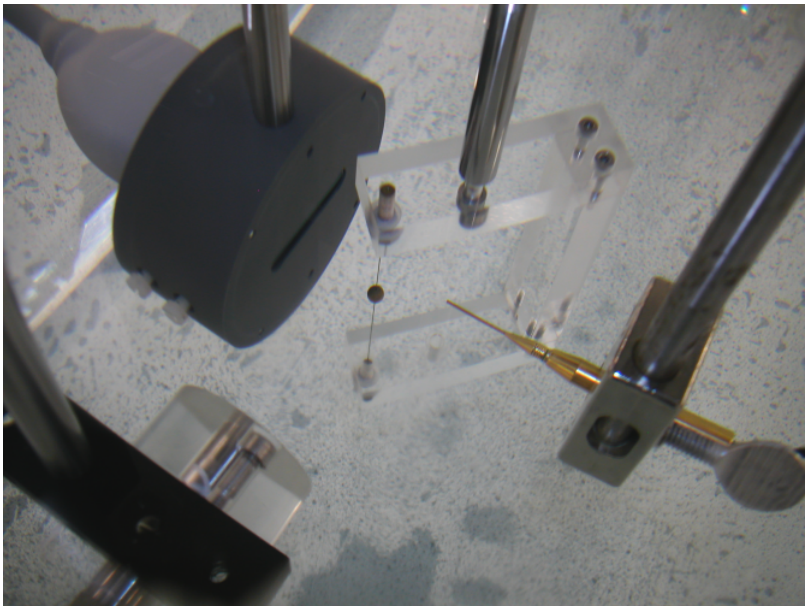

Figure 3.9: Absolute calibration of linear array on receive. The pressure wave generated by a 15 MHz broadband transducer (bottom left) is scattered by a 0.5 mm wire (the bronze sphere is outside the transducer beam) and received by the linear array and a calibrated 0.5 mm needle hydrophone. The centre of the array and the hydrophone are equidistant (40 mm) from the scattering section of the wire and axisymmetric along the transducer axis, allowing calibration of the pressure sensitivity of the array elements with frequency.

in less than 4 s. The array was recording for 5 s, capturing the scattering source from different distances at a frame rate of 75 Hz. Since there was no synchronisation between the pulser receiver and the scan engine, the frames only captured two out of every three pulses. However, such an arrangement still yielded an average source spacing of 0.5 mm between subsequent acquisitions. Assuming equal sensitivity of array elements, calibration data for a planar section was thus captured with high speed and spatial accuracy. Recordings were made for elevations of $y = -5, -4.5, \ldots, 5$ mm.

To extract the spatial response of the receivers from the calibration data, the directivity of the scatterer needs to be decoupled from the directivty of the receivers.

For the distances quoted above, the resulting finite length cylinder was well approximated by an acoustically small (much smaller than the wavelength of insonation) spherical scatterer insonified by a plane wave [243].

Despite their simplicity, even acoustically small spherical scatterers do not scatter sound isotropically. Objects scatter sound due to the contrast in *compressibility* K_s and *density* ρ_s with those of the surrounding medium, denoted by K_0 and ρ_0. For a small spherical object insonified by a plane wave, the scattered pressure in the far-field is proportional to [192]:

$$\frac{K_s - K_0}{K_0} + \frac{3(\rho_s - \rho_0)}{\rho_0 + 2\rho_s} \cos\theta \tag{3.1}$$

where θ is the angle with respect to the direction of propagation of the plane wave. Thus, changes in compressibility cause uniform, or monopolar scattering, while changes in density cause so-called dipolar scattering. Substituting values of $(K_0, K_s) = (488, 6)$ TPa^{-1}, $(\rho_0, \rho_s) = (998, 7800)$ kg m^{-3} [241] into the above expression leads to the directivity pattern shown in Figure 3.10.

To negate the effects of the dipolar term, the mean of the spatial calibration map and its mirror image around the $x = 0$ (or $\theta = \pi$) plane could be taken. In any case, calibration values at $x = 0$ are not affected by the dipolar scattering term, allowing calibration of the array receive response with distance.

In addition to spatial calibration, movement of the wire in the direction of the array axis also provided a good opportunity to simulate semi-continuous source fields by adding together array recordings corresponding to different source positions. These synthesised recordings could then be used to assess the accuracy of passive

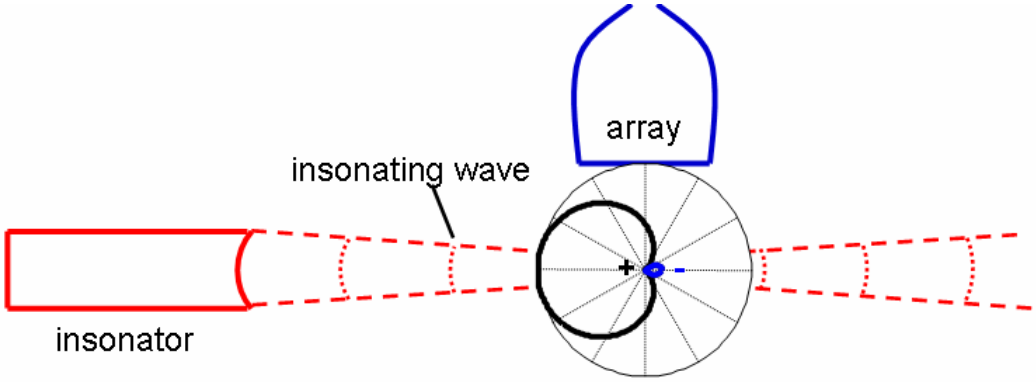

Figure 3.10: Scattering of sound by an acoustically small tungsten wire in water. The polar plot shows the amplitude of the pressure scattered in different directions (directivity pattern) if the scattered volume can be approximated as an acoustically small sphere. The combination of compressibility and density contrast causes a seemingly complex directivity pattern. However, normal to the propagation of the insonifying wave, only the uniform (monopolar) scattering term features. This allows calibration of the array sensitivity with distance.

maps applied to source distributions.

Passive source localizaton during calibration

The locations of the sources were estimated by fitting the arrival profiles of the scattered wave to a parabola and extracting its coefficients, as described in Section 2.3.2. For a single source, this algorithm is faster than generating a passive map and finding its maximum, and is independent of the spatial sensitivity of the array.

3.5 Bistatic passive cavitation mapping

The previous section stated the importance of abstracting the problem of cavitation mapping during HIFU treatment. Having generated model sources in the previous section, it would be useful to investigate the spatiotemporal dynamics of cavitation in a simple tissue-mimicking material.

As has been noted in Chapter 1, several researchers have noticed that the hyperecho-based method of identifying cavitation lacks sensitivity [136; 137]. It is postulated that this is because once HIFU is turned off (a necessary part of hyperecho imaging to avoid HIFU interference), cavitation stops occuring and the bubbles will dissolve away. In this experimental setup, the aim was also to verify this hypothesis.

To achieve the above aims of accurate spatiotemporal reconstruction of cavitation activity and its comparison with hyperecho-based cavitation localisation, an agar-based tissue mimicking gel was placed in the 1.06 MHz HIFU transducer focus, with the 15 MHz broadband transducer co-axially aligned with the HIFU transducer and actively (pulse-echo) interrogating the agar gel. At the same time, the linear array was placed 36 mm from the HIFU focus in a transverse configuration, as shown in Figure 3.11. This arrangement is called bistatic because the source and receiver are at different locations [244].

Given the good transverse resolution of the linear array, the experimental setup allows observation of cavitation distribution along the HIFU axis. In this sense, this setup and its results have similarities to the work of Farny [78]. However, the innovation of the present work is the use of passive beamforming on channel data,

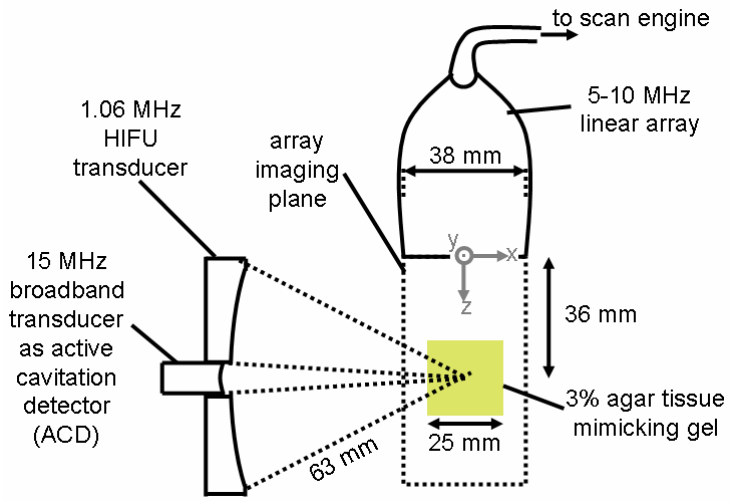

Figure 3.11: High-resolution passive cavitation source reconstruction and mapping. The ratio of focal distance to aperture being less than unity for the linear array, high resolution passive source maps are attainable, and the source signature of individual bubbles can also be reconstructed. The latter provides an attractive alternative to high-speed photography of cavitation bubbles when investigating cavitation dynamics.

as well as the use of a low ratio of focal distance to aperture ($f\# = 36/38 \approx 0.95$).

The above two changes offer two significant improvements. Firstly, 2-D cavitation maps can be generated. Secondly, the entire 2-D source field can be reconstructed as it varies with time, yielding time-dependent source strength estimates of individual bubbles. This new development offers a cheap alternative to high-speed photography (HSP), which at any rate is unable to image bubbles in opaque media. It must be noted, however, that the shape changes captured by HSP provide more information than that provided by source strength, even if it is possible to infer radius-time profiles from the latter [56].

In localising bubbles from their emissions with high spatial resolution, it is instructive to see whether the bubbles can be localised with pulse-echo methods, as in the hyperecho-based identification of cavitation. Unfortunately, it is difficult to

switch quickly from passive mapping to B-mode imaging with the current system. Therefore, the 15 MHz broadband transducer was placed coaxially with the HIFU transducer and connected to the pulser-receiver. The pulser-receiver was set to send a pulse every 500 µs, and the receive output of the pulser-receiver was connected to the digitiser card, which was set to receive continuously at 50 MHz sampling for 3s. During this time, the HIFU signal was off-on-off for 0.5s-2s-0.5s. This timing ensured that the broadband transducer could detect cavitating bubbles, free of HIFU interference, within 500 µs of the HIFU signal being switched off, for a further 0.5 s. Thus, the significance of bubble dissolution in actively detecting cavitation bubbles could be assessed.

To help consider the effect of bubble dissolution, it is noted that the typical frame rate of an ultrasound imager is 10 Hz. This means that bubbles that dissolve away (or dissolve to a size undetectable by the imager) within 100 ms, a time that will be called the *detection delay*, may not be seen.

Schemes have been devised whereby imaging is synchronised with the HIFU beam being switched off [135], which could shorten the detection delay, and therefore increase sensitivity. However, even then, to be able to image a large enough region of interest, the detection delay will be of the order of microseconds [138] (this is supposing the bubble had been cavitating up to the last HIFU excitation cycle). In short, the 500 µs detection delay provides a much-improved scheme for active cavitation detection that is expected to surpass the sensitivity of B-mode imagers. Section 5.3 will reveal whether even this scheme sometimes fails to detect previously cavitating bubbles.

3.6 Monostatic passive cavitation mapping

In the previous section an experimental setup was shown where it was possible to generate high-resolution passive maps of cavitation. Unfortunately, in the clinic, no more than a single axis can be readily found to propagate acoustic energy from an ultrasound transducer to the intended target, especially in the presence of challenging intervening structures such as the ribcage. Placing a detector at an angle to the HIFU axis is therefore not an option, nor is it possible to have the linear array so close to the HIFU focus. Instead, to have minimal interference with the HIFU treatment, and to be able to quickly register the area of HIFU treatment with passive maps and B-mode images, it is best to have the linear array co-axially aligned with the HIFU transducer, in a so-called monostatic arrangement. For this, the HIFU transducer needed to have a rectangular cut-out in the centre and a holder was designed to keep the HIFU transducer and linear array together (Figure 3.3).

The resulting co-axial configuration of HIFU transducer and linear array is one that is easily transferrable to the clinic. Therefore, the resolution and quality of passive maps obtained with this configuration informs the quality of passive maps that may be obtained during treatment.

As depicted in Figure 3.12, the configuration was tested with three different media: homogeneous agar, agar with two flow channels, and ox liver. The preparation of these media have already been described in Sections 3.3.4 and 3.3.5. A brief description of the three experiments follows.

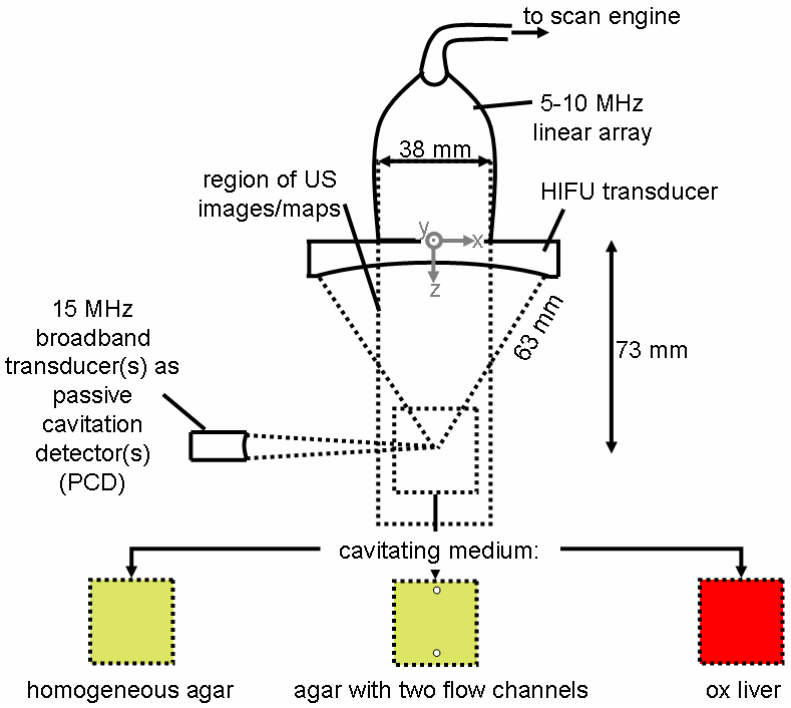

Figure 3.12: Schematic of passive cavitation mapping experiments with the linear array in the HIFU holder. Three different cavitation media are used. The homogeneous agar is expected to produce cavitating bubbles within a continuous region, corresponding to the portion of the HIFU beam above the cavitation threshold (Figure 3.14). The modified agar gel with two flow channels creates two disjoint regions of cavitation 20 mm apart due to the lowered cavitation thresholds of the talc suspension flowing through the channels compared with the surrounding agar (Figure 3.15). Lastly, ox liver is used as a more realistic representation of tissue during HIFU treatment.

3.6.1 Cavitation mapping in agar gel

When homogeneous agar gel was used as the cavitation medium in the experiment, two 15 MHz broadband transducers acting as passive cavitation detectors (PCDs) were placed transversely to the HIFU axis, with their foci aligned on the HIFU axis, one at the HIFU focus, and the other 5 mm pre-focally (Figure 3.13). With a -6dB beamwidth of 1.6 mm, these PCDs could be used to validate the passive cavitation maps. In addition, the calibration of the HIFU field, together with the measured

cavitation threshold, allowed a prediction of the initial cavitation distribution when the HIFU is switched on, as depicted for three different focal pressures in Figure 3.14.

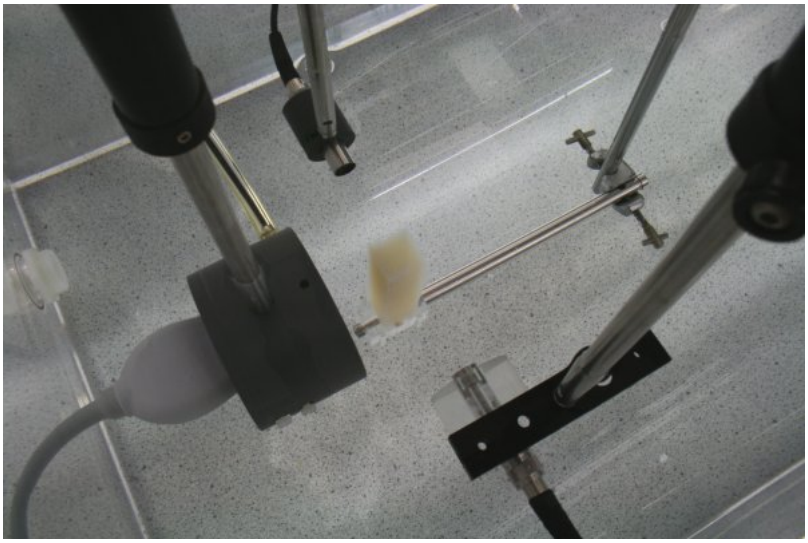

Figure 3.13: Passive cavitation mapping setup with homogeneous agar. The linear array and HIFU transducer are held together using a custom-designed holder in the lower left. Two 15 MHz broadband transducers, used as passive cavitation detectors (PCDs), are aligned confocally with the HIFU axis (one focally, the other prefocally by 5 mm). The centre of the agar tissue-mimicking gel is aligned with the HIFU focus. Following each HIFU exposure, the agar is moved 5 mm upwards, thereby allowing use of unexposed sections of agar, while the HIFU focus is maintained at an equal penetration depth of 10 mm.

In the case of agar embedded with two flow channels, whose preparation is described in Section 3.3.4, the flow channels could be made to cavitate selectively by flowing either pure water or 0.5% talc suspensions through the channel.

To create these two disjoint regions of cavitation, the pressure field would need to be such that the cavitation threshold was only exceeded at the channels (Figure 3.15). A broad HIFU beam was therefore necessary to ensure that both channels

Figure 3.14: Expected cavitation regions in homogeneous agar. The solid lines depict the axial pressure distribution created by the 1.06 MHz HIFU transducer for three different peak rarefactional focal pressures. Before cavitation dynamics has had a chance to change the cavitation distribution, cavitation is expected to occur in the regions above the dashed line (the measured cavitation threshold). Figure reproduced from [183].

received enough pressure. This is the only experiment where the 0.5 MHz HIFU transducer, with its wider beam (see Figure 3.2), was chosen.

The solutions were poured into 100 ml syringes connected to the channels using plastic tubing (Figure 3.16), with the channel outlets collected via beakers. (Based on a time of around 10 s for 100 ml of solution to pour through a 1.6 mm channel, the volumetric flow rate was roughly 10 ml/s.) This arrangement meant that if talc suspension was made to flow through the channels, the channels kept being replenished with new cavitation nuclei during the HIFU exposure.

THIS IMAGE HAS BEEN REMOVED
DUE TO COPYRIGHT ISSUES.

SEE ARTICLE FOR ORIGINAL FIGURES

Figure 3.15: Expected cavitation region in agar gel with two flow channels. The solid line depicts the axial pressure distribution created by the 0.5 MHz HIFU transducer during the experiment, as predicted by calibrations. The dashed line shows the variation of cavitation threshold. As the cavitation threshold is lower in the talc suspension than in the agar, a judicious choice of peak rarefactional pressure ensures that the cavitation threshold exceeded at the channels only. Figure reproduced from [183].

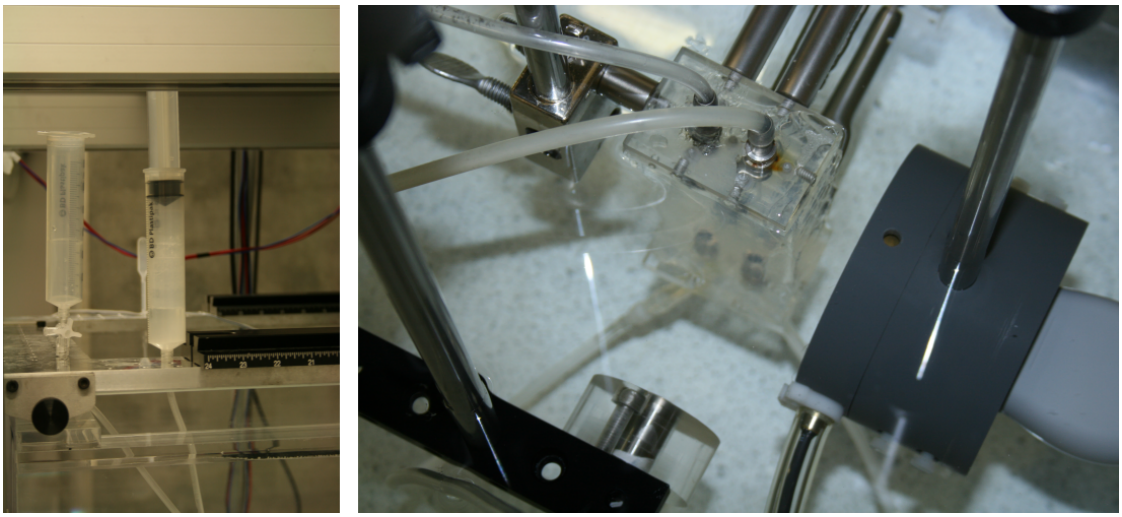

Figure 3.16: Passive cavitation mapping setup with cavitation-enhanced flow channels. Talc suspension is made to flow through the two channels using 100 ml syringes, with the outflow collected using beakers. During HIFU exposure, the flow of talc suspension provides a fresh source of cavitation nuclei in the two channels along the HIFU axis.

3.6.2 Cavitation mapping during tissue ablation

For cavitation mapping to be useful in ablative HIFU therapy, Cavitation maps do not just need to be accurate, but they must identify where cell death has occured. Therefore, fresh bovine liver was prepared following the manner described in Section 3.3.5, and was ablated using HIFU exposures. The passive cavitation maps were then compared with a macroscopic marker of tissue death, namely blanching.

Up to now, all experiments were conducted with a water tank at room temperature (20°C). With liver, however, the water tank temperature was maintained at a systemic temperature of 37°C (although the average body temperature of oxen is in fact slightly higher, at 38.6°C [245]).

In conducting the experiments, it was deemed essential that the HIFU beam did not reflect off the perspex holder, and that HIFU exposures were far enough apart as to be not influenced by each other. For this reason, exposures were placed 10 mm apart and at a minimum distance of 20 mm from the edges of the 90 mm×90 mm acoustic window. This resulted in 6×6 possible exposures in each liver.

After HIFU exposures, the liver needed to be cut to reveal the extent of macroscopic thermal damage (blanching [246]) along the HIFU axis. Cutting accurately through the HIFU axis is difficult, however. For this reason, a prior mid-plane cut through the liver was necessary to reveal the lesions at the focus before cutting in the axial directions. In order to minimise deformation of the liver, the mid-plane cut was made while it was still in the holder. Hence, the holder was designed with a slit in its mid-plane (Figure 3.7) that could receive a microtome blade. To seal the isotonic solution from the deionized water in the tank, as well as keep the water

tank clean, this slit was covered with insulating tape during the HIFU exposures, which was then cut through with the microtome following the HIFU exposures.

Following the midplane cut, cuts along the direction of the HIFU axis were made. The two halves could then be joined together to reveal the extent of the lesions along the HIFU axis.

3.7 Summary

This chapter has described how passive maps were generated using channel data from an array, as well as other apparatus used in the experiments. Three sets of experiments were carried out, with increasing complexity and relevance to the monitoring of HIFU treatment. First, wire scatterers were used to calibrate the array on receive and generate sources with known locations and source signatures to simulate broadband sources. Then, while cavitation was generated in a tissue-mimicking agar gel using HIFU, an array was used to record the cavitation emissions, which were used to generate passive cavitation maps. This was first done using a high-resolution bistatic setup, and then with a clinically relevant monostatic arrangement of HIFU transmitter and array receiver. Finally, the monostatic arrangement was used to generate passive maps of cavitation in *ex vivo* bovine liver, and compared with tissue blanching. The results obtained using these experiments are given in the following chapters.

Chapter 4

Passive Mapping of Time-Invariant Scatterers

Cavitation is a stochastic process and obtaining repeatable measurements of cavitation activity even within a tissue-mimicking material is very challenging. It was therefore felt that, as a first step, insonifying a time-invariant scatter, chosen to be a metal wire, with broadband pulses produced by a single-element broadband transducer positioned at 90 degrees to the cavitation mapping array would enable initial validation of the methodology for mapping broadband sources without the added complexity of cavitation dynamics. This method also makes it possible to calibrate the linear array on receive, the results of which are presented in Section 4.1. In Section 4.2, the position of the wire within the field of view of the array is varied, and summation of the various signals is carried out so as to simulate multiple narrowband and broadband sources. The reader is referred to Section 3.4 for further details of the experimental setup and rationale.

4.1 Calibration of the linear array on receive

4.1.1 Frequency-dependent sensitivity of array elements

Figure 4.1 shows the results of the frequency calibration. The frequency sensitivity is a combination of strong bandpass filtering (*wall filtering*) in the 4.6–9.6 MHz band prior to IQ demodulation (see the Appendix) and of the nominal frequency response of the elements in the 5-10 MHz range.

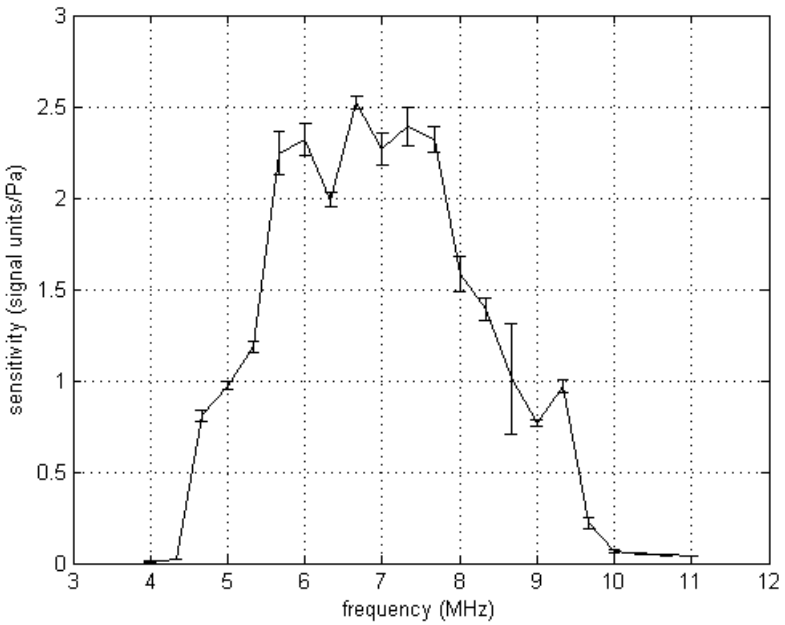

Figure 4.1: Frequency calibration of linear array elements. The average pressure sensitivity over 4 central elements were taken, with a maximum separation of 1.2 mm. Error bars show ±1 standard deviation. The combination of bandpass filtering in the 4.6–9.6 MHz band prior to IQ demodulation and the nominal 5-10 MHz mechanical response of the elements causes a strong rejection of signals outside the 4.6–9.6 MHz band.

As shown in Figure 4.1, the elements have a reasonably uniform response in the 4.6–9.6 MHz band. For simplicity, the mean sensitivity of the elements over the

4.6–9.6 MHz range, namely 1.15 signal units/Pa, is used hereafter. For sources with uniform frequency content in the 4.6–9.6 MHz range, such as cavitation emissions or the broadband pulses transmitted by the pulser-receiver, this sensitivity will be unbiased. However, for the 7.5 MHz sources encountered in Section 4.2.1, the correct sensitivity of 2.36 signal units/Pa is used.

The above results were obtained at a distance of 40 mm from the scattering source. To ensure that the pressure sensitivity is independent of the location of the source, the results of the spatial calibration are now considered.

4.1.2 Spatial calibration of the array

In order to characterize the spatial sensitivity of the array on receive, an acoustically small (0.02 mm diameter) wire intended to simulate a point source in the plane of the array was moved in 0.5 mm steps in the y-z directions. As discussed in Section 3.4 and illustrated in Figure 3.10, the scatterer will not have a uniform directivity pattern due to the dipolar scattering component created by the density contrast between the scatterer and the medium. However, for a fixed observation angle, the scattered pressure amplitude is still expected to vary inversely with distance. Moreover, normal to the propagation direction of the insonating wave, the dipolar term vanishes.

Figure 4.2 shows the signal amplitude received at the array in the y=0 plane and at various distances from the array (xy planes). A clear dipolar component can be seen in the images, with a visible preferential backscatter that was correctly predicted in Section 3.4. However, as previously discussed, the x=0 line is unaffected.

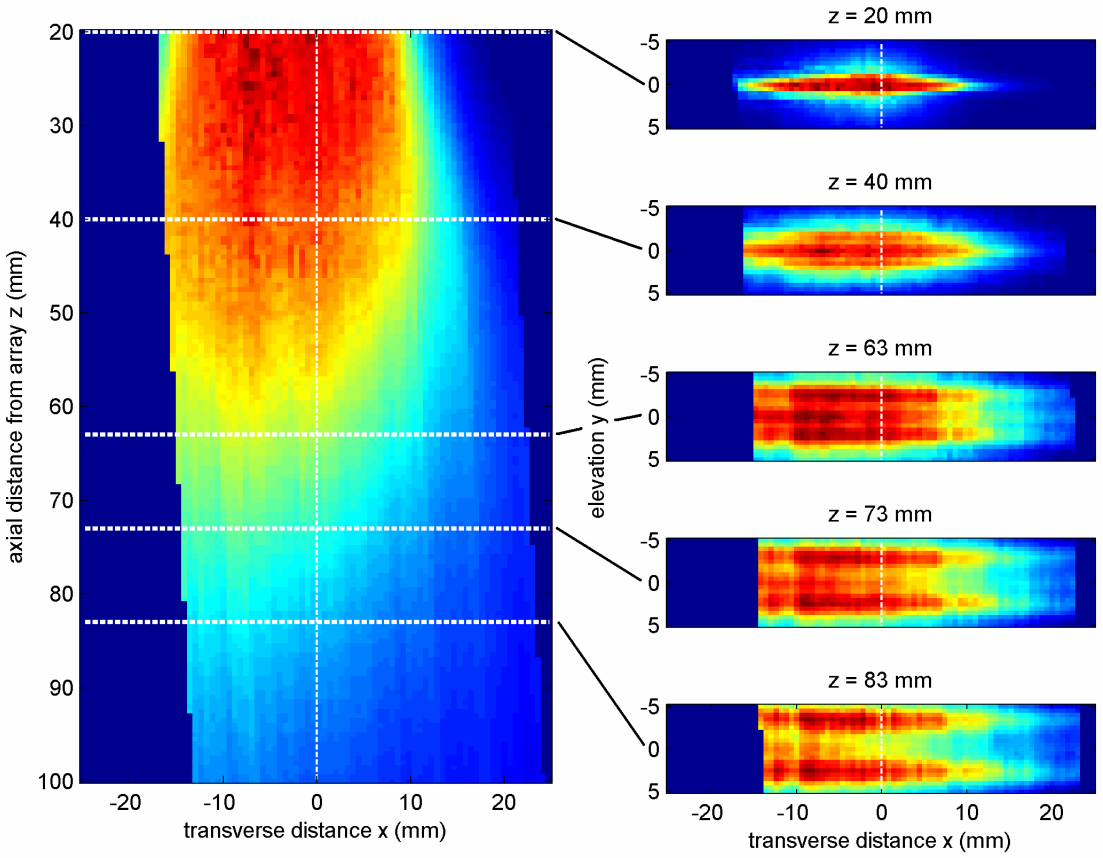

Figure 4.2: Spatial calibration of linear array elements. The cylindrical section of wire insonated by the broadband transducer is moved to different locations, while the acoustic power scattered by the wire is kept constant. The image on the left shows the pressure amplitudes received for scattering in the y=0 plane. The horizontal white dotted lines show the axial distances where cross-sections were taken in the x-y plane, shown on the right. In all images, preferential backscatter is clearly visible, arising from dipolar scattering. At the x=0 plane, the dipolar contribution is zero (see Figure 3.10).

Elevational focussing

An important feature of Figure 4.2 is that it shows spatial focussing within a $y \in [-5, 5]$ mm region. For the monostatic cavitation mapping experiment illustrated in Figure 3.12, the HIFU focus is at $z = 73$ mm, and the width of the HIFU beam is less than 5 mm. Since the array is only sensitive to 5 mm above and below the

x-z plane, the difference in arrival times for signals from broadband sources above and below the plane will be small compared to those sources which are in plane. This means that the (x,z) position of such out-of-plane sources will be accurately represented in the two-dimensional passive maps, with a maximum (axial) distortion of 0.2 mm at $z = 73$ mm.

Accounting for spatial spreading

Another important question that needs be confirmed in the context of a spatial calibration is whether the signal received by array elements does indeed scale as d^{-1}, as assumed in Section 2.3 for the passive reconstruction algorithm. The reason why this is not necessarily so is the fact that the array elements are cylindirically focussed in the y direction, meaning that considering them as point receivers is an approximation.

In order to determine the validity of this assumption, Fig 4.3 shows the change in signal received at the centre of the array (x=0) as the distance to the source is increased, both in-plane and increasingly out-of-plane. As shown in Fig. 4.3, the d^{-1} dependence provides a reasonably accurate description for distances of 40-100 mm, so that the pressure sensitivity obtained earlier in Section 4.1.1 is used for all distances.

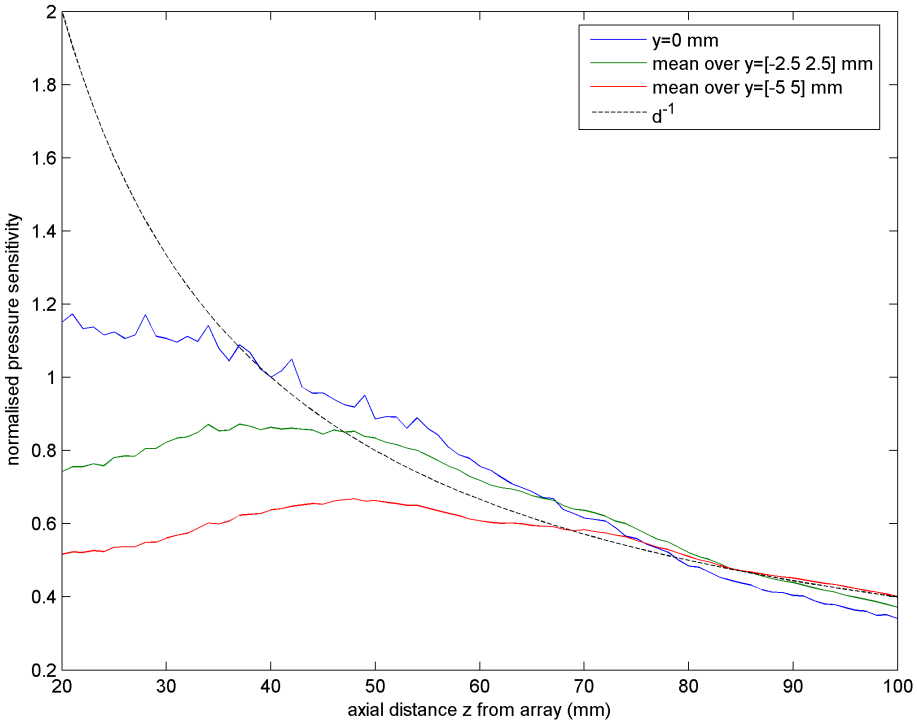

Figure 4.3: Comparison of array element spatial sensitivity models. The signal amplitude recorded at x=0 – where scattering is purely monopolar – is plotted with distance, normalised to the pressure received at z=40 mm using the absolute calibration in Section 4.1.1. For the monostatic and bistatic experimental setups described in Chapter 3, the HIFU focus is 38 mm and 73 mm from the array, respectively. For these regions, there is an approximately reciprocal variation between received pressure amplitude and distance, correponding to the decay of a monopolar source. Therefore, the pressure sensitivity obtained earlier at z=40 mm (Figure 4.1) is used for all distances.

4.2 Passive mapping of insonated scatterers

In the previous section, calibration of the linear array using wire scatterers allowed the passive mapping algorithm to yield physically meaningful values. This section describes results obtained from moving the wire to different locations and adding the signal received by the array signal at each location to simulate distributed sources. First, the 0.5 mm wire was placed so as to scatter at the HIFU focus in the mono-static setup – (0,0,73) mm – and the resulting passive map is compared with the scatterer moved in a 10 mm×10 mm cross formation in the plane of the array, with the HIFU focus at its centre. Then, the acquisitions from the spatial calibration (Section 4.1.2) are used to create linearly distributed semi-continuous sources.

4.2.1 Discrete sources in cross formation

Figure 4.4 shows passive maps of the 0.5 mm wire at the HIFU focus and in a cross formation around the HIFU focus. The source power at each location was kept constant. For both narrowband and broadband sources, going from a single source to a distributed source raises the maximum power on the map by about 20 %, probably due to leakage from one source power onto another. Nevertheless, in the broadband case, the cross formation can still be clearly resolved, unlike in the narrowband case.

The passive map of narrowband sources in cross formation (Figure 4.4) is curious: the frontal and distal sources are hardly discernible, and two artefacts appear near the centre of the map. However, narrowband sources tend to interfere with each

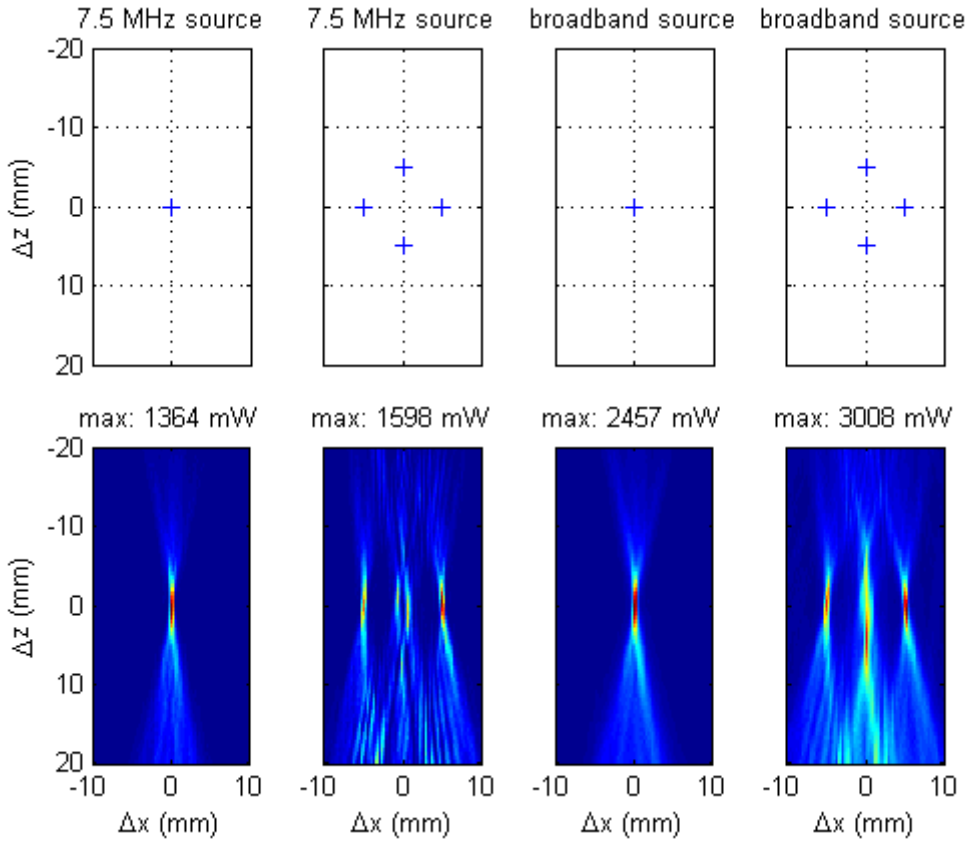

Figure 4.4: Passive maps of discrete sources in cross formation (in mW). In contrast to the interference observed with the 7.5 MHz source mapped in the leftmost two subplots, the cross formation can be clearly seen when the sources are broadband, as shown on the rightmost two subplots.

other due to their mutual coherence [184]. In Chapter 2, when two 7.5 MHz sources were varied in relative phase, their estimated powers, as well as their apparent position, changed (Figures 2.6, 2.7). Here too, when the phase of the distal source is varied, the frontal and distal sources appear with different powers (Figure 4.5). As for the two artefacts, these also appear in simulations (Figure 4.6). They arise from the constructive interference of the "St Andrew's cross" beams from the frontal and distal sources. In short, the quality of passive maps relies on the incoherence between sources; this topic will be revisited in the following two chapters.

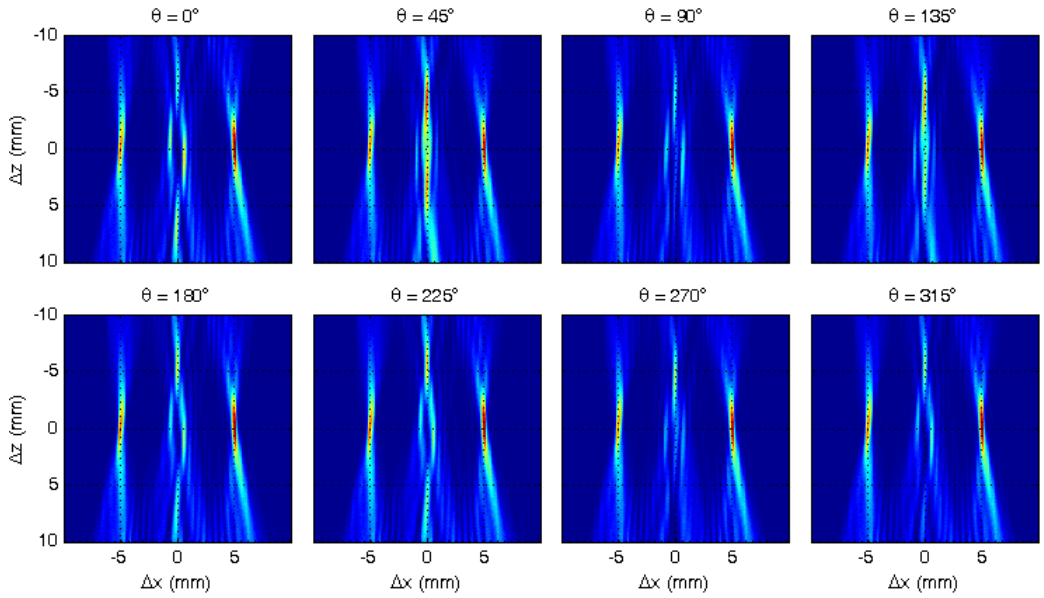

Figure 4.5: Passive maps of four 7.5 MHz sources in cross formation. The phase of the distal source is varied with respect to the phase of the original recording. The estimated powers of two interference artefacts near the centre of the maps, as well as of the frontal and distal sources, varies strongly depending on the phase.

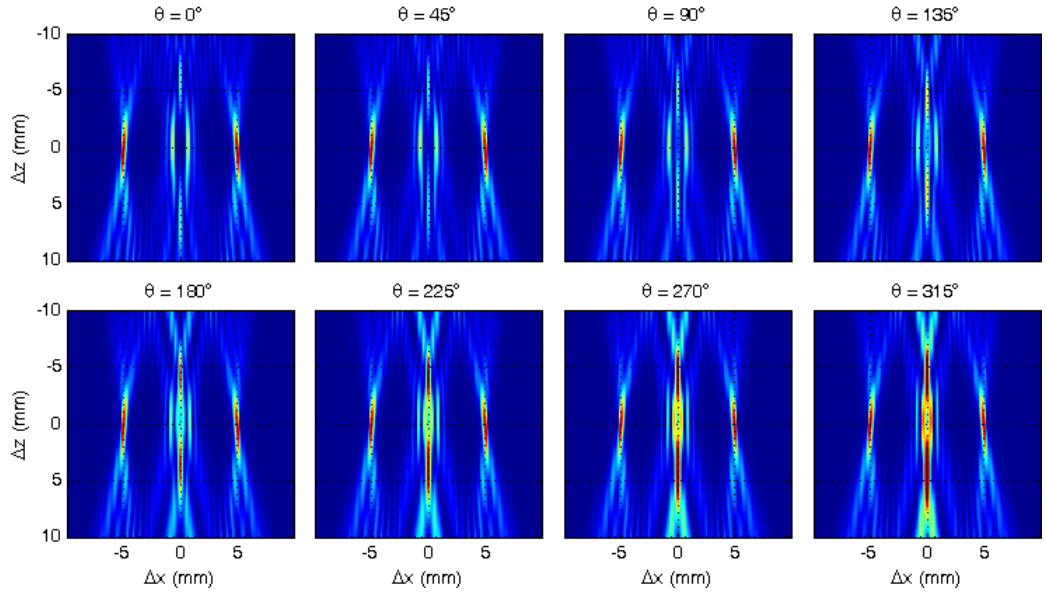

Figure 4.6: Simulated passive maps of four 7.5 MHz sources in cross formation. The phase of the distal source has been varied, which results in the variation of the estimated power of the frontal and distal sources, as well as of two interference artefacts near the centre of the maps (see also Figures 4.4, 4.5).

4.2.2 Semi-continuous linear source

In the clinically applicable monostatic setup shown on Figure 3.12, the HIFU focus is at z=73 mm, with a beam that extends primarily in the axial (z) direction, as shown in Figure 3.2. With increasing pressure amplitudes, the extent of the cavitation region was also accordingly expected to increase mostly in the axial direction (see Figure 3.14). Therefore, as a simple simulation, sources of varying extents (0 mm, 5mm, 10 mm and 20 mm) were simulated using the spatial calibration data obtained earlier in Section 4.1.2. Since the source strength of each point source was kept constant during the experiment, the array signals were later scaled by $1/\sqrt{K}$, where K was the number of sources added together, in order to keep the total source power constant.

Figure 4.7 shows the resulting passive maps. In the single source case, the acoustic power emitted in the 4.6–9.6 MHz range is 259 mW. As the source power is spread over increasingly large distances, the passive maps also spread accordingly.

4.3 Summary

This chapter has shown how, by scattering pressure waves off a wire, discrete point sources can be created. This can be used both to calibrate the linear array, and to create sources with a controllable spatial distribution, the latter making it possible to quantify the resolution and performance of the passive mapping system.

In the next chapter, cavitation will be generated close to the linear array in an effort to learn about the dynamics of cavitation in an agar tissue-mimimicking gel.

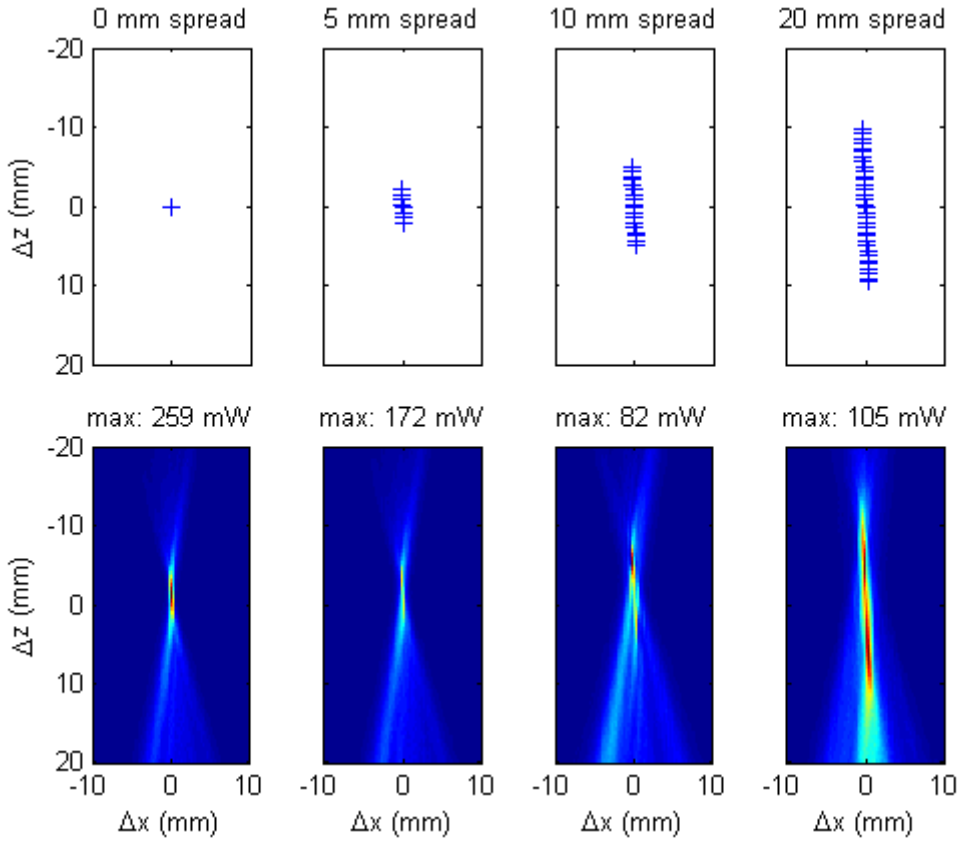

Figure 4.7: Passive maps of semi-continuous linear sources (in mW). As the axial spread of the sources increased from 0 mm (left) to 5 mm, 10 mm, and 20 mm (right), the total acoustic power is kept constant and is therefore distributed among the sources. The total acoustic power is estimated from the one-source case to be 259 mW.

Chapter 5

Bistatic Passive Cavitation Mapping

In the previous chapter, controllable sources were created by exciting a metal wire with narrowband and broadband signals from a broadband transducer, enabling testing of the passive mapping algorithm with different source distributions. Passive mapping is now applied to HIFU-induced cavitating bubbles in a tissue-mimicking agar gel. In order to acquire high resolution maps of cavitation activity, the array is placed transversely to the HIFU transducer, at a distance of 36.3 mm from the HIFU focus, as depicted in Figure 3.11.

This chapter has three aims, listed below, and dealt with in the respective sections to follow:

Investigate the spatial extent of cavitation with increasing pressure amplitudes

By measuring the pressure amplitude at which cavitation begins to occur – the cavitation threshold – and using the spatial calibration of the HIFU transducer, the spatial extent of cavitation activity can be predicted for short exposure durations in a homogeneous medium such as agar. Such predicted regions of cavitation can be compared with actual regions of cavitation. The cavitation maps will establish whether the cavitating bubbles are limited to discrete locations, or whether they should be seen as forming a bubble cloud or continuum.

Observe interactions between the HIFU wave and cavitating bubbles

In a simplified model of cavitation, each candidate bubble (of adequate size and composition) will cavitate inertially every time that it experiences the rarefactional half-cycle of the incident HIFU pressure wave. With increasing pressure amplitudes and temperatures, however, cavitation emissions will be periodic over an increasing number of cycles, gradually tending towards chaotic behaviour. Such chaotic behaviour may also be enhanced by cavitation emissions from nearby bubbles. Increased chaoticity will decrease the spatial coherence between cavitation emissions, which is an important factor in improving the quality of images in the monostatic setup, where the relatively significant axial blurring of the sources may cause interference effects in the images. Hence, it would be of interest to see how bubble emissions are related to each other.

Compare passive cavitation mapping with active cavitation detection

One of the main methods of monitoring HIFU treatment is by B-mode hyperechogenicity monitoring, which relies on active (pulse-echo) detection of bubbles while HIFU is turned off. However, research [136; 137] has shown that hyperecho-based imaging is a less sensitive marker of cavitation than passive cavitation detection. This chapter seeks to confirm the role of bubble dissolution in this by comparing the passive maps with the pulse-echo traces of a broadband transducer after HIFU is turned off, with a temporal resolution (pulse repetition period) of 500 µs.

5.1 Mapping of discrete bubble distributions

An agar tissue-mimicking gel with a cross-section of 25 mm×25 mm in the array imaging plane was exposed to 1.067 MHz HIFU for 2 seconds, as illustrated in Figure 3.11. Passive cavitation maps were generated for peak rarefaction focal pressures (PRFPs) of 1.6–4.8 MPa, with the cavitation threshold previously measured at 1.2 MPa (for 1.06 MHz). Since the pulses of the broadband transducer were transmitted at regular intervals, it could be ensured that passive maps were generated during "silent periods" when the transducer was not interrogating. This meant that the passive maps were not affected by scattering from the broadband pulses, although their effect was in any case minimal. (The source power of passive scattering maps, obtained when HIFU was off, was about a hundredth of the source power of passive cavitation maps when HIFU was on. Interestingly, passive scattering maps showed similar information to hyperecho traces obtained using the A-line transducer.)

Since all sources were within 0.5 mm of a distance of $z = 36.3$ mm from the

array, and the axial resolution at this distance is 1.2 mm (1.77), the cross-section of the maps at $z = 36.3$ mm with time was plotted for easy visualization. The cross-sections, together with predicted regions of cavitation, are shown in Figure 5.1.

The predicted regions of cavitation are somewhat wider than the actual region of cavitation. For lower pressure amplitudes, the number of cavitating bubbles or bubble clusters is relatively low (3-10), while increasing pressure amplitudes create a relatively large number of bubbles that can be well approximated by a bubble cloud. With time, the bubbles seem to be pushed away from the HIFU transducers, probably due to the acoustic radiation force of the HIFU beam. Although significant variation was found in the locations of the bubbles between exposures and samples (in total, 24 exposures were carried out across 3 samples), the increasing number of bubbles with increasing HIFU pressure, as well as the "tunnelling" of bubbles, was a general phenomenon observed for all exposures.

It is interesting to note that while increasing the pressure amplitude seems to increase the number of cavitating bubbles, the source power shown for each bubble is of the same order of magnitude. As mentioned in the earlier chapter, although the cavitation maps only give source powers corresponding to emissions in the 5-10 MHz range that have not been attenuated while reaching the receiver, these are expected to be directly proportional to the total power emitted by the bubbles, the majority of which is absorbed within 1 mm of the cavitating bubbles [56].

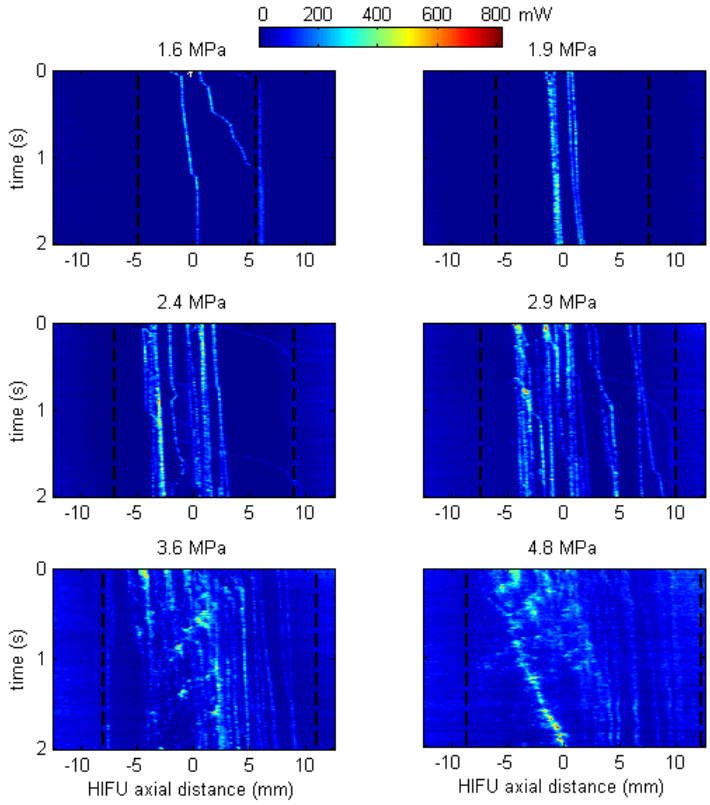

Figure 5.1: High-resolution passive cavitation maps in agar for different peak rarefaction focal pressures (PRFP). To ease visualization of the cavitation maps, cross-sections of the maps were taken at a distance of 36.3 mm from the linear array. Time passes vertically while the horizontal axis depicts distance from the HIFU focus, with positive distance leading away from the HIFU transducer. Thus, for each cross-section in time, the HIFU transducer is to the left of the passive maps while the linear array, placed perpendicularly to the HIFU transducer, is above the maps (Figure 2.8). The black dashed lines show the expected regions of cavitation based on a cavitation threshold of 1.2 MPa and the calibrated pressure profile of the HIFU transducer.

The cavitation maps show several interesting features. Many bubbles are seen to move away from the HIFU transducer, possibly due to acoustic radiation force. As the pressure increases, the bubble distribution tends towards being spatially continuous. All the while, however, it seems that the acoustic energy radiated by each bubble is relatively constant: for each bubble, around 400 mW leaves the agar gel in the 5-10 MHz range.

5.2 Resolution of discrete source signatures

The previous section has shown the evolution of cavitation distributions with time. The nature of the cavitation emissions decomposed by spatial origin is now sought, which can be assessed by reconstructing the source strength field. The first example in Figure 5.1, at 1.6 MPa peak rarefaction focal pressure (PRFP), serves as a useful starting point, as three bubbles or bubble clusters can easily be distinguished at first, with two of these bubbles appearing to merge around half-way through the exposure.

Figure 5.2 shows the cavitation emissions for each bubble at four different instances during the 1.6 MPa PRFP exposure. The time scale for each emission trace has been adjusted so that the reference frame moves with the propagating HIFU wave. Use of the moving reference frame allows the observation of some interesting emission behaviour, with collapses seemingly synchronised by the HIFU wave oscillations (see Figure 5.2 for an extended discussion).

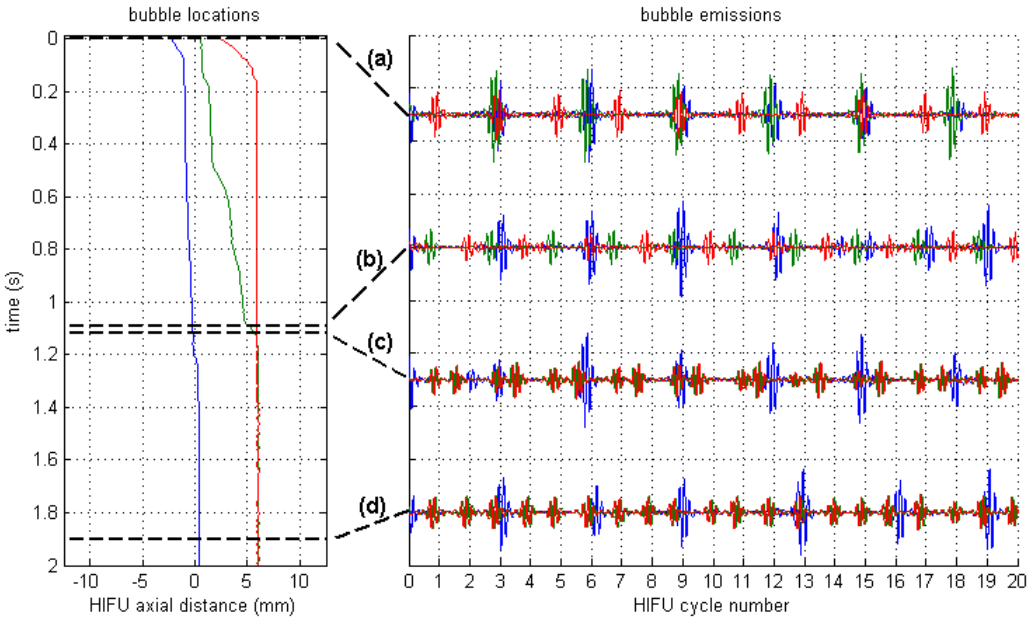

Figure 5.2: Bubble emissions from discrete locations at 1.6 MPa PFRP. Left plot: locations of the bubbles along the HIFU axis with exposure time, with bubbles tending to move away from the HIFU transducer, probably due to acoustic radiation force. Right plot: estimated bubble source strengths $\tilde{q}$ (Section 2.3.2) at different exposure times, using the propagating HIFU wave as the reference frame (each vertical tick corresponds to 20 µg µs^{-2} rate of change of mass outflow). Note the ringing of the cavitation signal due to the finite bandwidth of the transducer (see Figure 1.2).

(a) At the start of HIFU exposure, the blue and green bubbles both exhibit period tripling, collapsing with the same HIFU wavefront, while the red bubble undergoes period doubling, sharing its collapse with the other two bubbles every 6 HIFU cycles.

(b) As the green bubble moves away from the focus towards the red bubble, it also starts to adopt period doubling, with the two bubbles emitting alternately.

(c) The green and red bubbles are so close that the emissions cannot be separated. In contrast to the blue bubble, the proximity of the two bubbles seems to confer some temporal instability to their collapse.

(d) The green and red bubbles now seem to collapse in an orderly fashion, although at a slightly earlier point in the HIFU cycle than the blue bubble. It is not known whether the two bubbles are collapsing alternately as in (b), or whether they collapse every HIFU cycle, either as a cluster or as one coalesced bubble.

Although Figure 5.2 shows some remarkable synchronicity in the bubble emissions, the emissions are not always so stable or orderly, especially at higher pressures. Figure 5.3 shows the source strength field along the HIFU axis ($z = 36.3$ mm) for all six pressures discussed in the previous section, again using the propagating HIFU wave as the reference frame. With increasing pressures, the collapses become less stable and less spatially coherent. When the array is placed coaxially with the HIFU transducer, as in the next chapter, the axial resolution of the array is limited to 5 mm. Therefore, this spatial incoherence is important in reducing interference between sources (see Section 2.3.4).

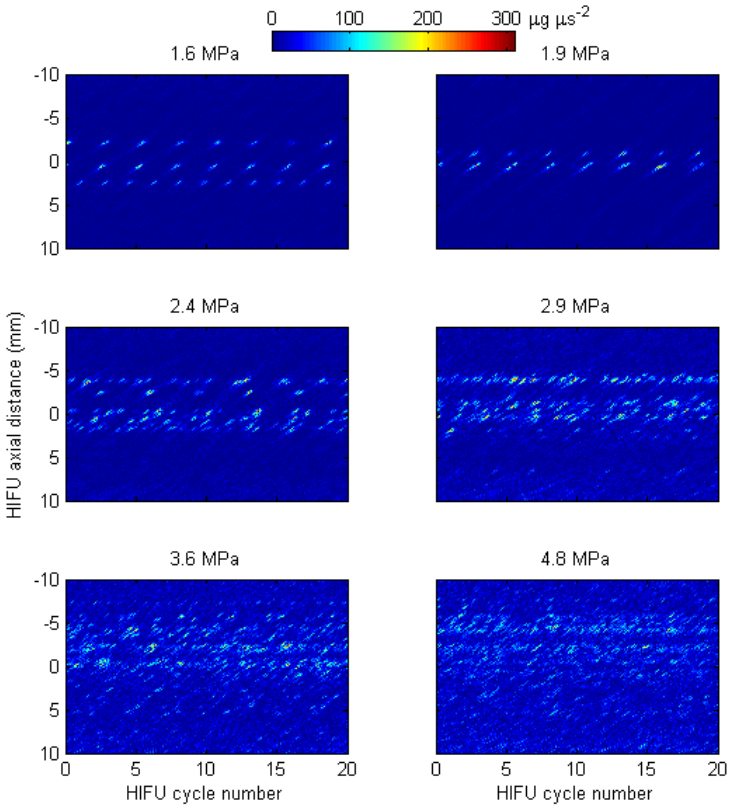

Figure 5.3: The source strength field $\tilde{q}(x, z = 36.3 \text{ mm}, t)$ from cavitating bubbles along the HIFU axis. The vertical axes represent distance from the HIFU focus, with positive distance leading away from the HIFU transducer. As in Figure 5.2, the time axis is referenced to the propagating HIFU wave, so that collapses caused by the same HIFU wave appear directly above each other. For each peak rarefaction focal pressure (PRFP) shown, the first frame of the exposure is used to generate the source strength field. It can be seen that with increasing pressures, cavitation becomes less temporally stable and less spatially coherent.

5.3 Comparison with pulse-echo

Cavitating bubbles, with their high air content, serve as strong scatterers of ultrasonic pulses, which could be used to localise the bubbles. However, the relatively high power of cavitation emissions makes it difficult to filter out the echoes from the emissions, and pulse compression techniques to increase signal-to-noise in pulse-echo localization are complicated by the changing shape of the scatterer. Therefore, the scattered signal can only be recovered after the HIFU is turned off. In effect, the broadband transducer produces pulse-echo traces that are like the central A-lines produced during hyperecho-based B-mode imaging, but at a higher frame rate.

With a pulse repetition period of 500 µs, the first usable echo is obtained within 500 µs of the HIFU being turned off. These echoes are shown in Figure 5.4, together with the corresponding passive cavitation maps generated during HIFU exposure. (Registration between passive maps and ACD A-lines was possible due to the prior alignment of the ACD and linear array with respect to the HIFU focus, as described in Section 3.3.1.) There is good correspondence between the cavitation maps right before HIFU is switched off, and the echoes of the broadband transducer right after HIFU is switched off. However, shielding from bubbles nearer to the HIFU transducer is visible on the A-lines, most markedly demonstrated by the gradual disappearance of the back wall of the agar gel as the pressure amplitude is increased.

The comparison of active and passive detection methods highlights two limitations of hyperecho monitoring, namely the effect of bubble movement and dissolution. In the former, a bubble that moves during HIFU exposure may heat regions of tissue that would not be indicated by the post-exposure A-line, although bubble

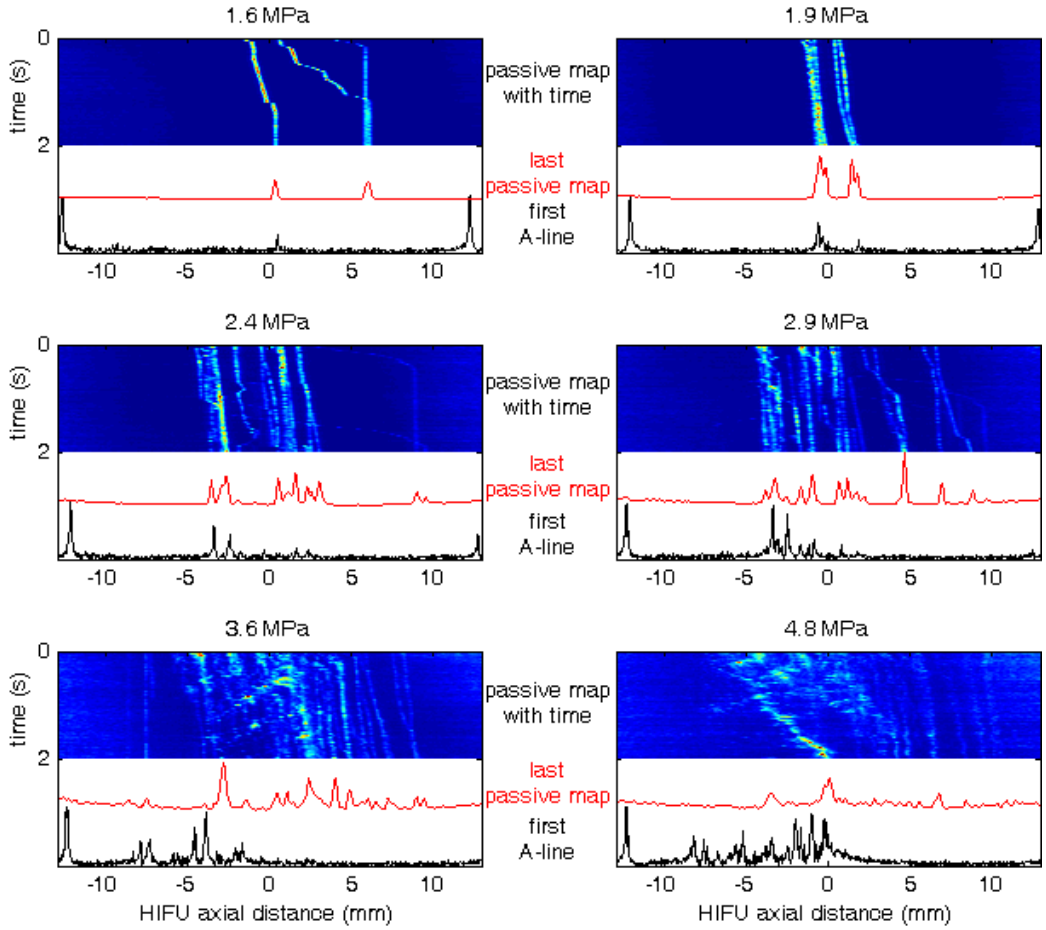

Figure 5.4: Comparison of passive maps with pulse-echo traces (A-lines). The passive maps of Figure 5.1 are shown next to the first A-line after HIFU has been switched off (for clarity, the envelope of the echo has been taken). The front wall of the agar phantom is clearly seen on all A-lines, at -12.5 mm relative to the HIFU focus. However, with increasing pressure amplitudes, the back wall at 12.5 mm is increasingly shielded by bubbles, and thus increasingly less visible on the A-lines. In spite of the shielding, there is good correspondence between the last passive map during HIFU exposure and the first A-lines after HIFU exposure. Interestingly, at 4.8 MPa, the prefocal hyperechoes detected on the first A-line are not detected on the last passive map. While some can be correlated to past cavitation events, it is likely that there are also boiling bubbles.

movement in tissue is less expected than in agar. More importantly, a bubble that stops cavitating will start dissolving due to surface tension, decreasing the scattered echo until it reaches the noise floor. Therefore, bubble dissolution will start as soon

as the HIFU is switched off, if indeed the bubble has not already stopped cavitating due to a change in tissue or bubble conditions.

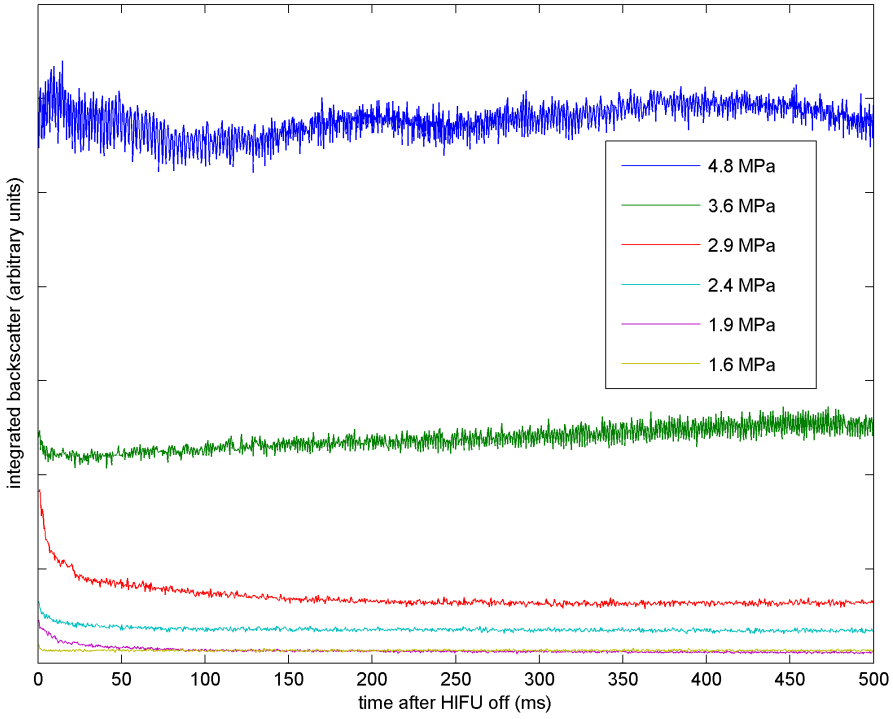

Figure 5.5: Dissolution of bubbles with time after different HIFU exposures. The backscattered signal from inside the agar gel is integrated after HIFU exposures of different peak rarefaction focal pressure (PRFP). At the lowest PRFP of 1.6 MPa, bubbles dissolve within 5 ms, whilst at 3.06 MPa PRFP and above, bubbles remain stable for over 500 ms. In the intermediate range of 2.4, 2.9 MPa PRFP, some of the bubbles remain stable for over 500 ms, as indicated by the fact that the integrated backscatter does not reach the "scattering noise floor" observed at 1.6 MPa and 1.9 MPa.

Figure 5.5 shows how the backscattered echo integrated over the inside of the gel changes with time after HIFU has been switched off. Depending on the pressure amplitude used, bubbles can dissolve within 5 ms, or remain stable over 500 ms. Since larger bubbles take more time to dissolve, it is unsurprising that higher

pressures create backscatter traces that take longer to dissolve.

When applying the above findings to the efficacy of hyperecho-based treatment monitoring, two important considerations are in order. Firstly, bubble dissolution is established here from a practical viewpoint, namely the backscatter reaching the noise floor, regardless of any bubble nucleus that may remain in the medium. Tissue is less homogeneous than agar, and therefore the bubble will "dissolve away" earlier. Secondly, the A-lines were generated at a rate of 2kHz, while typical B-mode frame rates go up to 100 Hz. Therefore, by showing that bubbles can dissolve away within 5 ms in the current setup, it is considered highly likely that a B-mode imager will also miss it in tissue, as indeed is the case [138]. The current results demonstrate the role of dissolution for this absence of detection.

5.4 Summary

In this chapter, cavitation has been observed with high spatial resolution due to the proximity (36.3 mm) of the linear array to the HIFU focus. Below 2 MPa peak rarefaction focal pressure (PRFP), bubbles were observed at discrete locations, and often cavitated synchronously to the HIFU insonation. The passive source reconstruction technique also allowed the observation of cavitation dynamics between bubbles. In short, a novel technique has been developed that complements existing high-speed photography.

Above 2 MPa PRFP, cavitation emissions are more chaotic and the spatial distribution of cavitation can be approximated as continuous.

The lack of spatial coherence between sources helps with passive mapping in

the monostatic arrangement of the next chapter, where a greater distance from the HIFU focus (73 mm) degrades the axial resolution of passive maps, and interference between coherent sources could therefore pose a problem.

Finally, the passive maps have been compared with pulse-echo data from a broadband transducer coaxially aligned with the HIFU transducer. It has been observed that bubbles can dissolve away within 5 ms of switching off HIFU, which is quicker than typical B-mode frame rates of up to 100 Hz. This explains the results of previous research [136; 137], where B-mode hyperecho was shown to be a less sensitive method of cavitation detection than passive cavitation detection during HIFU treatment.

With these observations in mind, the next chapter will consider the results of passive mapping with the linear array placed coaxially with the HIFU transducer, as implementable during clinical HIFU treatment.

Chapter 6

Monostatic Passive Cavitation Mapping

This chapter presents results obtained using a linear array placed coaxially with a HIFU transducer (Fig. 3.12), a monostatic arrangement that would be directly implementable during clinical HIFU therapy. Cavitation maps are first presented for a homogeneous agar gel, demonstrating successful mapping of contiguous cavitation regions, then in an inhomogeneous agar gel, where disjoint regions are mapped, and finally ox liver where cavitation is mapped during HIFU ablation.

6.1 Cavitation in agar tissue-mimicking phantoms

6.1.1 Cavitation in a contiguous region

It has been mentioned previously that by calibration of the pressure field caused by the HIFU transducer and measurement of the cavitation threshold, the region

of agar where cavitation is expected to occur can be predicted (see Figure 3.14). However, the high-resolution passive maps in the previous chapter showed that these predictions are not always accurate (Fig. 5.1). Therefore, to provide additional validation of the passive maps using the coaxial setup, two single-element passive cavitation detectors (PCDs) have also been employed, one placed confocally with the HIFU transducer, while the other was placed 5 mm prefocally (the resolution limit of passive mapping using this setup). In all, 47 exposures were carried out on 5 agar gel samples. Although there was variation in the passive maps obtained across different samples and exposures, there was better repeatability between the initial spatial distribution of cavitation for a given HIFU pressure.

Figure 6.1 shows the cavitation maps in agar for threee HIFU exposures of increasing pressure. The maps have been generated for the first recorded frame with cavitation, that is, within 10 ms of the HIFU being switched on. Expected regions of cavitation, and the signal variance from the PCDs, are also shown. In the first example, the cavitation threshold is only exceeded at the focus, and single bubble cavitation is expected there. Accordingly, there is negligible signal on the pre-focal PCD. With increasing pressure amplitudes, the extent of the cavitation region is predicted to increase, which is indeed observed on the cavitation maps. While the confocal PCD signal remains unchanged, a signal now appears on the pre-focal PCD, confirming that cavitation is starting to occur in the pre-focal region.

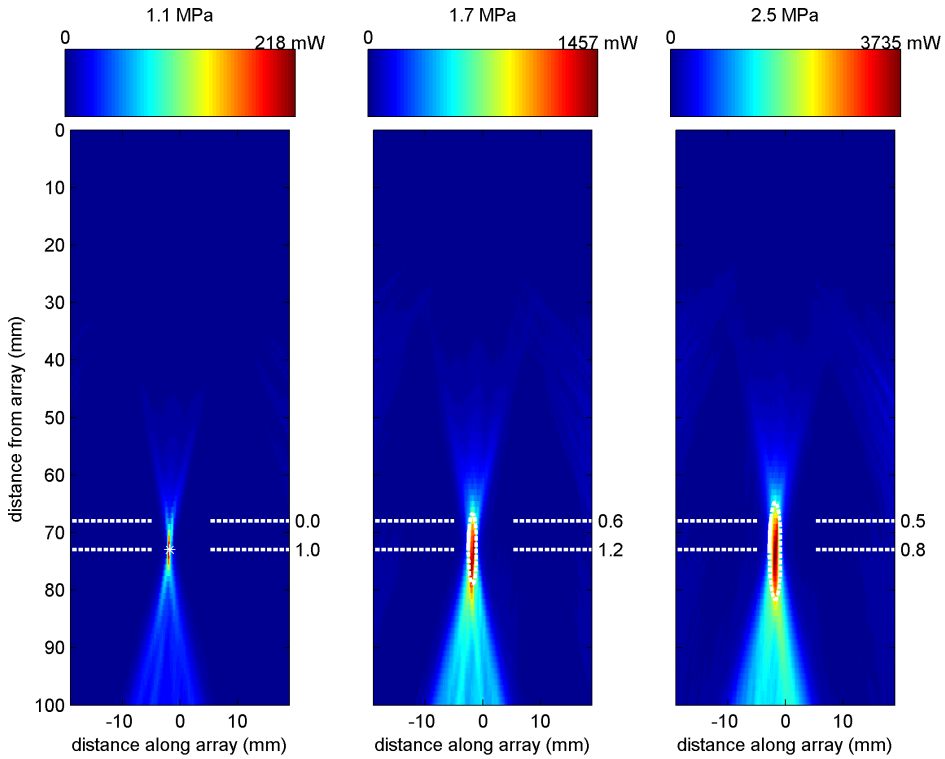

Figure 6.1: Cavitation maps in agar gel for the first recorded frame of HIFU exposure. The dotted ellipses show the predicted regions of cavitation based on prior calibration of the HIFU pressure field and measurement of the cavitation threshold. The white dotted lines depicted the axes of PCDs, whose signal variances are shown next to the lines. There is good correspondence between the cavitation maps and the predicted regions of cavitation shown by the ellipses. Furthermore, the pre-focal (top) PCD variance only detects cavitation at the higher two pressures, providing further confirmation of the passive maps, which also suggest that prefocal cavitation only happens at the higher pressures.

Assessment of signal quality

It is deemed useful at this point to show the raw channel data that was used to generate the passive maps in agar. This is because the quality of passive maps is highly dependent on the quality of the channel data, and channel data obtained from cavitation in homogeneous agar will provide a good comparison with later experiments with tissue (whose results will be shown in Section 6.2).

Figure 6.2 shows the channel data used to generate the passive maps in Figure 6.1. In contrast with higher pressures, emissions at 1.1 MPa PRFP, which arise from a single bubble, can be clearly distinguished. The bubble is seen to cavitate every cycle of the 1.06 MHz insonation.

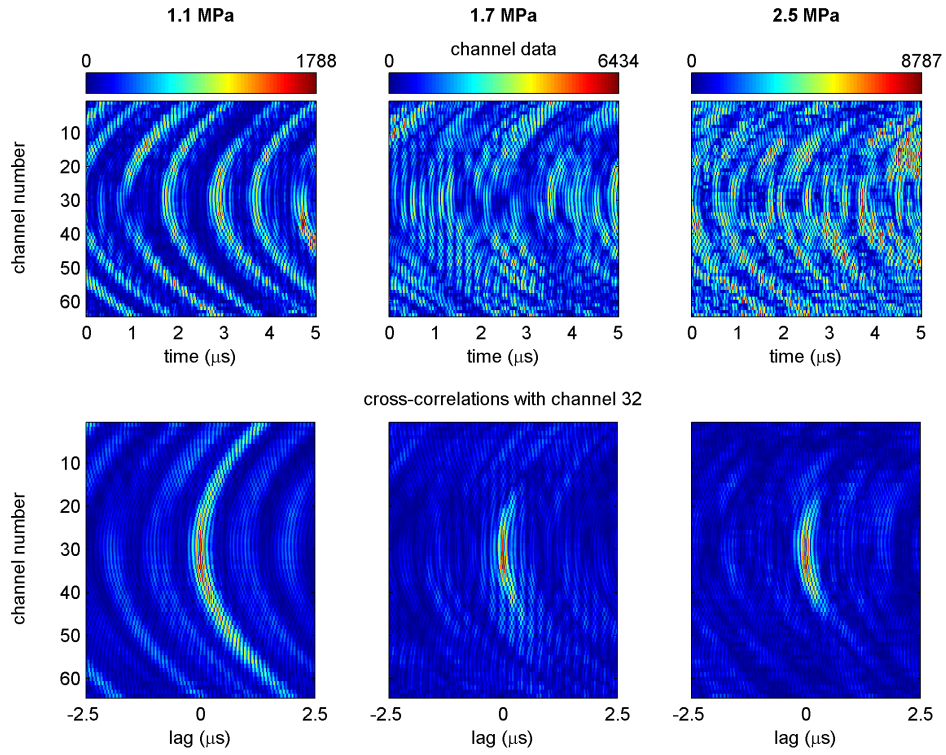

Figure 6.2: Channel data of cavitation in agar gel. The top images show magnitude plots of the channel data received by the array (with the colorbar showing the signal units). The bottom images show the cross-correlation of a central element signal with the other elements, revealing the delay in the emissions arriving to the elements with respect to the central element. At the lowest pressure, the single bubble emissions can be clearly seen in the channel data, producing a clear parabolic delay profile in the corresponding cross-correlation image. At higher pressures, bubble emissions arrive from different depths, with different delay curvatures. This causes a blurring at the edges of the cross-correlation images.

Figure 6.2 also shows cross-correlations of the channel data with a central element

(connected to channel 32). This allows checking the delay in the arrival of emissions at the elements, relative to the central element. For a single source, a circular arrival profile is expected, which becomes a parabola under the Fresnel approximation (see Section 2.3.2). The minimum of the parabola corresponds to the position of the cavitating bubble in the x-direction (along the array), while the radius of curvature of the parabola yields the distance of the bubble from the array. At 1.1 MPa PRFP, Figure 6.2 clearly shows that emissions are arising from a single location, while at higher pressures, bubble emissions from different depths cause a superimposition of parabolas with varying radii, and hence blurring at the edges.

For all three pressure settings, the channel data, and the cross-correlation data obtained from it, show good signal quality, with continuous delay profiles and a high signal-to-noise (SNR) ratio. Since passive mapping is equivalent to taking the sum of all cross-correlation pairs [184], the signal quality observed on the cross-correlation of one channel with all the others is directly related to the final passive map.

6.1.2 Cavitation source power versus focal temperature

Previous research has shown using single-element PCDs that the occurence of inertial cavitation greatly enhances heating during HIFU exposure [19; 20; 3]. Accordingly, Figures 6.3 and 6.4 show the correlation between the source power at the HIFU focus, estimated using passive mapping, and the temperature rise measured at or near the HIFU focus using a thermocouple.

In Figure 6.3, the maximum temperature rise at the HIFU focus is plotted against peak rarefactional focal pressure (PRFP) for 2 s exposures. The maximum focal

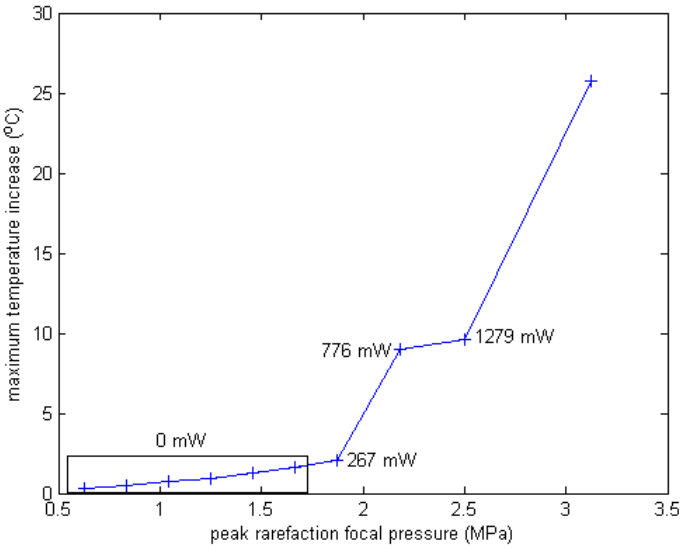

Figure 6.3: Temperature rises in agar gel for different HIFU pressures. The values of power correspond to the temporal peak focal source power estimates obtained using passive mapping. Below 2 MPa PRFP, little cavitation is observed and temperature increase is caused by linear heating only. With the onset of cavitation, the temperature increase rises significantly.

source power recorded over the 2s exposure is also shown. In this agar gel, the cavitation threshold was at 1.9 MPa PRFP, that is, higher than the usual 1.1 MPa, due to an extended degassing duration. In any case, it can be seen that as the level of cavitation increases, the maximum change in temperature increases above that expected using linear heating.

In order to be certain that the increased heating observed is not due to another phenomenon such as non-linear heating, whose effects are more pronounced at higher pressures, repeated exposures at 4.2 MPa PRFP were carried out. The repeated exposures deplete the cavitation nuclei, so that temperature increase with and without cavitation can be recorded, while keeping all other heating contributions constant. To prevent cavitation damage to the thermocouple, as well as prevent any thermocouple artefacts, the thermocouple was placed 2 mm transversely to the HIFU focus,

at a pressure minimum (see the relevant spatial calibration in Figure 3.2).

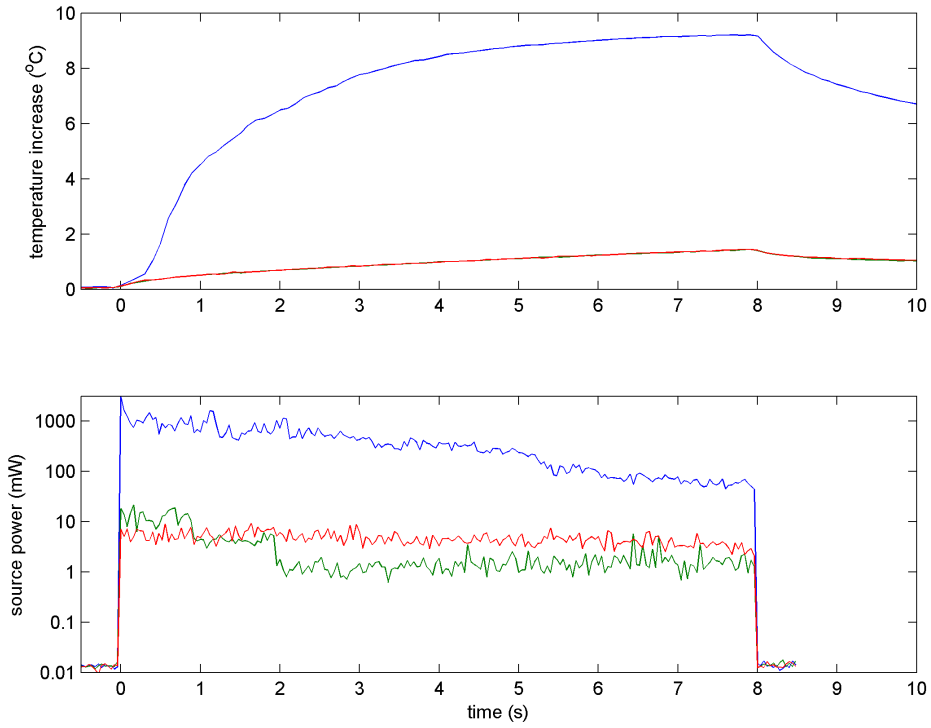

Figure 6.4: Temperature rise with and without cavitation at 4.2 MPa PRFP. Temperature rise was measured 2 mm transverse to the HIFU focus to avoid damage to the thermocouple and cavitation-induced measurement artefacts. Focal source powers were calculated using passive mapping. The same spot of agar gel was insonated three times, with blue, green and red representing each insonation in turn. After the first exposure, the level of temperature increase substantially decreases, with the temperature profiles of the second and third exposures being very similar. The level of cavitation also drops substantially, showing that cavitation is indeed responsible for the increased rate of heating observed at high pressure amplitudes (as shown in Figure 6.3).

The results of the repeated exposures are shown in Figure 6.4. After the first exposure, the temperature rise drops by a factor of 6.4, while cavitation power drops by a factor of over 100 to thermally insignificant levels (variations in source power between the second and third exposures cause insignificant changes in temperature rise). Hence, in these experiments, cavitation is the dominant source of heating.

6.1.3 Cavitation in disjoint regions

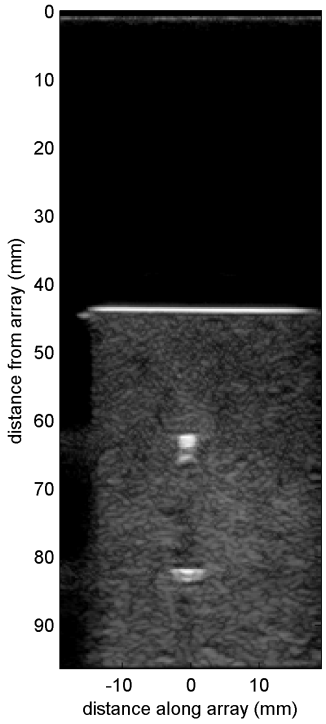

Figure 6.5: B-mode ultrasound image of flow channels in agar gel. The two channels are located 63 mm and 83 mm from the array, and the HIFU focus is positioned exactly half-way between them at 73 mm from the array. A highly hydrophobic talc suspension is flowing through both channels, hence their brightness. Since talc suspension has a much lower cavitation threshold, judicious choice of the HIFU intensity can cause cavitation in both channels without causing cavitation in the surrounding agar gel. The apparent difference in channel widths is due to the depth-dependent lateral resolution of the image.

Using the flow channel material described in Section 3.3.4, cavitation can be selectively instigated in none, either or both channels, by flowing either pure water or a highly hydrophobic talc suspension through the channels (see Section 3.6.1 for experimental details). Figure 6.5 shows a B-mode ultrasound image of the flow channels in agar. In Figure 6.6, cavitation maps are shown when cavitation is

created in the front channel, back channel, and finally both channels. There is good correspondence between the cavitation maps and the position of the flow channels, confirming the ability of the cavitation mapping technique to simultaneously map disjoint regions of cavitation activity. It is, to the best knowledge of the author, the first time that mapping of contiguous and disjoint regions of cavitation activity during HIFU exposure, without the need to turn off the HIFU transducer, has been demonstrated.

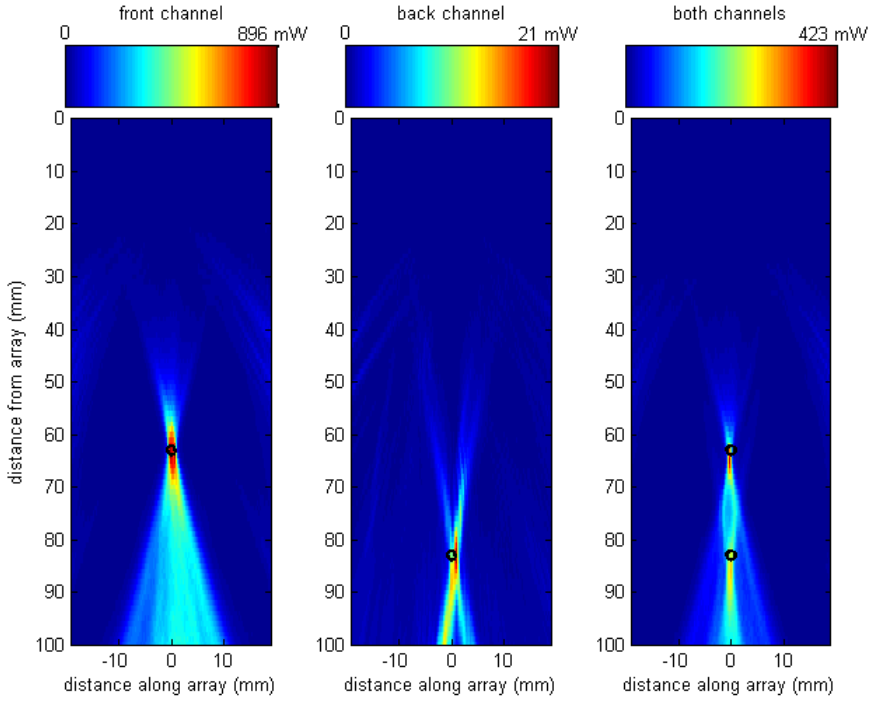

Figure 6.6: Cavitation maps in flow channels. By choosing whether to flow purified water or talc suspension through the channels, cavitation is selectively instigated in the front channel (left image), back channel (central image), or both channels (right image).

6.2 Cavitation in tissue

This section presents the results of cavitation mapping in bovine liver tissue. First, it is important to highlight the differences found between working in agar tissue-mimicking gel and tissue, and these are detailed in Section 6.2.1. Next, passive mapping and B-mode hyperecho are compared in their ability to detect lesion formation. Finally, cavitation maps are used to predict regions of lesioning and these are compared with visible (blanched) regions of lesioned tissue.

6.2.1 Extending passive cavitation mapping to tissue

Up to now, passive maps have been generated for cavitation in agar gel. Agar has many properties that make it easy to detect cavitation. Its speed of sound is close to that of water and attenuation is very low over the frequency range of interest (see Table 3.4). Agar gel is also relatively homogeneous, causing little scattering of cavitation emissions. As has been noted in the previous section, the level of harmonics from non-linear propagation was also relatively low in the investigated pressure range, which went up to 4.2 MPa peak rarefactional focal pressure (PRFP).

As expected, generating passive maps for cavitation in tissue poses several difficulties when compared with agar. These difficulties are discussed below. During the discussion, the reader is continually directed to Figure 6.7, which compares channel data received during single bubble cavitation in agar and liver.

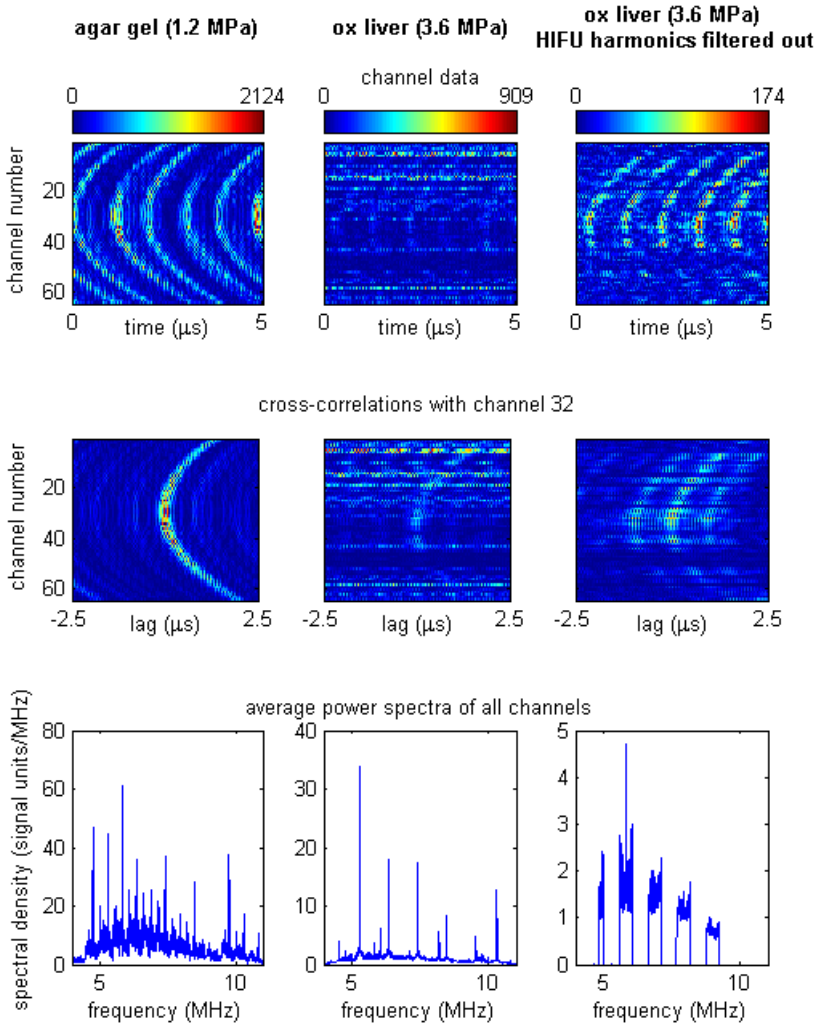

Figure 6.7: Comparison of single bubble recordings from agar gel (left column), ox liver (central column), and ox liver with 0.6 MHz bandstop filters centred at the harmonics of the 1.06 MHz HIFU wave (right column). The resulting channel data, arrival profiles (obtained using cross-correlation), and average power spectra are shown. In agar gel, bubble emissions in the channel data can be clearly observed, generating a clear parabolic delay profile in the cross-correlation image. Spectral peaks arise from the stable oscillation of the cavitating bubble. With ox liver, the channel data contains significant harmonics. These harmonics are significantly stronger on some channels, and the identity of these channels changes from one exposure to the next, suggesting some interference effect of the scattered harmonics of the non-linearly propagated HIFU wave. Filtering out the harmonics with bandstop filters reveals a clearer picture of the cavitation emissions. However, tissue inhomogeneities, and a loss of cavitation signal from filtering, cause signal degradation.

Speed of sound

The speed of sound in liver at 37°C, 1615 m/s (see Table 3.4; by comparison, [142] suggests 1597–1639 m/s), is significantly higher than that of water at the same temperature, 1524 m/s. For a cavitation emission at the HIFU focus to reach the centre of the array, the pressure wave must travel 20 mm through tissue and 53 mm through water, creating an effective speed of sound of 1548 m/s. For arrivals away from the array centre, refraction will distort the wave. However, this effect is minimal: using Snell's law to simulate refraction across the tissue-water interface, the curvature of arrivals produces an effective speed of sound of 1547 m/s.

Although emissions at different depths of tissue will cause changes in the effective speed of sound (at zero tissue depth, the effective speed of sound will be that of water, 1524 m/s), distance errors are less than 1 mm. Therefore, for simplicity, a speed of 1548 m/s is adopted for all depths when performing cavitation mapping. Incidentally, this speed of sound is also close to the speed assumed during B-mode imaging, 1540 m/s, so that little scaling of B-mode images is needed.

The above discussion has considered liver in its unaltered state at 37°C. However, it is possible that temperature and stiffness changes during HIFU ablation will cause localised speed of sound changes that distort the passive maps, in a similar way to thermoacoustic lensing during ultrasound echo strain thermometry [247; 141].

Furthermore, the assumption that a liver placed in a 37°C water bath will have reached a uniform temperature of 37°C after an hour needs to be challenged, as inhomogeneities in tissue structure are likely to result in local variations in temperature during diffusion of heat into the liver.

Attenuation

Unlike in agar, where cavitation emissions travel largely unattenuated in the 5-10 MHz range, attenuation in ox liver is significant – estimated to be 3.0 dB/cm at 5 MHz and 6.6 dB/cm at 10 MHz using results obtained with R Ritchie and E Mylonopoulou, which are consistent with other published research [142].

Because no attempt was made in the present work to quantifiably relate the power of cavitation emissions to focal heating, it was not deemed necessary to correct for attenuation experienced by the emissions as they travel to the array. However, the effect of attenuation is clearly seen on the amplitude of the signal received by the receivers (see Figure 6.7). Should future work make use of the quantitive information that the passive mapping techique provides, such depth-dependent compensation should be applied (see Section 7.2.2 of the Conclusions).

Inhomogeneities

Attenuation in tissue arises from absorption and scattering, the latter caused by tissue inhomogeneities. Scattering poses an additional problem in forming passive maps, since the pressure wave emanating from a cavitating bubble not only attenuates but causes secondary sources. Part of the signal degradation observed in Figure 6.7 is deemed to arise from scattering.

Non-linear propagation

The linear array detects three sources of sound during HIFU exposure: scattering of the HIFU driving frequency, from the linearly propagated portion of the HIFU wave;

scattering of harmonics of the HIFU driving frequency, from non-linear propagation of the HIFU wave; and finally, broadband emissions from cavitation. For array receivers with a uniform frequency response, scattering from the HIFU fundamental would dominate the signal. Thankfully, in this case, the 5-10 MHz array response and 4.6-9.6 MHz bandpass filtering removes most of the HIFU fundamental and has not been observed to appear in the channel data. Unfortunately, harmonics of the 1.06 MHz HIFU driving frequency directly interfere with the recorded signal, since they appear at $\{5.3, 6.36, 7.42, 8.48, 9.54\}$ MHz in the 4.6-9.6 MHz band.

In agar, Section 6.1.2 has shown that even at 4.2 MPa PRFP, the level of harmonics is minimal compared to broadband emissions. Therefore, filtering out the harmonics is unnecessary, and may even degrade the signal, since stable cavitation will also have a harmonic component. In ox liver, however, harmonics dominate in the recorded signal. Figure 6.7 shows the effect of filtering out the harmonics with a comb filter consisting of 0.6 MHz bandpass filters. Since passive maps are created from 20µs segments, a 0.05 MHz bandpass would at first seem sufficient; however, the high ratio of harmonic signal power to broadband power – especially marked when harmonics backscatter from boiling bubbles – makes a wideband filter necessary.

Pressure thresholds for cavitation and lesioning

It has been found with the samples of degassed ox liver that the cavitation threshold is high compared to agar gel, namely 2.7–3.6 MPa PRFP. Furthermore, the threshold for lesioning, as determined by visible blanching, is even higher for shorter exposures of 5 seconds or less. At such high pressures, cavitation nuclei are quickly depleted

and non-linear heating may be the dominant heating mechanism, potentially limiting the role of cavitation mapping for lesioning monitoring. However, the distribution of cavitation nuclei *in vivo* will be different than in degassed tissue, and could in any case be modified with the injection of microbubbles into the bloodstream. Therefore, further experiments will be needed to establish the role of cavitation in tissue.

6.2.2 Comparison of cavitation-based and hyperecho-based monitoring

During the course of the experiments with ox liver, many tissue samples were exposed to HIFU and monitored using hyperecho and cavitation maps (in all, 12 liver samples were used, with a total of 290 exposures). In this section and the next, results obtained from one sample of liver are presented. The data are representative of results for other samples, and encompass a wide range of exposure settings and lesion outcomes.

As described in Section 3.6.2, 6×6 exposures were made in a liver sample. Therefore, to compare B-mode based hyperecho detection with cavitation mapping, a row of 6 exposures with increasing pressure settings (3.6 to 8.0 MPa PRFP) was monitored with B-mode, followed by a row of identical settings monitored passively. In all, three pairs of rows were exposed for durations of 2 s, 5 s, and 10 s respectively.

After all HIFU exposures had finished, the tissue was sectioned through the midplane of the 40 mm thick liver slice, to reveal the past locations of the HIFU focus during exposure, and determine whether lesioning (indicated by blanching) occured. Figure 6.8 shows a photograph of the midplane section, compared with

a figure depicting hyperecho and cavitation detection. The clinician with whom the experiments were conducted, Mr Ritchie, had experience of conducting B-mode monitored HIFU treatments, and was asked to identify which B-mode images showed hyperecho. Hyperecho was also quantified by taking a region of interest around the HIFU focus and noting the decibel change in integrated backscatter before, and on the first frame after HIFU exposure. Similarly, the level of cavitation was quantified by using passive mapping to generate values of broadband source power at the HIFU focus. The mean of these values during HIFU exposure, referenced in decibels to the value before HIFU exposure, was then taken.

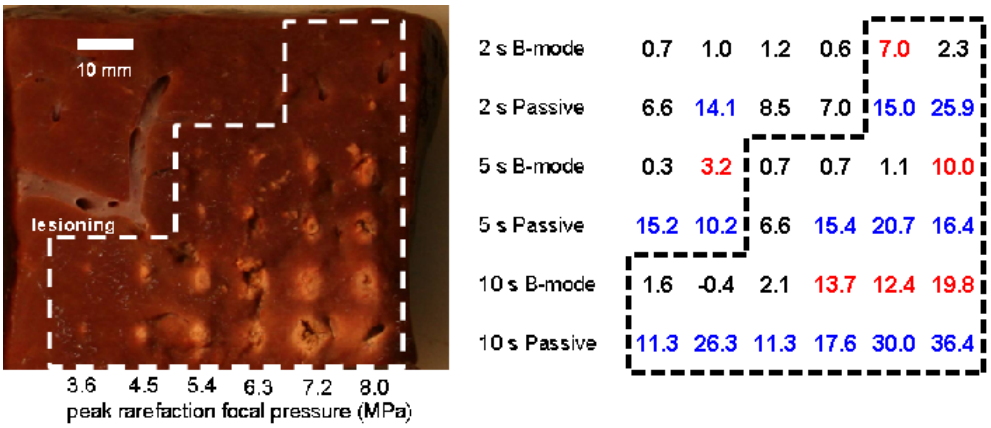

Figure 6.8: Comparison of tissue lesioning with active hyperecho and passive cavitation data. A midplane slice was made at the original location of the HIFU plane to reveal lesions caused at the HIFU focus (left image). As expected, the probability of lesioning increases both with longer exposure durations and higher pressures. In the right image, SNR measures of backscatter and cavitation are shown, whose calculation is described in Section 6.2.2. The existence of hyperecho (shown in red) was determined by a trained clinician, Mr Ritchie, and corresponds to a 3 dB backscatter SNR threshold. Using 10 dB as the threshold for significant cavitation (shown in blue), cavitation is a sensitive predictor of lesioning, and in this sample false positives arise only in the vicinity of the blood vessel visible near the top left of the image.

Figure 6.8 highlights several important observations. As expected, increasing pressure amplitudes and exposure durations caused increased lesioning, and lesioning was fairly repeatable for identical exposure parameters. The existence of hyperecho often indicated overtreatment. In contrast, the cavitation signal to noise ratio was high for all exposure settings shown (prior experiments showed that the cavitation threshold for tissue was in the 2.7–3.6 MPa PRFP range).

By choosing 10 dB as the threshold value for determining lesioning, a much higher prediction sensitivity was obtained than with hyperecho-based prediction. Although this method of prediction also generated some false positives, these only occurred in the vicinity of large blood vessels, which for the *ex vivo* tissue used in this experimental series would have been filled with a static non-physiological mixture of PBS and blood. It is therefore likely that the false positives were generated by cavitation occuring in this mixture, a place where blanching could not have occured. As shown on Figure 6.8, a false positive was also generated by hyperecho detection, which also occured in the vicinity of a large blood vessel. Unfortunately for these experiments, liver tissue is highly vascularised and these results highlight the difficulty in finding a relatively homogeneous sample of liver to use.

Although the presence of cavitation in the vessel may have been due to particles in the buffer solution acting as cavitation nuclei, the result nevertheless highlights the importance of displaying passive maps on top of B-mode images taken while the HIFU is off (much like the practice of overlaying color flow images onto B-mode images) in order to enable informed interpretation of the cavitation signal during treatment monitoring.

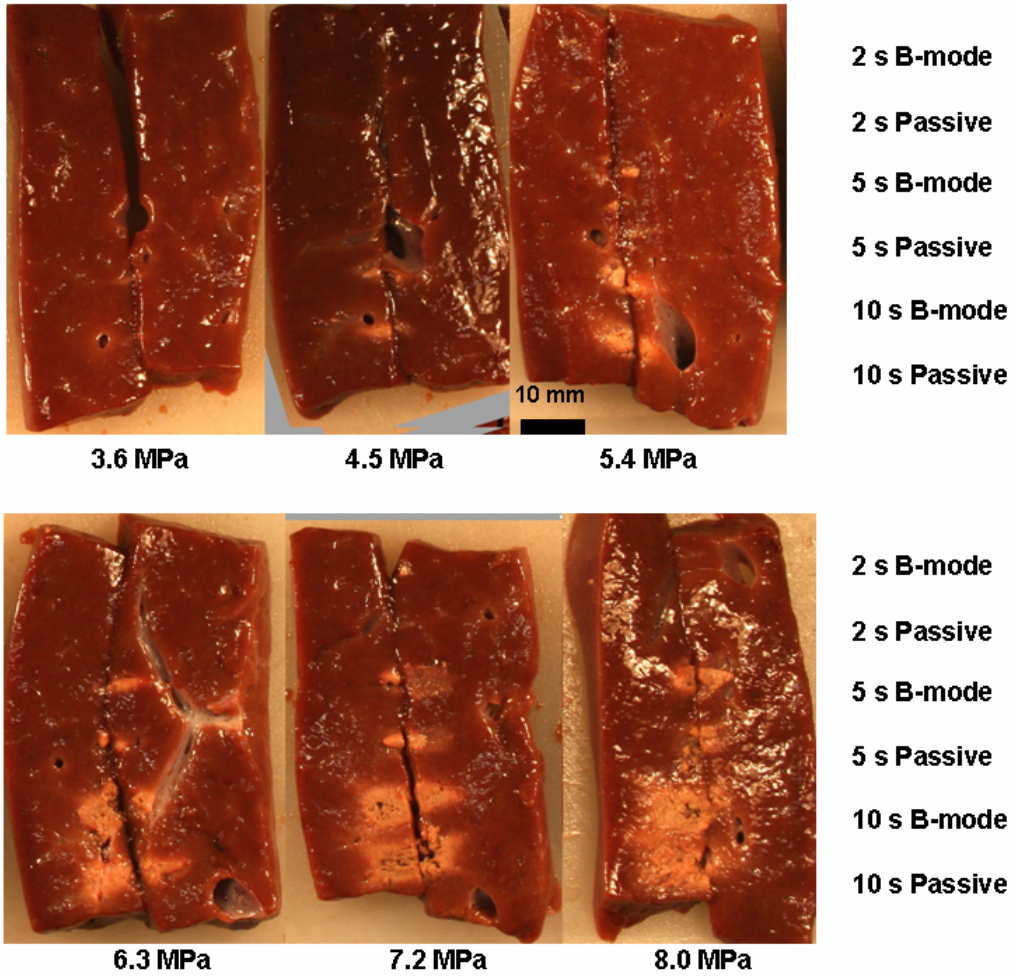

Figure 6.9: Slices of HIFU-exposed tissue showing the axial extent of lesioning for different exposure settings. Blanched tissue forms a volume that separates easily from surrounding tissue, so capturing small lesions in the axial direction is difficult. Nevertheless, the growth of lesions with increased exposure duration and pressure is visible. Cigar-shaped lesions and tadpole-shaped lesions can also be distinguished from each other, with the latter occuring at longer durations and higher pressures.

After slicing the tissue in the midplane and finding the past locations of the HIFU focus, the tissue was cut in strips along the HIFU axis, thereby revealing the axial extent of lesioning. Comparing these strips (Figure 6.9) with the exposures that led to hyperecho (Figure 6.8) shows that the appearance of hyperecho is often linked with tadpole-shaped lesioning. Figure 6.10 shows post-exposure B-mode images and

tissue photographs for three 10 s exposures at increasing HIFU pressures. The lack of sensitivity of hyperecho-based monitoring is again clearly visible.

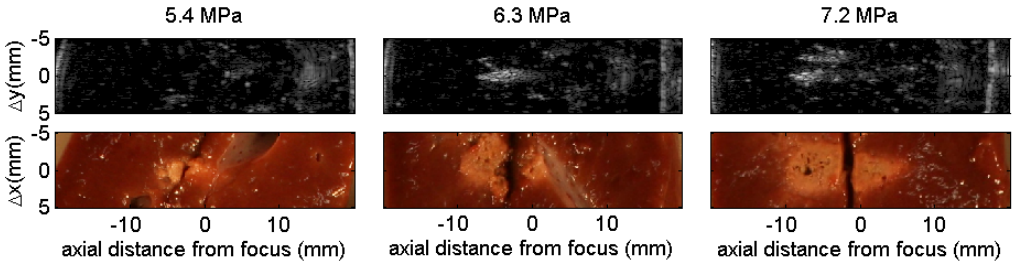

Figure 6.10: Comparison of B-mode images with lesioning for 10 s exposures. Figure 6.9 shows that the 10 s exposures encompass a wide range of lesioning types. In the above sequence of images, the effect of increasing the pressure can be seen on the B-mode images and photographs. Hyperecho does not appear until 6.3 MPa PRFP, when the cigar-shaped lesion starts to be distorted into a tadpole shaped lesion.

6.2.3 Prediction of lesion shape using passive dose maps

As discussed in Section 1.3.3, there are several possible approaches in using passive cavitation maps to predict the shape of lesions. Maps of heating rate obtained from passive cavitation maps could be input into the bioheat transfer equation [99] to predict temperature rise, from which a map of thermal dose could be estimated (as in Section 1.1.3). Alternatively, the decrease in cavitation source power with time, an indicator of elevated temperature and tissue stiffness, could be used to predict lesioning.

As a first attempt to predict cavitation lesions, a relatively simple method was chosen whereby cavitation maps were integrated with time to provide so-called *cavitation dose maps*. These maps, with units of energy, are expected to be proportional to the total energy deposited by cavitation. Although heat diffusion will decrease the probability of lesioning if the same thermal energy is deposited over a longer time, these dose maps are deemed to be a good starting point for future monitoring strategies based on passive mapping.

It would be impractical to show cavitation dose maps obtained for all exposure settings and discuss them at length. Instead, data for three exposure settings are presented – 2 s at 8.0 MPa PRFP, 5 s at 7.2 MPa PRFP, and 10 s at 8.0 MPa PRFP – that are representative of three different regimes of ablation that have been observed during experiments with liver. These regimes are broadly characterised by the shape of lesions they cause – small cigar-shaped, broad cigar-shaped, and distorted tadpole-shaped – but will be discussed in greater detail below.

As mentioned in the previous section, filtering of the channel data was needed

to separate the broadband and harmonic components from each other. Therefore, dose maps are not only provided for the broadband component of the data, which represent the energy deposited by inertial cavitation, but also for the harmonic component, which contains scattering from bulk tissue and, during extreme heating, boiling bubbles. The variation of maximum source power with time is also plotted for each component.

Comparison of passive dose maps with gross pathology

In order to assess the ability of passive dose maps to predict the size of lesions, the tissue was cut along the axis of HIFU exposure to reveal the extent of blanching, which is indicative of thermal lesioning (see Section 3.6.2). Unfortunately, it was experimentally easier to make cuts perpedincular to the array imaging plane. Nevertheless, the photographs still provide a means to check the axial extent of the lesions.

Because the tissue expands on being taken out of the holder, the photographs were scaled so that the distance between the edges was 40 mm (the depth of the tissue holder). Due to tissue deformations and non-uniform tissue compressibility (due to inhomogeneities such as vessels or lesioned tissue), this process of registration may be prone to errors (see the Conclusions on suggestions for future improvements).

2 s exposure at 8.0 MPa PRFP

Figure 6.11 shows the results for the 2 s exposure at 8.0 MPa PRFP. The broadband dose map is well focused and provides good localization in the transverse direction. Surprisingly, however, cavitation is depicted to occur 5 mm more prefocally than

lesioning, which was not observed in the agar experiments described in Section 6.1. In contrast to the broadband dose map, the harmonic dose map is quite diffuse. There are probably two reasons for this: firstly, the non-linearly propagated HIFU wave will be scattered off a relatively large volume; secondly, Chapters 2 and 3 have shown the tendency of narrowband sources to interfere with each other and create image artefacts.

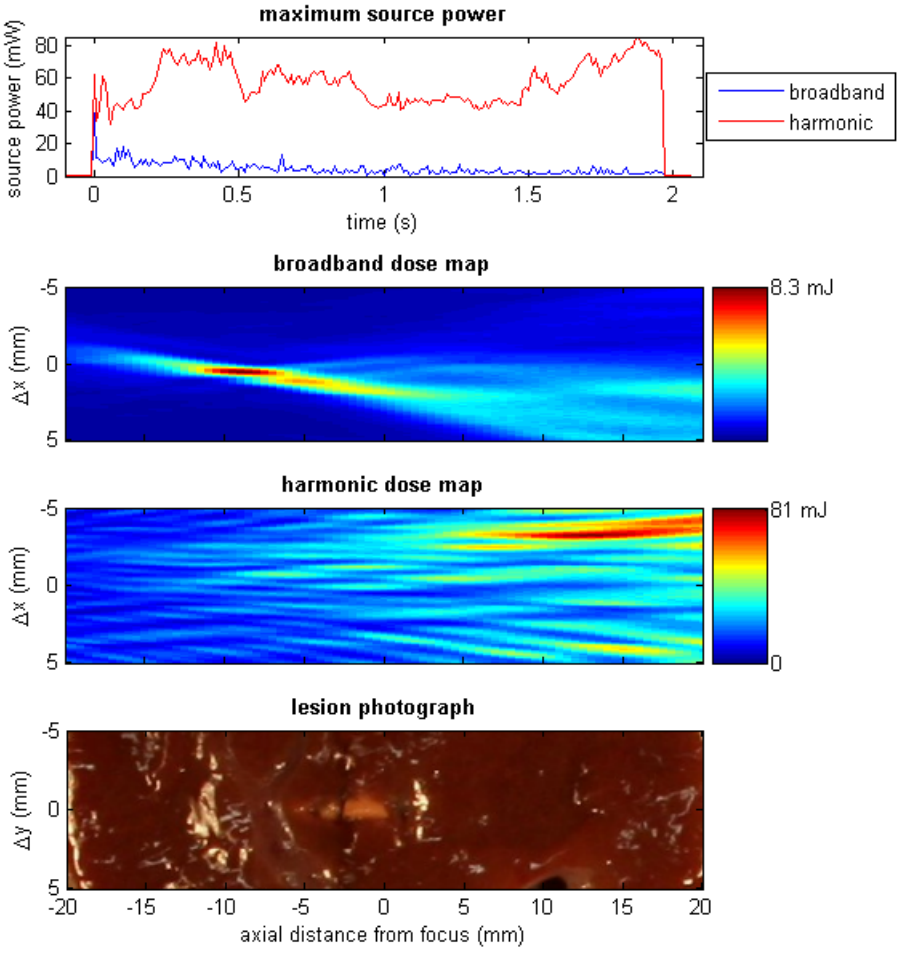

Figure 6.11: Passive dose maps and photograph of tissue exposed to HIFU for 2 s at 8.0 MPa PRFP. The broadband dose map gives good localization of the lesion in the transverse direction but there is a 5 mm prefocal error in the axial estimation. The harmonic dose map is diffuse and non-informative.

5 s exposure at 7.2 MPa PRFP

The results for the 5 s, 7.2 MPa PRFP exposure (Fig. 6.12) are similar in nature to the previously discussed exposure. The broadband dose map is again well focussed, with its focus 5 mm ahead of the centre of the lesion, while the harmonic dose map is again diffuse. It is worth noting, however, that the lesion is now thicker. This is because, for longer exposures, heat has had time to diffuse away from the heat source, and it should therefore not be expected that accurate mapping of the heat source will necessarily overlap with the extent of thermal damage. Hence, cavitation mapping will be most useful as a clinical tool for relatively short exposure durations on the order of 2 s, which are similar to those in current clinical use. Also note the extinction of broadband noise after 1 second of exposure, highlighting the aforementioned need to sustain cavitation in order to ensure it is the dominant source of heating.

10 s exposure at 8.0 MPa PRFP

In the final, 10 s, 8.0 MPa PRFP exposure, several interesting effects are visible (Figure 6.13). For instance, up to 3.2 seconds into HIFU exposure, the level of harmonic and broadband scattering is comparable to the previous two exposures. However, after 3.2 s, an order of magnitude increase in harmonic scattering occurs. This increase is believed to be due to the appearance of boiling bubbles [78], which in turn are associated with tadpole-shaped lesions and overtreatment [76]. This is confirmed by the tadpole-shaped lesion shown in Figure 6.13. In fact, the gross pathology of the liver tissue after sectioning showed an excellent correspondence

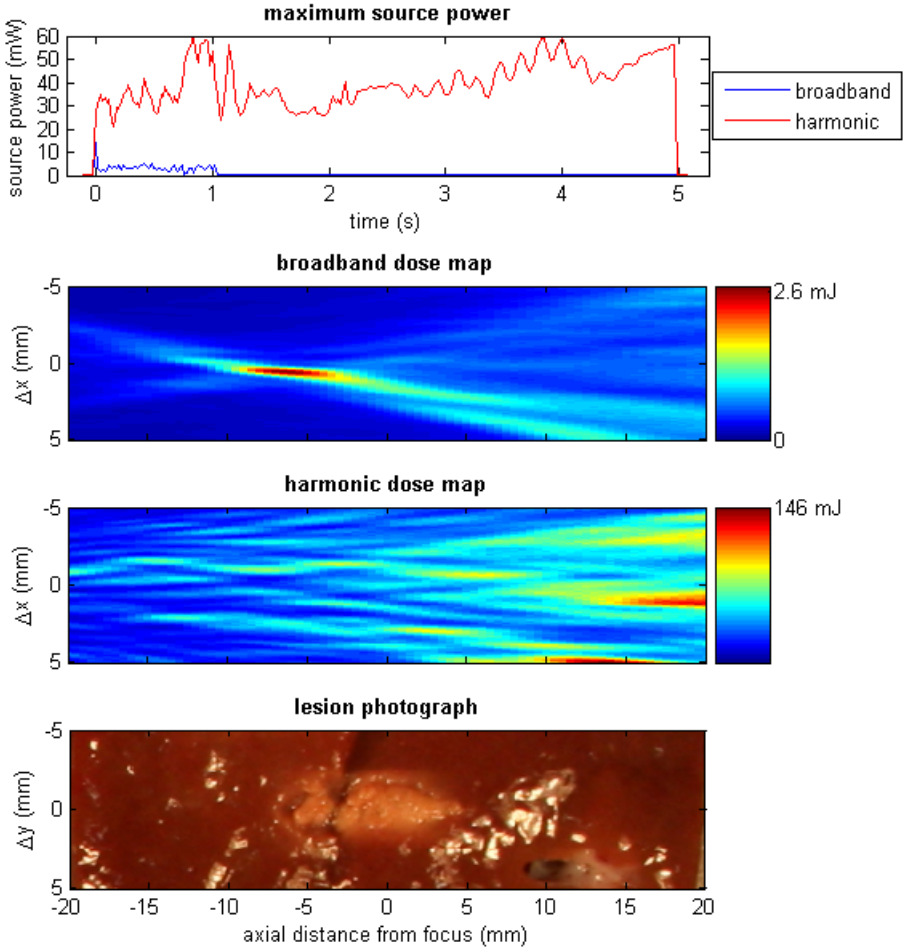

Figure 6.12: Passive dose maps and photograph of tissue exposed to HIFU for 5 s at 7.2 MPa PRFP. Like the results of the previous exposure (Fig. 6.11), the broadband dose map predicts the lesion to be 5 mm ahead of where it is. The harmonic dose map is again uninformative.

between high harmonic backscatter and tadpole-shaped lesioning for all the HIFU exposures. Since this elevated scattering develops a few seconds into exposure, monitoring the level of harmonics could also be a possible method of monitoring treatment *during* HIFU exposure.

Another interesting feature of Figure 6.13 is that in contrast with the earlier harmonic dose maps presented, the current one shows a well-focussed region. It has been predicted in Section 2.3.4 and confirmed in Section 4.2.1 that while a single narrowband source can be imaged well, several narrowband sources tend to interfere with each other. Therefore, it is highly likely that a well-focussed harmonic map arises from a single boiling bubble.

Even before the level of harmonic backscatter shows a marked increase at around 3.2 s, broadband emissions from inertial cavitation "shut down" at around 2.6 s. This could provide an early warning that boiling is about to occur.

Because of strong harmonic backscatter, which will cause signal leakage to the broadband dose map even before 3.2 s, it is useful to compare passive maps when either the broadband emissions or harmonic emissions are comparatively strong. Figure 6.14 shows passive broadband and harmonic maps at three time instances during HIFU exposure. As illustrated by the figure, inertial cavitation tends to appear pre-focally. Also, for the maps at 3.4 s, there seems to be significant backscatter from a boiling bubble in the HIFU focus, which is mapped well using harmonic mapping (some of the signal leaks into the passive map, which shows much lower powers). The central harmonic map also illustrated a general trend observed during all exposures: when the level of harmonic backscatter was high, the harmonic map

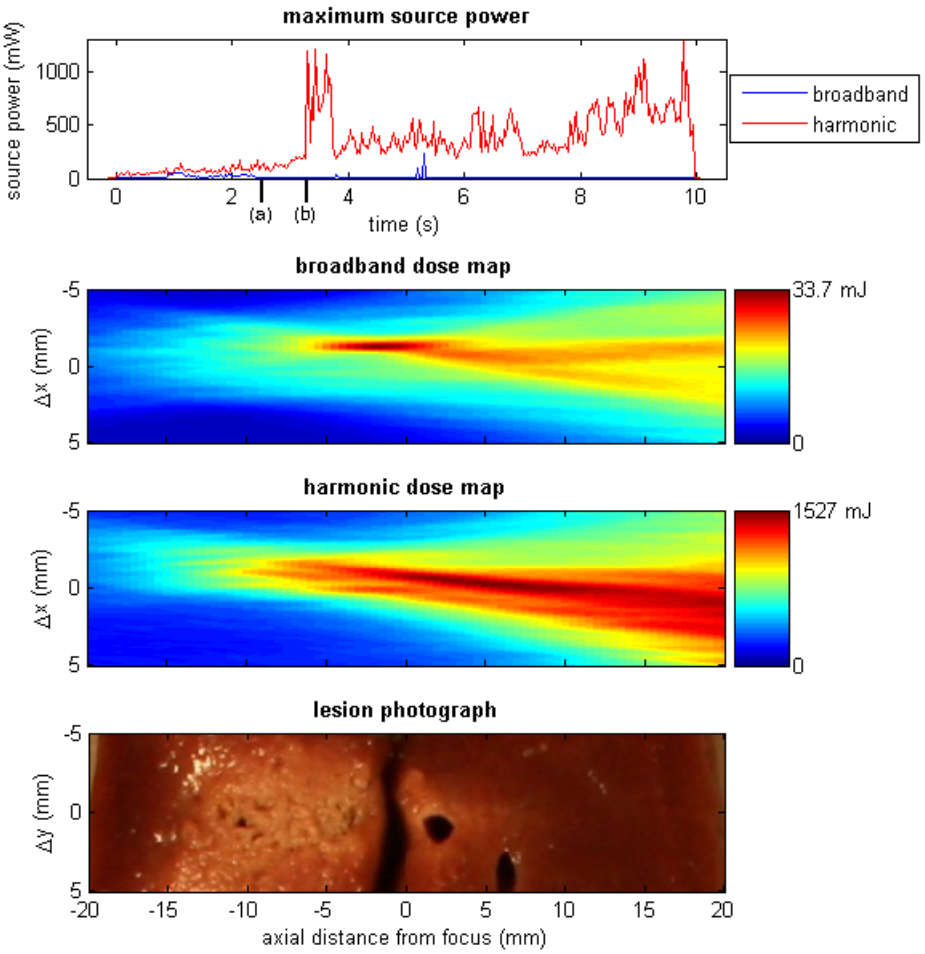

Figure 6.13: Passive dose maps and photograph of tissue exposed to HIFU for 10 s at 8.0 MPa PRFP. (a) The level of broadband emissions "shuts down" at 2.6 s into exposure. (b) In contrast to the previous exposures (Figs. 6.11,6.12), the level of harmonic backscatter increases considerably at 3.2 s into the exposure, causing a harmonic dose map that is somewhat focussed. The increased harmonic backscatter is assumed to arise from boiling bubbles, which cause the tadpole shaped lesion shown in the photograph. Because of leakage from the strong harmonic signal, the broadband dose map computed for the entire exposure had the same shape as the harmonic dose map. Therefore, the broadband dose map shown was only computed for the first 3.2 s.

tended to be well focussed. As mentioned previously, this is thought to be because scattering from one bubble dominates.

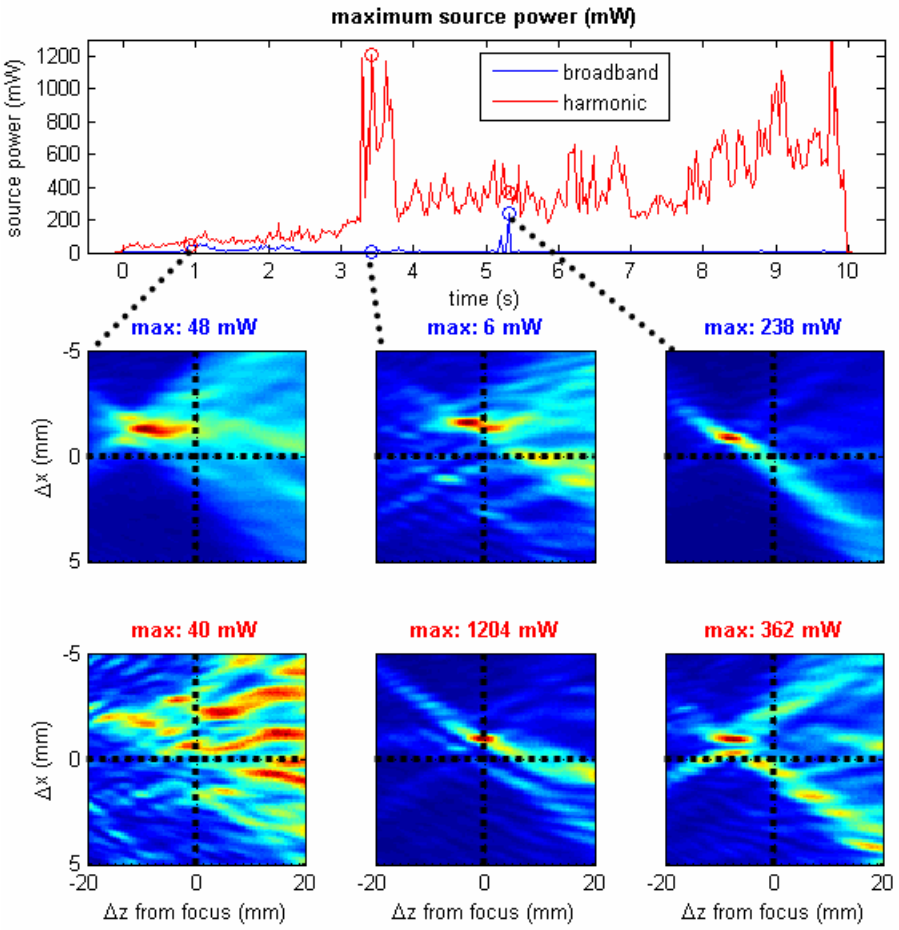

Figure 6.14: Passive maps of tissue exposed to HIFU for 10 s at 8.0 MPa PRFP.

Summary of lesion shape prediction

Before generating passive maps, the array signal was split into a broadband component indicative of inertial cavitation and a harmonic component indicative of backscatter (either of the non-linearly propagated HIFU wave, or non-linear backscatter by bubbles). The resulting broadband and harmonic passive maps yielded some very interesting results, summarised below.

Broadband maps integrated over the duration of exposure were well focussed in the transverse direction and gave a good indication of the size of the lesions. There was a trend, however, for inertial cavitation to be localised approximately 5 mm in front of the focus, which did not occur in the context of experiments in agar. The reason for this is still under investigation. It could be that tissue stiffening during ablation does not permit inertial cavitation to occur, however further work is needed to exclude the possibility of experimental errors, such as registration errors between passive maps and gross pathology. The relative roles that inertial cavitation and non-linear propagation play in tissue ablation also need to be investigated, as do HIFU protocols that enhance the former (see Section 7.2.2 of the Conclusions).

For longer exposure durations, the level of harmonic backscatter can suddenly increase by an order of magnitude. Since this increase is a good indicator of boiling, and thus pre-focal, tadpole-shaped lesioning, HIFU exposure could be terminated when a sudden increase is noted, in order to avoid overtreatment. Even before the increase in harmonic backscatter, broadband emissions are observed to "shut down", providing an early warning that boiling is about to occur (see Figure 6.14). This would be a much more sensitive monitoring method than the currently used B-mode

hyperecho, which relies on detecting stabilised, and often boiling bubbles after HIFU exposure.

The shape of harmonic maps is also worth mentioning. At lower levels of harmonic backscatter, the maps are diffusive and uninformative. However, at higher levels, the maps are often well focussed and at the HIFU focus. It is argued that this is due to a large, boiling bubble, dominating harmonic backscatter, since previous results (Sections 2.3.4,4.2.1) have shown that passive mapping can give reliably localization for single harmonic sources.

6.3 Summary

This chapter has shown passive maps obtained with the array placed through a rectangular opening in the HIFU transducer. HIFU exposures in agar demonstrate, for the first time, that passive mapping can be successfully used to map both continuous and disjoint cavitation regions during HIFU exposure, without the need to switch the HIFU transducer off. Cavitation was also shown to be the dominant heating mechanism in agar gel for pressures up to 4.2 MPa PRFP, resulting in a strong correlation between values of source power obtained using passive maps and temperature elevation at the HIFU focus.

Samples of ox liver were also insonated with HIFU for various durations and acoustic intensities. Hyperecho-based monitoring and passive mapping were compared in their ability to predict the existence and shape of lesioning. Cavitation detection was shown to be a more sensitive predictor of lesioning than the apperance of hyperecho, which is the current ultrasound-based monitoring method during

HIFU treatments. Furthermore, apart from a 5 mm prefocal axial shift the origin of which is still being investigated, passive maps of the broadband signal gave good prediction of the lesions, while harmonic maps could be used to indicate tissue boiling and overtreatment.

Throughout the HIFU exposures in *ex vivo* liver, it was observed that the level of harmonic backscatter was much higher than the level of broadband emissions, and careful filtering needed to be applied to recover the latter. This could be a reason why inertial cavitation, and the broadband emissions it produces, are often overlooked or not detected when detection systems that do not have a dynamic range appropriate for these low signal levels are utilized. Such systems have often been used in previously published research to draw conclusions as to the presence or absence of inertial cavitation during therapeutic ultrasound processes.

Since inertial cavitation is observed to "shut down" prior to the increase in harmonic backscatter associated with boiling, detecting broadband emissions could be an important method of monitoring HIFU treatment. Therefore, further research should be carried out *in vivo* (where gas concentrations are expected to differ from *ex vivo* experiments) to investigate the role of inertial cavitation during HIFU treatment, as well as the applicability of passive mapping to ablative HIFU treatment monitoring. As with conventional B-mode imaging, tissue layers of different speeds of sound (most markedly fat) are expected to cause localisation errors *in vivo*. However it is hoped that the presence of speed of sound estimators on B-mode imagers (as already implemented on the machine used in this work [248]) can help correct for such errors.

Chapter 7

Conclusions

7.1 Summary of achievements

The primary aim of the present work was to demonstrate the feasibility of passive cavitation mapping as a monitoring tool during HIFU treatment. However, the use of a linear array of 64 piezoelectric elements recording acoustic emissions in parallel has also shown other applications, which are re-iterated below.

In Chapter 2, various passive source reconstruction algorithms were reviewed, and a variant of passive beamforming called Time Exposure Acoustics (TEA) [184] was selected for the present application. TEA is simple enough to act as a proof of concept without excessive demands on computational time and yet general enough to map arbitrary source distributions. However, future work may incorporate some of the more advanced reconstruction techniques such as deconvolution.

In the last part of Chapter 2, theory and simulations were used to evaluate the resolution performance of TEA as applied to a linear array of aperture 38 mm.

It was found that the axial and transverse resolutions were 5 mm and 0.5 mm, respectively, for a source 73 mm from the array. (73 mm is the distance of the HIFU focus – were cavitation is expected to happen – from the array when the linear array is placed next to a rectangular opening ot the HIFU transducer, in a clinically applicable setup.) It was further found that broadband sources such as inertially cavitating bubbles were less likely to interfere with each other in the passive maps than narrowband sources, as predicted by Norton *et al.* [184]. Lastly, deconvolution was found to have a limited effect on improving the axial resolution of passive maps, so such improvements were left for future work.

Chapter 3 began with describing the experimental methods common to all experiments, including the channel data acquisition and methods for subsequent passive map generation. It then described the setup and methods particular to each of the three sets of experiments carried out in this work, whose results were given in the subsequent three chapters.

In Chapter 4, narrowband and broadband sources were generated by scattering ultrasound waves off a wire, serving the dual purpose of calibrating the linear array to generate quantitative passive maps, and validating the passive mapping method using controllable source distributions. The absolute and spatial calibrations of the linear array allowed passive mapping to give quantiative maps of source power (in Watts). It was highlighted that the powers obtained did not indicate the power radiated by the sources themselves, but the power transmitted in the 5–10 MHz range that was not absorbed by the propagating medium, whether agar gel or ox liver. In the final part of Chapter 4, the passive maps were used to experimentally confirm

the earlier finding that broadband sources are more robust to source interference than narrowband sources.

Chapter 5 showed passive maps of cavitation in agar, generated with the array placed transversely to the HIFU axis, at a distance of 36 mm. The resulting passive maps were of such high quality that individual cavitating bubbles could be resolved. Indeed, the signals received by each array element, which showed a mixture of emissions from different bubbles, could be separated into the emissions arising from individual bubbles. Correcting for the propagation of the HIFU wave, it was shown that near the cavitation threshold, bubbles often collapse due to the same HIFU pulse wavefront. The passive maps also showed good correlation of bubbles using a single element active cavitation detector (ACD). Nevertheless, the ACD traces, taken at a rate of 2 kHz after HIFU was switched off, showed dissolution of bubbles at pressure amplitudes below 3 MPa peak rarefactional focal pressure (PRFP), supporting the assertion that a B-mode imager will not be able to detect some previously cavitating bubbles, even when the imager is synchronised with HIFU.

Finally, in Chapter 6, the clinically applicable setup of the array placed coaxially with the HIFU transducer was used. Passive mapping correctly identified increasingly large areas of cavitiation in agar as the HIFU excitation amplitude was increased, as well as disjoint regions of cavitation when the cavitation threshold was intentionally lowered in discrete regions. Inertial cavitation was also shown to be the dominant source of heating in agar. The result was shown by the repeated HIFU exposure, with simultaneous thermometry, of a single location at pressures above the cavitation threshold, until the local cavitation nuclei became depleted.

Due to the inhomogeneity and nonlinearity of liver, results were more difficult to interpret in samples of ox liver than in agar gel. The channel data needed to be decomposed into harmonic and broadband components before mapping to separate the effects of non-linear propagation and inertial cavitation. Inertial cavitation was a more sensitive detector of lesioning than hyperecho, the latter correlating with tadpole-shaped lesioning that is associated with boiling and therefore overtreatment.

Perhaps the most important conclusion of the present work is that, with appropriately sensitive cavitation detection in place, significant levels of inertial cavitation were detected whenever lesioning was observed, whilst hyperecho was not. This strongly suggests that passive cavitation mapping could provide a significant advance in ultrasound-based monitoring of HIFU therapies, compared to currently available pulse-echo techniques, not only because it can be applied during HIFU exposure, but also because of increased sensitivity and signal-to-noise ratio.

To predict lesions, the broadband and harmonic passive maps were integrated to give dose maps. The broadband dose maps produced by passive cavitation mapping gave very good transverse localisation of lesions, and harmonic dose maps returned some spatial information if boiling was reached, suggesting that backscatter was dominated by a few echogenic bubbles (since less interference arises when there are fewer narrowband sources). However, cavitation maps in tissue showed a repeatable 5 mm axial bias, which was not observed during previous experiments in agar. Identifying whether inertial cavitation does indeed occur slightly prefocally during HIFU exposure of tissue, or whether this discrepancy is the result of registration errors between passive maps and tissue photographs, will be investigated.

Despite the need for further research and evaluation, it is believed that with use of an appropriately designed cavitation detection array, passive mapping will represent a major advance in ultrasound-guided HIFU therapy. Not only can it be utilized in real time during HIFU exposure, without the need to turn the therapeutic ultrasound field off, but it has also been shown in the context of the present work to provide a strong indicator of successful lesioning and high signal-to-noise compared to conventional B-mode ultrasound techniques.

7.2 Suggestions for future work

7.2.1 High-resolution passive cavitation mapping and source reconstruction

The ability to reconstruct emissions from several, simultaneously cavitating bubbles opens up a new way of investigating multi-bubble cavitation dynamics, an important but somewhat neglected subject [58]. Passive source reconstruction has some important advantages over high-speed photography: at relatively low cost, the behaviour of several bubbles can be studied at megahertz frame rates over the course of hundreds of ultrasound cycles, even in an optically opaque medium such as tissue. In future work, the source strengths would be converted to the radial movement of the bubbles using the proportional relationship between the second temporal derivative of bubble volume and radiated pressure [49].

The results could also be compared with other indicators of cavitation activity in a transparent medium: in addition to high-speed photography, chemical indica-

tors such as BSA (thermal dose), luminol (sonochemiluminescence), methylene blue (dissolved oxygen), cobalt (II) chloride (temperature), potassium iodide (free radical generation), could also be used [249; 250; 251; 252; 253].

7.2.2 Cavitation monitoring during ultrasound therapy

This work has shown the feasibility of passive cavitation monitoring during ablative HIFU treatment. Passive cavitation maps gave accurate indications of the distribution of cavitation in agar tissue mimicking gel. However, more work is needed to establish how cavitation can be related to lesioning, and the source of the 5 mm axial difference noticed between lesions and cavitation maps. Furthermore, the current axial resolution of the system (5 mm) should be improved, and the method of generating passive maps could be made faster. To this end, several suggestions for future work are given below.

In order to predict regions of tissue damage, a simple measure of "cavitation dose" was used, whereby cavitation maps were integrated with time. Although the results gave reasonable predictions, cavitation merely provides a heat source and the effect of heat diffusion should also be incorporated into the formulation to be able to predict the broadening of lesions with longer HIFU exposures.

To provide a direct estimate of the heat being deposited, the scaling factor between the received source power and the absorbed source power should be measured (See Section 2.1.5 and [56]). One possible solution would be to compensate for attenuation by a pulse-echo measurement on a reference scatterer such as a contrast agent microbubble. This is similar to the quantification of power Doppler signals

by normalisation of the signal to a vessel with full blood blow [254; 255]. A second possible solution is to ramp the HIFU intensity until a contrast agent microbubble of a known cavitation threshold and emission power inertially cavitates. In both cases, however, the absorption coefficient of the treated tissue would also need to be known in order to estimate the local heating rate.

From the local heating rate, temperature maps could also be produced, but this would only be possible for short exposures and away from major blood vessels where conduction and convection can be neglected. Alternatively, the correspondence between cavitation shutting down and lesion formation could also be part of a monitoring strategy, and should also be investigated further.

Similarly to the flow channels in agar, samples of ox liver should be injected with microbubbles at known locations, and the cavitation maps compared with the sites of injection. This could help establish whether the axial difference between cavitation maps and lesioning is real (lesioned tissue may not support cavitation and so cavitation may happen at the prefocal tip of the lesion), or whether it arises from image distortion, such as speed of sound errors.

The role of cavitation during *in vivo* HIFU exposures is the source of some contention among researchers, with some maintaining that without the introduction of microbubbles into tissue, heating due to non-linear propagation is a greater contributor to lesioning than inertial cavitation. In the *ex vivo* experiments of Chapter 6, cavitation often diminished within a few seconds, increasing the role of other heating mechanisms in the lesioning that was observed. This supports previous *ex vivo* observations that, using elevated hydrostatic pressures to suppress cavitation,

lesioning can occur without inertial cavitation [102]. Lowering the duty cycle [20], or using a closed-loop control system [256], can help maintain cavitation, ensuring that cavitation-enhanced heating is maintained throughout the exposure and thus making cavitation mapping a more reliable treatment marker for longer exposures. Tests should be carried out *in vivo* to determine the extent of cavitation with or without microbubbles and how the enhancement or suppression of cavitation using different HIFU insonation parameters [257] affects treatment speed and efficacy.

As regards the passive maps themselves, it is clear that spatial resolution should be improved from the present 5 mm axial resolution. Although Chapter 2 has shown some alternatives to Time Exposure Acoustics, the availability of better data is always a better solution to improving image reconstruction than applying complex inversion algorithms that are invariably sensitive to noise.

With passive beamforming, image resolution is proportional to the square of $f_{\#}$, that is, the ratio of source distance to array aperture. In the present work, a 38 mm aperture array was 10 mm behind the surface of a HIFU transducer with a 63 mm focus (see Figure 3.3), giving an $f_{\#}$ of $73/38 \approx 1.9$. Recently, a 55 mm aperture linear array was made available for the ultrasound system used in this work. By constructing a 63 mm focus HIFU transducer that can accommodate such an array, the axial resolution of passive mapping could be reduced to 1.8 mm, though grating lobes may start to appear due to the large interelemental spacing.

The ultrasound system used in the present work was ideal for recording channel data and analysing it afterwards in Matlab. However, if many tests need to be carried out on an existing passive mapping algorithm, it would be simpler to incorporate the

algorithm into the operating system of the ultrasound engine. Given the software-based architecture of the z.one system, this incorporation is a relatively easy task and in fact has been done for other ultrasound research groups.

Finally, the passive cavitation mapping method detailed in this thesis is not limited to HIFU ablation: any ultrasound therapy where cavitation may have an important role could benefit. For instance, research in the laboratory has shown promise that cavitation mapping could identify when vasculature has been penetrated by microbubbles. Hence, cavitation mapping could be used to monitor cavitation-mediated drug delivery.

Appendix A

Channel Data Acquisition on a Commercial Ultrasound System

A.1 Setting imaging parameters via communication with the ultrasound scan engine

As the z.one ultrasound system was designed for both medical professionals and researchers, the system has to ensure ease of use and robustness on the one hand and flexibility on the other. Accordingly, there are two communication interfaces with the scan engine, a graphical user interface (GUI) and a serial interface based on the RS-232 standard. While the GUI provides an intuitive way to capture, save, and review B-mode images (as well as M-mode and Doppler modes), the serial interface allows precise control over imaging parameters, as well as the ability to switch to the so-called research mode where 64 channels of pre-beamformed data can be saved.

With the supplied proprietary USB to DE-9 (9-pin serial) dongle, any computer

with terminal software and a standard DE-9 serial port (or USB port with appropriate adapter) can communicate with the scan engine. In addition to free terminal emulators such as PuTTY, Tera Term, and RealTerm, serial communication can also be automated using Matlab (Mathworks, Natick, MA) and LabView (National Instruments, Austin, TX).

In contrast to conventional B-mode imaging, where minimal setting up is required before the desired images can be captured, the acquisition of channel data for passive beamforming needs a sequence of commands using the serial interface. Many of the settings are best explained in the next subsection, where the path the received data takes from the linear array to being stored is considered. For now, some important functionalities are highlighted below.

Change imaging status between live/frozen

Ultrasound imaging can either be *live* or *frozen*. During *live* mode, the system is generating images or *frames* at the specified frame rate and displaying them on the screen in real-time, while in *frozen* mode the images stored in a buffer can be reviewed. The buffer is erased every time an image parameter changes or the imager goes *live*. Upon erasure, new frames are added to the buffer until it fills, at which point frames are deleted on a first-in first-out basis.

Before making any imaging parameter changes, it is necessary to set imaging to *live*. Furthermore, due to finite buffer size it is important to ensure that images are available for the entire duration of interest, which can be done by choosing the correct imaging modality, depth, and frame rate, as specified below.

Change imaging mode

Both for conventional B-mode images and for the generation of passive maps, the imaging mode needs to be set nominally to B-mode. In the case of the former, images are created from the combination of several transmit zones [258] (in contrast to other ultrasound systems, where a B-mode image is created from stacking A-lines together [259; 260]). For optimum image quality, different zones will use different sets of 64 elements on which to transmit and receive. In contrast, to have access to *channel data* – data from the 64 elements prior to beamforming – the imager needs to be set to single zone mode [258].

Regardless of zone mode, within B-mode imaging there are several transmission modes that influence the data that will be received, even if transmission is turned off, as in the case of passive mapping. Specifically, if imaging is in *tissue harmonic mode*, data will be received at the first harmonic of the transmitted frequency, while *compound mode* will combine data from two sets of transmissions at different frequencies. In *compound harmonic mode*, one transmission occurs and data is received from the fundamental and first harmonic of the transmitted frequency.

For passive mapping, all the above specialised modes need to be turned off, so as to avoid complications from specialised frequency filtering and also to reduce the data load of each frame and thereby maximise the number of frames that can be stored in the buffer.

Change imaging depth (channel recording duration)

When images are generated for greater depths, the time required for the pulse to reach the scatterer and for the echo to return increases. In other words, changing the imaging depth changes the time for which data from the 64 elements is recorded. This determines the integration time T available for passive mapping (2.8), with greater T leading to better estimates. However, reducing the recording time also raises the maximum frame rate available, as well as the number of frames that can be stored in the buffer.

For the problem being addressed in the present work, long recording lengths of typically 140 µs (10 cm imaging depth) were chosen. This was in order to observe cavitation dynamics and to ensure an adequate time window for frequency filtering. The long recording length also ensured a sufficient integration time T, although it was later observed that integration times of 20 µs were sufficient.

In passive mapping, when the recording length is chosen through the selection of imaging depth, the recording length provided by the scan engine will be longer than the time taken for sound to travel the imaging depth twice. This accounts for: the finite pulse duration (the scan engine assumes pulses are transmitted); the time taken to pass through the matching layer; and the longer propagation path from the edges of the aperture. In all, the recording length is generally longer by ~ 10 µs. Similarly, the maximum available integration time T will be less than the recording time, limited by the difference in propagation distances to different array elements at the shallowest image depth. This, coupled with interference from leaked transmit pulses at the matching layer, decreases T by ~ 30 µs.

Set frame rate

Conventional B-mode images are typically limited to 15-20 Hz frame rates, depending on the imaging parameters. While this is sufficient for diagnostic use, cavitation dynamics can change over tens of milliseconds, which makes higher frame rates desirable. Thankfully, with the single-zone mode that is employed in passive mapping, even kHz frame rates are possible, although this comes at the cost of decreased recording time for each frame and recording duration overall. For this reason, frame rates of 30-200 Hz were used in the passive mapping experiments.

Turn transmission on/off

In order to have interference-free passive source maps from externally generated sources, it is necessary to turn off pulse transmission from the ulrasound system. In laboratory experiments, it was in fact possible to leave pulse transmission on as there was an initial period of time when the pulse was travelling through water and had not yet reached the sample, when no echoes were expected. This time period could be used to form the passive map. However, in a HIFU treatment, the path from the array to the surface of the skin could be very short, so pulse transmission would need to be turned off. To have the benefit of both the active and passive imaging modalities, a future implementation could have rapid switching between the two.

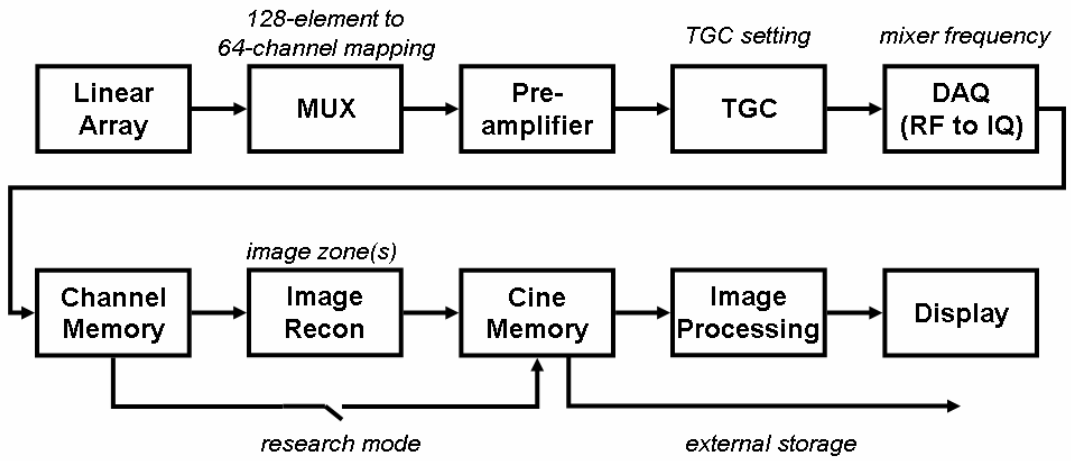

Figure A.1: Receive data path from linear array to data storage. Text in italics refers to imaging parameters that can be changed, or commands that can be executed, that are relevant to the adjacent stage of data processing.

A.2 Data acquisition path

The path taken by the received data before being stored is now reviewed, with a discussion of any relevant settings that need to be made along the way for passive mapping. Figure A.1, based on Figure 1 in [258], shows the path that the received signal takes from the linear array. While reading this subsection, the reader is continually referred to this figure.

The linear array has 128 elements, 64 of which can be accessed at any one time, using a multiplexer. Since imaging resolution, especially in the axial direction, is heavily dependent on the aperture (2.65,2.76), it is highly desirable for elements to span the entire aperture. Every channel $ch \in \{0 \dots 63\}$ could be connected to one of two elements $i \in \{0 \dots 127\}$, namely $i = ch$ or $i = ch + 64$. In the end, a semi-regular aperture was chosen

$$i \in \{2, 4, \ldots, 64, 65, \ldots, 127\} \tag{A.1}$$

although a randomly generated aperture (that also spanned the 38 mm aperture) also gave similar simulated passive maps.

Upon passing through the multiplexer, each of the 64 signals is pre-amplified to ensure a high signal to noise ratio (SNR) before propagating through the micro-coaxial cable. The signal then undergoes time-gain compensation (TGC). This is typically a time-varying amplification that is used to compensate for pulses returning weaker from greater depths due to two-way attenuation. In the passive mapping case, however, a signal received at a certain time could have emanated from any depth, so it is preferred to have a constant TGC and to perform attenuation correction in the passive mapping algorithm itself. A constant TGC of 40dB was found to give good SNR while preventing signal saturation.

After application of TGC, most ultrasound scan engines to date would perform beamforming on the analogue signal prior to digitization. This would circumvent expensive parallel digitization. Thankfully, in the case of the z.one system, the signals are digitized prior to beamforming, providing access to pre-beamformed data. The digitization is initially done at 50 MHz and 16-bit depth [258], however the storage requirements of this are substantial.

To save storage space, a 5 MHz band

$$[f_0 - 2.5, f_0 + 2.5] \text{ MHz}$$

is chosen for storage. The out of band signal is filtered out and the remaining

signal taken down to base-band (demodulated by f_0). Given the Nyquist criterion, the resulting signal can then be sampled at 5 MHz, with a substantial storage saving. Such a scheme is called IQ-demodulation [239], with the resulting data called IQ (in-phase/quadrature data). The naming derives from treating the signal as a modulated version of a carrier or mixer frequency f_0, with the signal decomposed into the amplitude variations of an "in-phase" sinusoid of frequency f_0 and its "quadrature" (90° phase-shifted) counterpart.

IQ data compression has the effect that only a 5 MHz band of the data is made available, however the scan engine allows some control over what this band is. Specifically, the mixer frequency f_0 can be any frequency $50/n,\ n \in \{5 \dots 9\}$. Since the linear array has a 5-10 MHz response, the closest frequency band to this was attained when choosing $n = 7$, with the frequency band being approximately 4.6-9.6 MHz. Since higher frequencies improve imaging resolution (2.65,2.76), it would be tempting to choose a higher frequency band. However, both the limited response of the array at higher frequencies, as well as higher attenuation at higher frequencies, would cause significant losses in SNR that are expected to outweigh any modest improvements in resolution.

The IQ data is now stored in channel memory. For multiple-zone imaging, several channel memory blocks can be used to reconstruct an image, which is then stored in the cine buffer, and can be reviewed on a display and transferred to a USB storage device using a serial interface command. Alternatively, with single-zone imaging and the research mode on, the channel data is transferred to the cine buffer at the specified frame rate, and by freezing imaging, the buffer can likewise be transferred

to a USB storage device.

Before discussing the generation of passive source maps, it is worth clarifying the three types of data that can be stored from the scan engine to a USB storage device.

1. VGA (640×480 pixels) "screen grabs" of the external display for each stored frame. In other words, grayscale images in bitmap form are saved, in the format that one would see them on the screen. The data shown in these frames are true B-mode – brightness-mode – images that have had all the image reconstruction steps done on them, including envelope detection and downsampling to fit the 640×480 screen.

2. Post-beamformed IQ data, which contains more information than the first format, since the IQ data can be remodulated offline to 50 MHz sampling and the data can give information about signal frequency content. In the case of passive mapping, however, the dynamic receive beamforming of the scan engine distorts the frequency content of sources.

3. Pre-beamformed channel data, obtained using single-zone imaging and the research mode of the scan engine enabled.

All three data formats can be copied to a USB storage device using the command

`cine dump` *start_frame end_frame format*

where *format* has a value 1–3 corresponding to one of the above formats.

A.3 Pre-processing of channel data in Matlab

Any block of frames stored in channel data format using the `cine dump` command above is saved to a file that can be converted, using a proprietary program relying on the *Matlab Component Runtime*, to a Matlab data file. The data file, besides containing information about the linear array used to capture the data and some imaging parameters, contains the channel IQ data sampled at 5 MHz in a 4-D matrix, with the following dimensions:

[*frame#, transmit#, channel#, sample#*]

The experiments in this work typically captured 400 frames, with one proxy transmit per frame (as transmission had in fact been turned off), and 139.4 µs recordings for each frame, with a resulting matrix size of $400 \times 1 \times 64 \times 697$.

In order to apply the passive beamforming algorithm, each frame of IQ data needs to be remodulated to RF. This is done using a (corrected) script supplied by Zonare, whereby the IQ data is resampled to 50 MHz using cubic interpolation and then remodulated from baseband to the central frequency of $50/7 \approx 7.1$ MHz.

Bibliography

[1] A. Szent-Györgyi. Chemical and biological effects of ultrasonic radiation. *Nature*, 131:278, 1933.

[2] F. W. Kremkau. Cancer therapy with ultrasound: a historical review. *Journal of Clinical Ultrasound*, 7:287–300, 1979.

[3] C. C. Coussios and R. A. Roy. Applications of acoustics and cavitation to noninvasive therapy and drug delivery. *Annual Review of Fluid Mechanics*, 40:395–420, 2008.

[4] E. A. Brujan, T. Ikeda, and Y. Matsumoto. Jet formation and shock wave emission during collapse of ultrasound-induced cavitation bubbles and their role in the therapeutic applications of high-intensity focused ultrasound. *Physics in Medicine and Biology*, 50(20):4797, 2005.

[5] R. Cobbold. *Foundations of biomedical ultrasound*. Oxford University Press, 2006.

[6] C. R. Hill, J. C. Bamber, and G. R. ter Haar. *Physical Principles of Medical Ultrasonics*. John Wiley and Sons, Chichester, 2004.

[7] T. G. Muir and E. L. Carstensen. Prediction of nonlinear acoustic effects at biomedical frequencies and intensities. *Ultrasound in Medicine & Biology*, 6(4):345–357, 1980.

[8] H. C. Starritt, M. A. Perkins, F. A. Duck, and V. F. Humphrey. Evidence for ultrasonic finite-amplitude distortion in muscle using medical equipment. *The Journal of the Acoustical Society of America*, 77(1):302–306, 1985.

[9] V. A. Khokhlova, R. Souchon, J. Tavakkoli, O. A. Sapozhnikov, and D. Cathignol. Numerical modeling of finite amplitude sound beams: Shock formation in the near field of a CW plane piston source. *The Journal of the Acoustical Society of America*, 110(1):95–108, 2001.

[10] M. F. Hamilton and D. T. Blackstock, eds. *Nonlinear Acoustics*. Academic Press, 1998.

[11] C. M. Sehgal and J. F. Greenleaf. Scattering of ultrasound by tissues. *Ultrasonic imaging*, 6(1):60–80, 1984.

[12] P. N. T. Wells. Ultrasonic imaging of the human body. *Reports on Progress in Physics*, 62(5):671–722, 1999.

[13] W. L. Nyborg. Heat generation by ultrasound in a relaxing medium. *The Journal of the Acoustical Society of America*, 20(2):310–312, 1981.

[14] W. L. Nyborg. Sonically produced heat in a fluid with bulk viscosity and shear viscosity. *The Journal of the Acoustical Society of America*, 80(4):1133–1139, 1986.

[15] C. R. Hill, J. C. Bamber, and G. R. ter Haar, eds. *Physical Principles of Medical Ultrasonics*, chapter Attenuation and Absorption, 93–166. Wiley, 2004.

[16] S. A. Goss, L. A. Frizzell, and F. Dunn. Ultrasonic absorption and attenuation in mammalian tissues. *Ultrasound in Medicine & Biology*, 5(2):181–186, 1979.

[17] D. R. Bacon and E. L. Carstensen. Increased heating by diagnostic ultrasound due to nonlinear propagation. *The Journal of the Acoustical Society of America*, 88(1):26–34, 1990.

[18] F. P. Curra, P. D. Mourad, V. A. Khokhlova, R. O. Cleveland, and L. A. Crum. Numerical simulations of heating patterns and tissue temperature response due to high-intensity focused ultrasound. *IEEE Transactions on Ultrasonics, Ferroelectrics, and Frequency Control*, 47:1077–1089, 2000.

[19] R. G. Holt and R. A. Roy. Measurements of bubble-enhanced heating from focused, mhz-frequency ultrasound in a tissue-mimicking material. *Ultrasound in Medicine & Biology*, 27(10):1399–1412, 2001.

[20] C. C. Coussios, C. H. Farny, G. R. ter Haar, and R. A. Roy. Role of acoustic cavitation in the delivery and monitoring of cancer treatment by high-intensity focused ultrasound (HIFU). *International Journal of Hyperthermia*, 23(2):105–120, 2007.

[21] C. H. Farny, R. G. Holt, and R. A. Roy. The correlation between bubble-enhanced HIFU heating and cavitation. *IEEE Transactions on Biomedical Engineering*, 57:175–184, 2010.

[22] C. A. Speed. Therapeutic ultrasound in soft tissue lesions. *Rheumatology*, 40(12):1331–1336, 2001.

[23] T. Watson. Ultrasound in contemporary physiotherapy practice. *Ultrasonics*, 48:321–329, 2008.

[24] J. van der Zee. Heating the patient: a promising approach? *Annals of Oncology*, 13:1173–1184, 2002.

[25] H.-G. Zhang, K. Mehta, P. Cohen, and C. Guha. Hyperthermia on immune regulation: a temperature's story. *Cancer Letters*, 271:191–204, 2008.

[26] J. R. Ellis and F.-U. Hartl. Protein folding and chaperones. In *Encyclopedia of Life Sciences*. Wiley, 2006.

[27] F. Despa, D. P. Orgill, J. Neuwalder, and R. C. Lee. The relative thermal stability of tissue macromolecules and cellular structure in burn injury. *Burns*, 31:568–577, 2005.

[28] F. Wu, W.-Z. Chen, J. Bai, J.-Z. Zou, Z.-L. Wang, H. Zhu, and Z.-B. Wang. Tumor vessel destruction resulting from high intensity focused ultrasound in patients with solid malignancies. *Ultrasound in Medicine & Biology*, 28(4):535–542, 2002.

[29] R. Agah, A. H. Gandjbakhche, M. Massoud, R. Nossal, and R. F. Bonner. Dynamics of temperature dependent optical properties of tissue: Dependence on thermally induced alteration. *IEEE Transactions on Biomedical Engineering*, 43(8):839–846, 1996.

[30] H. Yoshimura, J. A. Viator, and S. L. Jacques. Relationship between damaged fraction and reflected spectra of denaturing tissues. *Lasers in Surgery and Medicine*, 37(4):308–313, 2005.

[31] N. T. Zervas and A. Kuwayama. Pathological characteristics of experimental thermal lesions: Comparison of inducting heating and radiofrequency electrocoagulation. *Journal of Neurosurgery*, 37:418–422, 1972.

[32] F. Wu, W.-Z. Chen, J. Bai, J.-Z. Zou, Z.-L. Wang, H. Zhu, and Z.-B. Wang. Pathological changes in human malignant carcinoma treated with high-intensity focused ultrasound. *Ultrasound in Medicine & Biology*, 27(8):1099–1106, 2001.

[33] T. Wu, J. P. Felmlee, J. F. Greenleaf, S. J. Riederer, and R. L. Ehman. Assessment of thermal tissue ablation with MR elastography. *Magnetic Resonance in Medicine*, 45:80–87, 2001.

[34] R. Righetti, F. Kallel, R. J. Stafford, R. E. Price, T. A. Krouskop, J. D. Hazle, and J. Ophir. Elastographic characterization of HIFU-induced lesions in canine livers. *Ultrasound in Medicine & Biology*, 25(7):1099–1113, 1999.

[35] S. Bharat, U. Techavipoo, M. Z. Kiss, W. Liu, and T. Varghese. Monitoring stiffness changes in lesions after radiofrequency ablation at different temperatures and durations of ablation. *Ultrasound in Medicine & Biology*, 31(3):415–422, 2005.

[36] C. Maleke and E. E. Konofagou. Harmonic motion imaging for focused ultrasound (hmifu): a fully integrated technique for sonication and monitoring

of the thermal ablation in tissues. *Physics in Medicine and Biology*, 53:1773–1793, 2008.

[37] S. A. Sapareto and W. C. Dewey. Thermal dose determination in cancer therapy. *International Journal of Radiation Oncology, Biology, Physics*, 10(6):787–800, 1984.

[38] M. W. Dewhirst, B. L. Viglianti, M. Lora-Michiels, M. Hanson, and P. J. Hoopes. Basic principles of thermal dosimetry and thermal thresholds for tissue damage from hyperthermia. *International Journal of Hyperthermia*, 19(3):267–294, 2003.

[39] C. Damianou and K. Hynynen. The effect of various physical parameters on the size and shape of necrosed tissue volume during ultrasound surgery. *The Journal of the Acoustical Society of America*, 95(3):1641–1649, 1994.

[40] J. Hindley, W. M. Gedroyc, L. Regan, E. Stewart, C. Tempany, K. Hynynen, N. Macdanold, Y. Inbar, Y. Itzchak, J. Rabinovici, K. Kim, J.-F. Geschwind, G. Hesley, B. Gostout, T. Ehrenstein, S. Hengst, M. Sklair-Levy, A. Shushan, and F. Jolesz. MRI guidance of focused ultrasound therapy of uterine fibroids: Early results. *Am J Roentgenol*, 183(6):1713–1719, 2004.

[41] N. McDannold, N. Vykhodtseva, and K. Hynynen. Targeted disruption of the blood-brain barrier with focused ultrasound: association with cavitation activity. *Physics in Medicine and Biology*, 51(4):793–807, 2006.

[42] I. Rivens, A. Shaw, J. Civale, and H. Morris. Treatment monitoring and

thermometry for therapeutic focused ultrasound. *International Journal of Hyperthermia*, 23(2):121–139, 2007.

[43] S. D. Nandlall, M. Arora, H. A. Schiffter, and C. C. Coussios. On the applicability of the thermal dose cumulative equivalent minutes metric to the denaturation of bovine serum albumin in a polyacrylamide tissue phantom. *Proceedings of the 8th International Symposium on Therapeutic Ultrasound, AIP*, 1113:205–209, 2009.

[44] M. Menzinger and R. Wolfgang. The meaning and use of the arrhenius activation energy. *Angewandte Chemie International Edition in English*, 8(6):438–444, 1969.

[45] K. J. Laidler. The development of the Arrhenius equation. *Journal of Chemical Education*, 61(6):494–498, 1984.

[46] N. T. Wright. On a relationship between the arrhenius parameters from thermal damage studies. *Journal of Biochemical Engineering*, 125(2):300–304, 2003.

[47] N. P. Brunton, J. G. Lyng, L. Zhang, and J. C. Jacquier. The use of dielectric properties and other physical analyses for assessing protein denaturation in beef *biceps femoris* muscle during cooking from 5 to 85°c. *Meat Science*, 72:236–244, 2006.

[48] E. A. Neppiras. Acoustic cavitation. *Physics Reports*, 61(3):159–251, 1980.

[49] C. E. Brennen. *Cavitation and Bubble Dynamics*. Oxford University Press, Oxford, 1995.

[50] M. Minnaert. On musical air bubbles and the sounds of running water. *Philosophical Magazine*, 16:235–248, 1933.

[51] T. G. Leighton and A. J. Walton. An experimental study of the sound emitted from gas bubbles in a liquid. *European Journal of Physics*, 8(2):98–104, 1987.

[52] H. G. Flynn. Cavitation dynamics. i. a mathematical formulation. *The Journal of the Acoustical Society of America*, 57(6):1379–1396, 1975.

[53] C. C. Church and E. L. Carstensen. "stable" inertial cavitation. *Ultrasound in Medicine & Biology*, 27(10):1435–1437, 2001.

[54] R. Hickling and M. S. Plesset. Collapse and rebound of a spherical bubble in water. *The Physics of Fluids*, 7(1):7–14, 1964.

[55] S. Fujikawa and T. Akamatsu. Effects of the non-equilibrium condensation of vapour on the pressure wave produced by the collapse of a bubble in a liquid. *Journal of Fluid Mechanics*, 97(3):481–512, 1980.

[56] J. R. T. Collin. *Detection and Interpretation of Thermally Relevant Cavitation During HIFU Exposure*. Ph.D. thesis, University of Oxford, 2009.

[57] A. Vogel, W. Lauterborn, and R. Timm. Optical and acoustic investigations of the dynamics of laser-produced cavitation bubbles near a solid boundary. *Journal of Fluid Mechanics*, 206:299–338, 1989.

[58] T. G. Leighton. Bubble population phenomena in acoustic cavitation. *Ultrasonics Sonochemistry*, 2(2):S123–S136, 1995.

[59] G. R. ter Haar and S. Daniels. Evidence for ultrasonically induced cavitation in vivo. *Physics in Medicine and Biology*, 26(6):1145–1149, 1981.

[60] C. K. Holland, C. X. Deng, R. E. Apfel, J. L. Alderman, L. A. Fernandez, and K. J. W. Taylor. Direct evidence of cavitation in vivo from diagnostic ultrasound. *Ultrasound in Medicine & Biology*, 22(7):917–925, 1996.

[61] E. N. Harvey, D. K. Barnes, W. D. McElroy, A. H. Whiteley, D. C. Pease, and K. W. Cooper. Bubble formation in animals. i. physical factors. *Journal of Cellular and Comparative Physiology*, 24(1):1–22, 1944.

[62] R. E. Apfel. The role of impurities in cavitation-threshold determination. *The Journal of the Acoustical Society of America*, 48(5B):1179–1186, 1970.

[63] L. A. Crum. Nucleation and stabilization of microbubbles in liquids. *Applied Scientific Research*, 38(1):101–115, 1982.

[64] A. A. Atchley and A. Prosperetti. The crevice model of bubble nucleation. *The Journal of the Acoustical Society of America*, 86(3):1065–1084, 1989.

[65] D. E. Yount, E. W. Gillary, and D. C. Hoffman. A microscopic investigation of bubble formation nuclei. *The Journal of the Acoustical Society of America*, 76(5):1511–1521, 1984.

[66] D. N. Walder and A. Evans. In vivo nuclear fission in the aetiology of decompression sickness. *Nature*, 252(5485):696–697, 1974.

[67] D. Sette and F. Wanderlingh. Nucleation by cosmic rays in ultrasonic cavitation. *Physical Review*, 125(2):409–417, 1962.

[68] K. G. Ikels. Production of gas bubbles in fluids by tribonucleation. *Journal of Applied Physiology*, 28(4):524–527, 1970.

[69] J. Herbertz. Spontaneous cavitation in liquids free of nuclei. *Fortschritte der Akustik DAGA*, 14:439–442, 1988.

[70] C. C. Church. Spontaneous homogeneous nucleation, inertial cavitation and the safety of diagnostic ultrasound. *Ultrasound in Medicine & Biology*, 28(10):1349–1364, 2002.

[71] R. E. Apfel and C. K. Holland. Gauging the likelihood of cavitation from short-pulse, low-duty cycle diagnostic ultrasound. *Ultrasound in Medicine & Biology*, 17(2):179–185, 1991.

[72] F. R. Young. *Cavitation*. Imperial College Press, London, 1989.

[73] C. C. Church. Prediction of rectified diffusion during nonlinear bubble pulsations at biomedical frequencies. *The Journal of the Acoustical Society of America*, 83(6):2210–2217, 1988.

[74] I. R. Webb, M. Arora, J. R. T. Collin, S. J. Payne, R. A. Roy, and C. C. Coussios. The effect of hifu-relevant rates of heating on the growth and dissolution of nuclei available for inertial cavitation. In *Proceedings of 19th International Conference on Acoustics, Madrid*. 2007.

[75] T. G. Leighton. *The acoustic bubble*. San Diego : Academic Press, c1994., 1997.

[76] V. A. Khokhlova, M. R. Bailey, J. A. Reed, B. W. Cunitz, P. J. Kaczkowski, and L. A. Crum. Effects of nonlinear propagation, cavitation, and boiling in lesion formation by high intensity focused ultrasound in a gel phantom. *The Journal of the Acoustical Society of America*, 119(3):1834–1848, 2006.

[77] A. Anand and P. J. Kaczkowski. Monitoring formation of high intensity focused ultrasound (HIFU) induced lesions using backscattered ultrasound. *Acoustics Research Letters Online*, 5(3):88, 2004.

[78] C. H. Farny, R. G. Holt, and R. A. Roy. Temporal and spatial detection of HIFU-induced inertial and hot-vapor cavitation with a diagnostic ultrasound system. *Ultrasound in Medicine & Biology*, 35(4):603–615, 2009.

[79] S. Datta, C. C. Coussios, L. E. McAdory, J. Tan, T. Porter, G. D. Courten-Myers, and C. K. Holland. Correlation of cavitation with ultrasound enhancement of thrombolysis. *Ultrasound in Medicine & Biology*, 32(8):1257–1267, 2006.

[80] L. Rayleigh. On the pressure developed in a liquid during the collapse of a spherical cavity. *Philosophical Magazine*, 34:94–98, 1917.

[81] J. R. Blake and D. C. Gibson. Growth and collapse of a vapour cavity near a free surface. *Journal of Fluid Mechanics*, 111:123–140, 1981.

[82] W. Lauterborn and H. Bolle. Experimental investigations of cavitation-bubble

collapse in the neighbourhood of a solid boundary. *Journal of Fluid Mechanics*, 72:391–399, 1975.

[83] A. J. Coleman and J. E. Saunders. A review of the physical properties and biological effects of the high amplitude acoustic fields used in extracorporeal lithotripsy. *Ultrasonics*, 31(2):75–89, 1993.

[84] A. Maxwell, C. Cain, A. P. Duryea, L. Yuan, H. S. Gurm, and Z. Xu. Noninvasive thrombolysis using pulsed ultrasound cavitation therapy – histotripsy. *Ult Med Biol*, 35(12):1982–1994, 2009.

[85] T.-Y. Wang, Z. Xu, W. Frank, T. L. Hall, J. B. Fowlkes, E. D. Rothman, W. W. Roberts, and C. Cain. Quantitative image feedback for pulsed cavitational ultrasound therapy – histotripsy. *IEEE Trans Ultrason Ferroelectr Freq Control*, 56(5):995–1005, 2009.

[86] Z. Xu, Z. Fan, T. L. Hall, F. Winterroth, J. B. Fowlkes, and C. Cain. Size measurement of tissue debris particles generated from pulse ultrasound cavitational therapy – histotripsy. *Ult Med Biol*, 35(2):245–255, 2009.

[87] C. D. Ohl, M. Arora, R. Ikink, N. de Jong, M. Versluis, M. Delius, and D. Lohse. Sonoporation from jetting cavitation bubbles. *Biophysical Journal*, 91(11):4285–4295, 2006.

[88] H. Tang, C. C. Wang, D. Blanksctein, and R. Langer. An investigation of the role of cavitation in low-frequency ultrasound-mediated transdermal drug transport. *Pharmaceutical Research*, 19:1160–1169, 2002.

[89] H. Ueda, M. Mutoh, T. Seki, D. Kobayashi, and Y. Morimoto. Acoustic cavitation as an enhancing mechanism of low-frequency sonophoresis for transdermal drug delivery. *Biological and Pharmaceutical Bulletin*, 32(5):916–920, 2009.

[90] K. G. Baker, V. J. Robertson, and F. A. Duck. A review of therapeutic ultrasound: Biophysical effects. *Physical Therapy*, 81:1351–1358, 2001.

[91] A. Sarvazyan. Diversity of biomedical applications of acoustic radiation force. *Ultrasonics*, 50(2):230–234, 2010.

[92] B.-T. Chu and R. E. Apfel. Acoustic radiation pressure produced by a beam of sound. *The Journal of the Acoustical Society of America*, 72(6):1673–1687, 1982.

[93] W. L. Nyborg. Acoustic streaming due to attenuated plane waves. *The Journal of the Acoustical Society of America*, 25(1):68–75, 1953.

[94] W. D. O'Brien. Ultrasound-biophysics mechanisms. *Progress in Biophysics and Molecular Biology*, 93(1-3):212–255, 2007.

[95] J. Harle, F. Mayia, I. Olsen, and V. Salih. Effects of ultrasound on transforming growth factor-beta genes in bone cells. *European Cells and Materials*, 10:70–6; discussion 76, 2005.

[96] S. L. Poliachik, W. L. Chandler, P. D. Mourad, R. J. Ollos, and L. A. Crum. Activation, aggregation and adhesion of platelets exposed to high intensity focused ultrasound. *IEEE Ultrasonics Symposium*, 2:1433–1436 vol.2, 2000.

[97] S. Vaezy and V. Zderic. Hemorrhage control using high intensity focused ultrasound. *International Journal of Hyperthermia*, 23(2):203–211, 2007.

[98] J. E. Kennedy. High-intensity focused ultrasound in the treatment of solid tumours. *Nature Reviews Cancer*, 5(4):321–327, 2005.

[99] H. H. Pennes. Analysis of tissue and arterial blood temperatures in the resting human forearm. *Journal of Applied Physiology*, 1(2):93–122, 1948.

[100] L. Chen, I. Rivens, G. ter Haa, S. Riddler, C. Hill, and J. Bensted. Histological changes in rat liver tumours treated with high-intensity focused ultrasound. *Ultrasound in Medicine & Biology*, 19(1):67–74, 1993.

[101] H. L. Liu, N. McDannold, and K. Hynynen. Focal beam distortion and treatment planning in abdominal focused ultrasound surgery. *Medical Physics*, 32(5):1270–1280, 2005.

[102] M. R. Bailey, L. N. Couret, O. A. Sapozhnikov, V. A. Khokhlova, G. R. ter Haar, S. Vaezy, X. Shi, R. W. Martin, and L. A. Crum. Use of overpressure to assess the role of bubbles in focused ultrasound lesion shape in vitro. *Ultrasound in Medicine & Biology*, 27(5):695–708, 2001.

[103] W.-S. Chen, C. Lafon, T. J. Matula, S. Vaezy, and L. A. Crum. Mechanisms of lesion formation in high intensity focused ultrasound therapy. *Acoustics Research Letters Online*, 4(2):41–46, 2003.

[104] A. Payne, U. Vyas, A. Blankespoor, D. Christensen, and R. Roemer. Minimi-

sation of hifu pulse heating and interpulse cooling times. *International Journal of Hyperthermia*, 26(2):198–208, 2010.

[105] R. Yang, K. K. Kopecky, F. J. Rescorla, C. A. Galliani, E. X. Wu, and J. L. Grosfeld. Sonographic and computed tomography characteristics of liver ablation lesions induced by high-intensity focussed ultrasound. *Investigative Radiology*, 28(9):796–801, 1993.

[106] K. D. Paulsen, M. J. Moskowitz, T. P. Ryan, S. E. Mitchell, and P. J. Hoopes. Initial in vivo experience with eit as a thermal estimator during hyperthermia. *International Journal of Hyperthermia*, 12(5):573–91; discussion 593–4, 1996.

[107] S. Vaezy, M. Andrew, P. Kaczkowski, and L. Crum. Image-guided acoustic therapy. *Annual Review of Biomedical Engineering*, 3(1):375–390, 2001.

[108] X. Jin, Y. Xu, L. V. Wang, Y. R. Fang, C. I. Zanelli, and S. M. Howard. Imaging of high-intensity focused ultrasound-induced lesions in soft biological tissue using thermoacoustic tomography. *Medical Physics*, 32(1):5–11, 2005.

[109] B. J. Wood, J. Yanof, V. Frenkel, A. Viswanathan, S. Dromi, K. Oh, J. Kruecker, C. Bauer, R. Seip, A. Kam, and K. C. P. Li. CT and ultrasound guided stereotactic high intensity focused ultrasound (HIFU). *AIP Conference Proceedings*, 829(1):122–126, 2006.

[110] P. M. Meaney, T. Zhou, M. W. Fanning, S. D. Geimer, and K. D. Paulsen. Microwave thermal imaging of scanned focused ultrasound heating: Phantom results. *International Journal of Hyperthermia*, 24(7):523–536, 2008.

[111] K. Hynynen, O. Pomeroy, D. N. Smith, P. E. Huber, N. J. McDannold, J. Kettenbach, J. Baum, S. Singer, and F. A. Jolesz. MR imaging-guided focused ultrasound surgery of fibroadenomas in the breast: A feasibility study. *Radiology*, 219(1):176–185, 2001.

[112] E. A. Stewart, J. Rabinovici, C. M. Tempany, Y. Inbar, L. Regan, B. Gastout, G. Hesley, H. S. Kim, S. Hengst, and W. M. Gedroye. Clinical outcomes of focused ultrasound surgery for the treatment of uterine fibroids. *Fertil Steril*, 85(1):22–29, 2006.

[113] F. A. Jolesz. MRI-guided focused ultrasound surgery. *Annu Rev Med*, 60:417–430, 2009.

[114] K. Hynynen. MRI-guided focused ultrasound treatments. *Ultrasonics*, 50:221–229, 2010.

[115] J. P. Hornak. *The Basics of MRI*. www.cis.rit.edu/htbooks/mri, 1997.

[116] R. H. Hashemi, J. William G. Bradley, and C. J. Lisanti. *MRI: The Basics*. Lippincott Williams & Wilkins, second edition, 2004.

[117] C. Damianou, M. Pavlou, O. Velev, K. Kyriakou, and M. Trimikliniotis. High intensity focused ultrasound ablation of kidney guided by MRI. *Ultrasound in Medicine & Biology*, 30(3):397–404, 2004.

[118] K. Hynynen, A. Darkazanli, E. Unger, and J. F. Schenck. MRI-guided noninvasive ultrasound surgery. *Medical Physics*, 20(1):107–115, 1993.

[119] S. D. Sokka, R. King, and K. Hynynen. MRI-guided gas bubble enhanced ultrasound heating in in vivo rabbit thigh. *Physics in Medicine and Biology*, 48(2):223–241, 2003.

[120] B. Quesson, J. A. de Zwart, and C. T. Moonen. Magnetic resonance temperature imaging for guidance of thermotherapy. *Journal of Magnetic Resonance Imaging*, 12(4):525–533, 2000.

[121] B. de Senneville, C. Mougenot, B. Quesson, I. Dragonu, N. Grenier, and C. Moonen. MR thermometry for monitoring tumor ablation. *European Radiology*, 17(9):2401–2410, 2007.

[122] H. E. Cline, K. Hynynen, C. J. Hardy, R. D. Watkins, J. F. Schenck, and F. A. Jolesz. MR temperature mapping of focused ultrasound surgery. *Magnetic Resonance in Medicine*, 31(6):628–636, 1994.

[123] D. L. Bihan, J. Delannoy, and R. Levin. Temperature mapping with MR imaging of molecular diffusion: application to hyperthermia. *Radiology*, 171(3):853–857, 1989.

[124] K. Hynynen, W. Freund, H. Cline, A. Chung, R. Watkins, J. Vetro, and F. Jolesz. A clinical, noninvasive, MR imaging-monitored ultrasound surgery method. *Radiographics*, 16(1):185–195, 1996.

[125] J. A. de Zwart, F. C. Vimeux, Palussière, R. Salomir, B. Quesson, C. Delalande, and C. T. W. Moonen. On-line correction and visualization of motion during MRI-controlled hyperthermia. *Magnetic Resonance in Medicine*, 45:128–137, 2001.

[126] A. C. Schmitz, D. Gianfelice, B. L. Daniel, W. P. T. M. Mali, and M. A. A. J. van den Bosch. Image-guided focused ultrasound ablation of breast cancer: current status, challenges and future directions. *European Radiology*, 18:1431–1441, 2008.

[127] X. Zhou, Q. He, A. Zhang, M. Beckmann, and C. Ni. Temperature measurement error reduction for mri-guided hifu treatment. *International Journal of Hyperthermia*, 26:347–358, 2010.

[128] K. R. Gorny, N. J. Hangiandreou, G. K. Hesley, B. S. Gostout, K. P. McGee, and J. P. Felmlee. MR guided focused ultrasound: technical acceptance measures for a clinical system. *Physics in Medicine and Biology*, 51:3155–3173, 2006.

[129] R. M. Arthur, W. L. Straube, J. W. Trobaugh, and E. G. Moros. Non-invasive estimation of hyperthermia temperatures with ultrasound. *International Journal of Hyperthermia*, 21(6):589–600, 2005.

[130] N. L. Bush, I. Rivens, G. R. ter Haar, and J. C. Bamber. Acoustic properties of lesions generated with an ultrasound therapy system. *Ultrasound in Medicine & Biology*, 19(9):789–801, 1993.

[131] R. Maass-Moreno. Noninvasive temperature estimation in tissue via ultrasound echo-shifts. part ii. in vitro study. *The Journal of the Acoustical Society of America*, 100(4):2522, 1996.

[132] M. R. Gertner, B. C. Wilson, and M. D. Sherar. Ultrasound properties of

liver tissue during heating. *Ultrasound in Medicine & Biology*, 23(9):1395–1403, 1997.

[133] T. Szabo. *Diagnostic Ultrasound Imaging: Inside Out (Biomedical Engineering Series)*. Academic Press, 2004.

[134] S. Vaezy, X. Shi, R. W. Martin, E. Chi, P. I. Nelson, M. R. Bailey, and L. A. Crum. Real-time visualization of high-intensity focused ultrasound treatment using ultrasound imaging. *Ultrasound in Medicine & Biology*, 27(1):33–42, 2001.

[135] N. R. Owen, M. R. Bailey, J. Hossack, and L. A. Crum. A method to synchronize high-intensity, focused ultrasound with an arbitrary ultrasound imager. *IEEE Transactions on Ultrasonics, Ferroelectrics, and Frequency Control*, 53(3):645–650, 2006.

[136] C. C. Coussios, C. H. Farny, C. R. Thomas, R. O. Cleveland, R. G. Holt, and R. A. Roy. Cavitation detection during and following HIFU exposure in vitro. *The Journal of the Acoustical Society of America*, 115(5):2448, 2004.

[137] B. A. Rabkin, V. Zderic, and S. Vaezy. Hyperecho in ultrasound images of HIFU therapy: involvement of cavitation. *Ultrasound in Medicine & Biology*, 31(7):947–956, 2005.

[138] B. A. Rabkin, V. Zderic, L. A. Crum, and S. Vaezy. Biological and physical mechanisms of HIFU-induced hyperecho in ultrasound images. *Ultrasound in Medicine & Biology*, 32(11):1721–1729, 2006.

[139] B. A. Rabkin, V. Zderic, and S. Vaezy. HIFU-induced hyperecho in ultrasound images, cavitation activity and thermal behavior. *AIP Conference Proceedings*, 754:43–46, 2005.

[140] T. Yu and C. Xu. Hyperecho as the indicator of tissue necrosis during microbubble-assisted high intensity focused ultrasound: sensitivity, specificity and predictive value. *Ult Med Biol*, 34(8):1343–1347, 2008.

[141] N. R. Miller, J. C. Bamber, and G. R. ter Haar. Imaging of temperature-induced echo strain: preliminary in vitro study to assess feasibility for guiding focused ultrasound surgery. *Ultrasound in Medicine & Biology*, 30(3):345–356, 2004.

[142] J. C. Bamber and C. R. Hill. Ultrasonic attenuation and propagation speed in mammalian tissues as a function of temperature. *Ultrasound in Medicine & Biology*, 5(2):149–157, 1979.

[143] M. A. Lubinski. Speckle tracking methods for ultrasonic elasticity imaging using short-time correlation. *IEEE Transactions on Ultrasonics, Ferroelectrics, and Frequency Control*, 46(1):82–96, 1999.

[144] R. Souchon, G. Bouchoux, E. Maciejko, C. Lafon, D. Cathignol, M. Bertrand, and J.-Y. Chapelon. Monitoring the formation of thermal lesions with heat-induced echo-strain imaging: A feasibility study. *Ultrasound in Medicine & Biology*, 31(2):251– 259, 2005.

[145] T. Varghese, J. A. Zagzebski, Q. Chen, U. Techavipoo, G. Frank, C. Johnson, A. Wright, and F. T. Lee. Ultrasound monitoring of temperature change

during radiofrequency ablation: preliminary in-vivo results. *Ultrasound in Medicine & Biology*, 28(3):321–329, 2002.

[146] U. Techavipoo, T. Varghese, Q. Chen, T. A. Stiles, J. A. Zagzebski, and G. R. Frank. Temperature dependence of ultrasonic propagation speed and attenuation in excised canine liver tissue measured using transmitted and reflected pulses. *The Journal of the Acoustical Society of America*, 115(6):2859–2865, 2004.

[147] R. L. Nasoni, T. Bowen, W. G. Connor, and R. R. Sholes. In vivo temperature dependence of ultrasound speed in tissue and its application to noninvasive temperature monitoring. *Ultrasonic imaging*, 1(1):34, 1979.

[148] D. Liu and E. S. Ebbini. Real-time 2-d temperature imaging using ultrasound. *IEEE Transactions on Biomedical Engineering*, 57:1, 2010.

[149] W. L. Straube and R. M. Arthur. Theoretical estimation of the temperature dependence of backscattered ultrasonic power for noninvasive thermometry. *Ultrasound in Medicine & Biology*, 20(9):915–922, 1994.

[150] R. M. Arthur, J. W. Trobaugh, W. L. Straube, and E. G. Moros. Temperature dependence of ultrasonic backscattered energy in motion-compensated images. *IEEE Transactions on Ultrasonics, Ferroelectrics, and Frequency Control*, 52(10):1644–1652, 2005.

[151] C. A. Damianou, N. T. Sanghvi, F. J. Fry, and R. Maass-Moreno. Dependence of ultrasonic attenuation and absorption in dog soft tissues on temperature and

thermal dose. *The Journal of the Acoustical Society of America*, 102(1):628–634, 1997.

[152] R. L. Clarke, N. L. Bush, and G. R. Ter Haar. The changes in acoustic attenuation due to in vitro heating. *Ultrasound in Medicine & Biology*, 29(1):127–135, 2003.

[153] A. E. Worthington, J. Trachtenberg, and M. D. Sherar. Ultrasound properties of human prostate tissue during heating. *Ultrasound in Medicine & Biology*, 28(10):1311–1318, 2002.

[154] M. Ribault, J. Y. Chapelon, D. Cathignol, and A. Gelet. Differential attenuation imaging for the characterization of high intensity focused ultrasound lesions. *Ultrasonic imaging*, 20(3):160–177, 1998.

[155] P. D. Bevan and M. D. Sherar. B-scan ultrasound imaging of thermal coagulation in bovine liver: frequency shift attenuation mapping. *Ultrasound in Medicine & Biology*, 27(6):809–817, 2001.

[156] P. D. Bevan and M. D. Sherar. B-scan ultrasound imaging of thermal coagulation in bovine liver: log envelope slope attenuation mapping. *Ultrasound in Medicine & Biology*, 27(3):379–387, 2001.

[157] J. Ophir, S. K. Alam, B. S. Garra, F. Kallel, E. E. Konofagou, T. Krouskop, C. R. B. Merritt, R. Righetti, R. Souchon, S. Srinivasan, and T. Varghese. Elastography: Imaging the elastic properties of soft tissues with ultrasound. *Journal of Medical Ultrasonics*, 29(4):155–171, 2002.

[158] E. E. Konofagou. Quo vadis elasticity imaging? *Ultrasonics*, 42(1-9):331–336, 2004.

[159] T. Varghese, J. A. Zagzebski, and F. T. Lee. Elastographic imaging of thermal lesions in the liver in vivo following radiofrequency ablation: preliminary results. *Ultrasound in Medicine & Biology*, 28(11-12):1467–1473, 2002.

[160] T. Varghese and H. Shi. Elastographic imaging of thermal lesions in liver in-vivo using diaphragmatic stimuli. *Ultrasonic imaging*, 26(1):18–28, 2004.

[161] G. Pareek, E. R. Wilkinson, S. Bharat, T. Varghese, P. F. Laeseke, F. T. L. Jr, T. F. Warner, J. A. Zagzebski, and S. Y. Nakada. Elastographic measurements of in-vivo radiofrequency ablation lesions of the kidney. *Journal of Endourology*, 20(11):959–964, 2006.

[162] L. Curiel, R. Souchon, O. Rouvire, A. Gelet, and J. Y. Chapelo. Elastography for the follow-up of high-intensity focused ultrasound prostate cancer treatment: initial comparison with MRI. *Ultrasound in Medicine & Biology*, 31(11):1461–1468, 2005.

[163] K. R. Nightingale, M. L. Palmeri, R. W. Nightingale, and G. E. Trahey. On the feasibility of remote palpation using acoustic radiation force. *The Journal of the Acoustical Society of America*, 110(1):625–634, 2001.

[164] B. J. Fahey, K. R. Nightingale, D. L. Stutz, and G. E. Trahey. Acoustic radiation force impulse imaging of thermally- and chemically-induced lesions in soft tissues: preliminary ex vivo results. *Ultrasound in Medicine & Biology*, 30(3):321–328, 2004.

[165] F. L. Lizzi, R. Muratore, C. X. Deng, J. A. Ketterling, S. K. Alam, S. Mikaelian, and A. Kalisz. Radiation-force technique to monitor lesions during ultrasonic therapy. *Ultrasound in Medicine & Biology*, 29(11):1593–1605, 2003.

[166] M. Fatemi and J. F. Greenleaf. Vibro-acoustography: An imaging modality based on ultrasound-stimulated acoustic emission. *PNAS*, 96(12):6603–6608, 1999.

[167] E. Konofagou, J. Thierman, and K. Hynynen. The use of ultrasound-stimulated acoustic emission in the monitoring of modulus changes with temperature. *Ultrasonics*, 41(5):337–345, 2003.

[168] J. Bercoff, M. Pernot, M. Tanter, and M. Fink. Monitoring thermally-induced lesions with supersonic shear imaging. *Ultrasonic imaging*, 26(2):71–84, 2004.

[169] J. McLaughlin and D. Renzi. Shear wave speed recovery in transient elastography and supersonic imaging using propagating fronts. *Inverse Problems*, 22:681–706, 2006.

[170] R. Muthupillai, P. J. Ross, D. J. Lomas, J. F. Greenleaf, S. J. Riederer, and R. L. Ehman. Magnetic resonance imaging of transverse acoustic strain waves. *Magnetic Resonance in Medicine*, 36(2):266–274, 1996.

[171] B. Larrat, M. Pernot, J.-F. Aubry, E. Dervishi, R. Sinkus, D. Seilhean, Y. Marie, B. A-L, M. Fink, and M. Tanter. MR-guided transcranial brain HIFU in small animal models. *Physics in Medicine and Biology*, 55:365–388, 2010.

[172] L. Huwart, N. Salameh, L. ter Beek, E. Vicaut, F. Peeters, R. Sinkus, and B. E. Van Beers. MR elastography of liver fibrosis: preliminary results comparing spin-echo and echo-planar imaging. *European Radiology*, 18:2535–2541, 2008.

[173] D. Razansky, P. D. Einziger, and D. R. Adam. Enhanced heat deposition using ultrasound contrast agent–modeling and experimental observations. *IEEE Transactions on Ultrasonics, Ferroelectrics, and Frequency Control*, 53(1):137–147, 2006.

[174] T. G. Leighton. A strategy for the development and standardisation of measurement methods for high power/cavitating ultrasonic fields: Review of cavitation monitoring techniques. Technical Report ISVR Technical Report No. 263, , 1997.

[175] ANSI. Bubble detection and cavitation monitoring. Technical Report Technical Report, , 2002.

[176] T. G. Leighton, P. Birkin, M. Hodnett, B. Zeqiri, J. Power, G. Price, T. Mason, M. Plattes, N. Dezhnukov, and A. Coleman. *Bubble and Particle Dynamics in Acoustic Fields: Modern Trends and Applications*, chapter Characterization of measures of reference acoustic cavitation (COMORAC): an experimental feasibility trial, 37–94. Research Signpost, 2005.

[177] R. A. Roy, S. I. Madanshetty, and R. E. Apfel. An acoustic backscattering technique for the detection of transient cavitation produced by microsecond pulses of ultrasound. *The Journal of the Acoustical Society of America*, 87(6):2451–2458, 1990.

[178] A. J. Coleman, M. Whitlock, T. Leighton, and J. E. S. J.E. The spatial distribution of cavitation induced acoustic emission, sonoluminescence and cell lysis in the field of a shock wave lithotripter. *Physics in Medicine and Biology*, 38(16):1545–1560, 1993.

[179] C. H. Farny. *Identifying and monitoring the roles of cavitation in heating from High Intensity Focused Ultrasound*. Ph.D. thesis, Boston University, 2007.

[180] V. A. Salgaonkar, S. Datta, C. K. Holland, and T. D. Mast. Passive cavitation imaging with ultrasound arrays. *The Journal of the Acoustical Society of America*, 126(6):3071–3083, 2009.

[181] M. Gyöngy, M. Arora, A. J. Noble, and C. C. Coussios. A passive array technique for cavitation mapping during HIFU treatment (A). *The Journal of the Acoustical Society of America*, 123:3223–3223, 2008.

[182] M. Gyöngy, M. Arora, A. J. Noble, and C. C. Coussios. Use of passive arrays for characterization and mapping of cavitation activity during HIFU exposure. In *Ultrasonics Symposium, 2008. IUS 2008. IEEE*, 871–874. 2008.

[183] M. Gyöngy and C. C. Coussios. Passive spatial mapping of inertial cavitation during HIFU exposure. *IEEE Transactions on Biomedical Engineering*, 57(1):48–56, 2010.

[184] S. J. Norton, B. J. Carr, and A. J. Witten. Passive imaging of underground acoustic sources. *The Journal of the Acoustical Society of America*, 119(5):2840–2847, 2006.

[185] M. Gyöngy and C.-C. Coussios. Passive cavitation mapping for localization and tracking of bubble dynamics. *The Journal of the Acoustical Society of America – Express Letters* (submitted), 2010.

[186] M. Gyöngy, R. Ritchie, M. Arora, T. Leslie, and C.-C. Coussios. Monitoring of thermal ablation during HIFU exposure using passive cavitation mapping. In *9th International Symposium on Therapeutic Ultrasound, Aix-en-Provence, France*. 2009.

[187] C. Jensen, R. Ritchie, M. Gyöngy, M. Arora, T. Leslie, and C.-C. Coussios. Spatio-temporal monitoring of HIFU therapy by passive cavitation mapping. *Ultrasound in Medicine & Biology* (to be submitted), 2010.

[188] C. D. Arvanitis, M. Gyöngy, M. Bazan-Peregrino, B. Rifai, L. W. Seymour, and C.-C. Coussios. Passive mapping of cavitation activity for monitoring of drug delivery (A). *The Journal of the Acoustical Society of America*, 127(3):1977–1977, 2010.

[189] C. D. Arvanitis, M. Gyöngy, M. Bazan-Peregrino, B. Rifai, L. W. Seymour, and C.-C. Coussios. Passive ultra-sonography: monitoring, mapping and assessment of cavitation mediated drug delivery. *PNAS* (to be submitted), 2010.

[190] Y. Xu, D. Feng, and L. V. Wang. Exact frequency-domain reconstruction for thermoacoustic tomography – i: Planar geometry. *IEEE Transactions on Medical Imaging*, 21(7):823–828, 2002.

[191] A. P. Dowling and J. E. F. Williams. *Sound and Sources of Sound*. Ellis Horwood, Chichester, 1989.

[192] J. Lighthill. *Waves in Fluids*. Cambridge University Press, 2005.

[193] S. J. Norton and I. J. Won. Time exposure acoustics. *IEEE Transactions on Geoscience and Remote Sensing*, 38(3):1337–1343, 2000.

[194] K. Riley, M. Hobson, and S. Bence. *Mathematical methods for physics and engineering*. Cambridge University Press, 2003.

[195] R. Krimholtz, D. Leedom, and G. Matthaei. New equivalent circuits for elementary piezoelectric transducers. *Electronics Letters*, 6(13):398–399, 1970.

[196] H. T. O'Neil. Theory of focusing radiators. *The Journal of the Acoustical Society of America*, 21(5):516–526, 1949.

[197] P. Crombie, P. Bascom, and R. Cobbold. Calculating the pulsed response of linear arrays: accuracy versus computational efficiency. *IEEE Transactions on Ultrasonics, Ferroelectrics, and Frequency Control*, 44(5):997–1009, 1997.

[198] A. Macovski. Ultrasonic imaging using arrays. *Proceedings of the IEEE*, 67(4):484–495, 1979.

[199] A. Devaney. Inverse source and scattering problems in ultrasonics. *IEEE Transactions on Sonics and Ultrasonics*, 30(6):355–363, 1983.

[200] A. Devaney. The inverse problem for random sources. *J Math Phys*, 20(8):1687–1691, 1979.

[201] B. D. Van Veen and K. M. Buckley. Beamforming: A versatile approach to spatial filtering. *IEEE ASSP Magazine*, 5(2):4–24, 1988.

[202] M. E. Weber and R. Heisler. A frequency-domain beamforming algorithm for wideband, coherent signal processing. *The Journal of the Acoustical Society of America*, 76(4):1132–1144, 1984.

[203] L. C. Godara. Application of the fast fourier transform to broadband beamforming. *The Journal of the Acoustical Society of America*, 98(1):230–240, 1995.

[204] H. Krim and M. Viberg. Two decades of array signal processing research: the parametric approach. *IEEE Signal Processing Magazine*, 13(4):67–94, 1996.

[205] J. Starck and E. Pantin. Deconvolution in astronomy: A review. *Publications of the Astronomical Society of the Pacific*, 114:1051–1069, 2002.

[206] A. Khare and U. Tiwary. A new method for deblurring and denoising of medical images using complex wavelet transform. In *Engineering in Medicine and Biology Society, 2005. IEEE-EMBS 2005. 27th Annual International Conference of the*, 1897–1900. 2005.

[207] D. B. Ward, R. A. Kennedy, and R. C. Williamson. Theory and design of broadband sensor arrays with frequency invariant far-field beam patterns. *The Journal of the Acoustical Society of America*, 97(2):1023–1034, 1995.

[208] K. Thomenius. Evolution of ultrasound beamformers. In *Ultrasonics Symposium, 1996. Proceedings., 1996 IEEE*, volume 2, 1615–1622 vol.2. 1996.

[209] K. Kim and A. D. George. Parallel subspace projection beamforming for au-

tonomous, passive sonar signal processing. *Journal of Computational Acoustics*, 11(1):55–74, 2003.

[210] Y. Kim and P. Nelson. Optimal regularisation for acoustic source reconstruction by inverse methods. *Journal of Sound and Vibration*, 275:463–487, 2004.

[211] M. Wax and T. Kailath. Detection of signals by information theoretic criteria. *IEEE Transactions on Acoustics, Speech, and Signal Processing*, 33(2):387–392, 1985.

[212] P. Stoica and A. Nehorai. Music, maximum likelihood, and cramer-rao bound. *IEEE Transactions on Acoustics, Speech, and Signal Processing*, 37(5):720–741, 1989.

[213] J. M. Mendel. Tutorial on higher-order statistics (spectra) in signal processingand system theory: theoretical results and some applications. *Proceedings of the IEEE*, 79(3):278–305, 1991.

[214] E. Gonen and J. M. Mendel. Applications of cumulants to array processing – part iii: Blind beamforming for coherent signals. *IEEE Transactions on Signal Processing*, 45(9):2252 – 2264, 1997.

[215] E. Gonen, J. M. Mende, and M. C. Dogan. Applications of cumulants to array processing – part iv: Directionfinding in coherent signals case. *IEEE Transactions on Signal Processing*, 45(9):2265–2276, 1997.

[216] T.-H. Liu and J. M. Mendel. Application of cumulants to array signal pro-

cessing – part v: Sensitivity issues. *IEEE Transactions on Signal Processing*, 47(3):746–759, 1999.

[217] Y. Wu, L. Ma, C. Hou, G. Zhang, and J. Li. Subspace-based method for joint range and doa estimation of multiple near-field sources. *Signal processing*, 86(8):2129–2133, 2006.

[218] W. A. Gardner, A. Napolitano, and L. Paura. Cyclostationarity: Half a century of research. *Signal processing*, 86:639–697, 2006.

[219] X. Yan, S. Wang, K. Wang, and H. Jiang. Localization of near field cyclostationary source based on fourth-order cyclic cumulant. In *Signal Processing, 2008. ICSP 2008. 9th International Conference on*, 1629–1632. 2008.

[220] M. Martone. Adaptive multistage beamforming using cyclic higher order-statistics (chos). *IEEE Transactions on Signal Processing*, 47(10):2867–2873, 1999.

[221] M. Wax and T. Kailath. Optimum localization of multiple sources by passive arrays. *IEEE Transactions on Acoustics, Speech, and Signal Processing*, 31(5):1210–1217, 1983.

[222] R. Jeffers, K. Bell, and H. Van Trees. Broadband passive range estimation using music. In *Acoustics, Speech, and Signal Processing, 2002. Proceedings. (ICASSP '02). IEEE International Conference on*, volume 3, III–2921–III–2924 vol.3. 2002.

[223] R. Andrew and R. Kirlin. A broadband maximum likelihood imager for a

class of extended space-time separable sources. *IEEE Transactions on Signal Processing*, 48(5):1287–1294, 2000.

[224] R. K. Andrew, D. M. Farmer, and R. L. Kirlin. Broadband parametric imaging of breaking ocean waves. *The Journal of the Acoustical Society of America*, 110(1):150–162, 2001.

[225] W. R. Hahn. Optimum signal processing for passive sonar range and bearing estimation. *The Journal of the Acoustical Society of America*, 58:201–207, 1975.

[226] J. Christensen and J. Hald. Beamforming. Technical Report 1, Bruel & Kjaer, 2004.

[227] P. R. White, T. G. Leighton, D. C. Finfer, C. Powles, and O. N. Baumann. Localisation of sperm whales using bottom-mounted sensors. *Applied Acoustics*, 67:1074–1090, 2006.

[228] B. Artman. *Passive Seismic Imaging*. Ph.D. thesis, Stanford University, 2007.

[229] J. A. Jensen, O. Holm, L. J. Jensen, H. Bendsen, M. H. Pedersen, and K. Salomonsen. Experimental ultrasound system for real-time synthetic imaging. *Proc IEEE Ultrason Symp*, 1689–1693, 2000.

[230] C.-K. Liao, S.-W. Huang, C.-W. Wei, and P.-C. Li. A high frame rate photoacoustic imaging system and its applications to perfusion measurements. In A. A. Oraevsky and L. V. Wang, eds., *Measurement of Blood Oxygenation*, volume 6086 of *1*, 60860S. SPIE, 2006.

[231] Zonare Medical Systems. z.one ultrasound system (3.0): advanced hardware operator manual. 2007.

[232] W. J. Graham. Analysis and synthesis of axial field patterns of focused apertures. *IEEE Transactions on Antennas and Propagation*, AP-31(4):665–668, 1983.

[233] T. D. Mast. Fresnel approximations for acoustic fields of rectangularly symmetric sources. *The Journal of the Acoustical Society of America*, 121(6):3311–3322, 2007.

[234] J. W. Sherman. Properties of focused apertures in the fresnel region. *IEEE Transactions on Antennas and Propagation*, AP-10:399–408, 1962.

[235] P. F. V. James and G. S. Agarwal. The generalized fresnel transform and its application to optics. *Optics Communications*, 126(4):207–212, 1996.

[236] F. A. Jenet and T. A. Prince. Detection of variable frequency signals using a fast chirp transform. *Phys Rev D*, 62(12):122001–122011, 2000.

[237] K. D. Mielenz. Computation of fresnel integrals. ii. *Journal of Research of the National Institute of Standards and Technology*, 105(4):589–590, 2000.

[238] V. A. del Grosso and C. W. Mader. Speed of sound in pure water. *The Journal of the Acoustical Society of America*, 52(5b):1442–1446, 1972.

[239] J. Kirkhorn. Introduction to IQ-demodulation of RF data. Technical report, Department of Physiology and Biomedical Engineering (IFBT), Norwegian University of Science and Technology (NTNU), 1999.

[240] X. Yang and C. C. Church. A model for the dynamics of gas bubbles in soft tissue. *The Journal of the Acoustical Society of America*, 118(6):3595–3606, 2005.

[241] National Physical Laboratory. *Kaye & Laby Tables of Physical and Chemical Constants*. National Physical Laboratory, 1995.

[242] K. Hynynen. The threshold for thermally significant cavitation in dog's thigh muscle in vivo. *Ultrasound in Medicine & Biology*, 17(2):157–169, 1991.

[243] T. K. Stanton. Sound scattering by cylinders of finite length. I. Fluid cylinders. *The Journal of the Acoustical Society of America*, 83(1):55–63, 1988.

[244] P. Howland, D. Maksimiuk, and G. Reitsma. FM radio based bistatic radar. *IEE Proceedings Radar, Sonar and Navigation*, 152(3):107–115, 2005.

[245] . Body temperature. *American Encyclopedia*, Academic American Encyclopedia:B 357, 1994.

[246] L. Chen, G. R. ter Haar, D. Robertson, J. P. M. Bensted, and C. R. Hill. Histological study of normal and tumor-bearing liver treated with focused ultrasound. *Ultrasound in Medicine & Biology*, 25(5):847–856, 1999.

[247] C. Simon, P. van Baren, and E. S. Ebbini. Two-dimensional temperature estimation using diagnostic ultrasound. *IEEE Transactions on Ultrasonics, Ferroelectrics, and Frequency Control*, 45(4):1088–1099, 1998.

[248] D. Napolitano, C.-C. Chou, G. McLaughlin, T.-L. Ji, L. Mo, D. DeBusschere,

and R. Steins. Sound speed correction in ultrasound imaging. *Ultrasonics*, 44:e43–e46, 2006.

[249] J. Sunamoto and T. Hamada. Solvochromism and thermochromism of cobalt (ii) complexes solubilized in reversed micelles. *Bull Chem Soc Jap*, 51(11):3130–3135, 1978.

[250] H. N. McMurray and B. P. Wilson. Mechanistic and spatial study of ultrasonically induced luminol chemiluminescence. *J Phys Chem A*, 103:3955–3962, 1999.

[251] Y. Iida, K. Yasui, T. Tuziuti, and M. Sivakumar. Sonochemistry and its dosimetry. *Microchemical Journal*, 80:159164, 2005.

[252] C. Lafon, V. Zderic, M. L. Noble, J. C. Yuen, P. J. Kaczkowski, O. A. Sapozhnikov, F. Chavrier, L. A. Crum, and S. Vaezy. Gel phantom for use in high-intensity focused ultrasound dosimetry. *Ultrasound in Medicine & Biology*, 31(10):1383–1389, 2005.

[253] A. Mills. Oxygen indicators and intelligent inks for packaging food. *Chem Soc Rev*, 34:1003–1011, 2005.

[254] P. L. Carson, X. Li, J. Pallister, A. Moskalik, J. M. Rubin, and J. B. Fowlkes. Approximate quantification of detected fractional blood volume and perfusion from 3-d color flow and Doppler power signal imaging. In *Ultrasonics Symposium, IEEE*. 1993.

[255] J. M. Rubin, R. S. Adler, J. B. Fowlkes, and R. S. Spratt. Fractional moving blood volume estimation with power Doppler ultrasound, 1999.

[256] N. Hockham, M. Arora, and C. C. Coussios. A real-time controller for sustaining thermally relevant cavitation during HIFU exposure. In *International Symposium on Therapeutic Ultrasound, Aix-en-Provence, France*. 2009.

[257] S. D. Sokka, T. P. Gauthier, and K. Hynynen. Theoretical and experimental validation of a dual-frequency excitation method for spatial control of cavitation. *Physics in Medicine and Biology*, 50:2167–2179, 2005.

[258] L. Mo, D. DeBusschere, G. McLaughlin, D. Napolitano, W. Bai, K. Fowkes, A. Irish, X. Wang, J. B. Fowlkes, and P. L. Carson. Compact ultrasound scanner with simultaneous parallel channel data acquisition capabilities. In *IEEE Ultrasonics Symposium*, 1342–1345. 2008.

[259] P. N. Burns. Introduction to the physical principles of ultrasound imaging and doppler, 2005.

[260] P. N. T. Wells. Ultrasound imaging. *Physics in Medicine and Biology*, 51(13):R83, 2006.